2000

# Optomechatronics in retroreflective grating metrology for 3D surface measurement.

Xianzhu. Zhang
*University of Windsor*

## Recommended Citation

Zhang, Xianzhu., "Optomechatronics in retroreflective grating metrology for 3D surface measurement." (2000). *Electronic Theses and Dissertations.* Paper 2955.

## INFORMATION TO USERS

This manuscript has been reproduced from the microfilm master. UMI films the text directly from the original or copy submitted. Thus, some thesis and dissertation copies are in typewriter face, while others may be from any type of computer printer.

The quality of this reproduction is dependent upon the quality of the copy submitted. Broken or indistinct print, colored or poor quality illustrations and photographs, print bleedthrough, substandard margins, and improper alignment can adversely affect reproduction.

In the unlikely event that the author did not send UMI a complete manuscript and there are missing pages, these will be noted. Also, if unauthorized copyright material had to be removed, a note will indicate the deletion.

Oversize materials (e.g., maps, drawings, charts) are reproduced by sectioning the original, beginning at the upper left-hand corner and continuing from left to right in equal sections with small overlaps.

Photographs included in the original manuscript have been reproduced xerographically in this copy. Higher quality 6" x 9" black and white photographic prints are available for any photographs or illustrations appearing in this copy for an additional charge. Contact UMI directly to order.

Bell & Howell Information and Learning
300 North Zeeb Road, Ann Arbor, MI 48106-1346 USA
800-521-0600

UMI®

# Optomechatronics in Retroreflective Grating Metrology for 3D Surface Measurement

by

**Xianzhu Zhang**

**A Dissertation**
**Submitted to the College of Graduate Studies and Research**
**through the Department of Mechanical Engineering**
**in Partial Fulfilment of the Requirements for the Degree of**
**Doctor of Philosophy of Mechanical Engineering at the**
**University of Windsor**
**Windsor, Ontatio, Canada**

**2000**

0-612-52448-5

# Abstract

With an explosion of technology occurring, optomechatronics is proposed as a general engineering area for the coming century. Optomechatronics is the integration of optical, mechanical, electrical, and other traditional engineering disciplines with microelectronics in order to unify machine and information technology. An optomechatronic product is a machine with knowledge and intelligence, which can process information and take action in response to human needs, other machines and the environment. Future trends in optomechatronic products will see smaller, swifter, and smarter systems. Optomechatronics provides a vision for engineers to meet the challange of intellectural broadness in technology. Retroreflective grating metrology is viewed as an example to illustrate optomechatronics.

Retroreflective grating metrology is a new optical technique for measuring the derivative and contour of quasi flat and reflective surfaces. It is based on a retroreflective process in which the retroreflective screen is very efficient in returning light to the light source. Uniform gratings can be produced in the optical process by attachment, painting, projection, moiré methods, etc. The gratings are modulated in phase by the surface under test. A efficient and simple mathematical model can relate the phase information in the deformed gratings to the derivative of the surface at each point. A variety of DFT (Discrete Fourier Transform) and PST(Phase shifting Technology) algorithms can be used to extract the phase information in the deformed gratings. The contour of the surface is found by integration. Experiments show that the method can detect slope related defects smaller than 10 microns, very efficiently.

The retroreflective grating metrology has been used to measure the 3D surface waviness on calibrated artifacts. In order to eliminate the effect of the illumination angle, a nonlinear equation was developed explicitly to calculate the slope from the phase information. The optical configuration for projection gratings technique was used for the measurement. The three-step PST algorithm was applied to analyze the grating image. Three calibrated artifacts with different wave amplitude were tested. The experiments show that the retroreflective metrology can recover the contour and amplitude of the 3D surface waviness on the standard artifacts successfully.

Retroreflective grating metrology is one of the most precise among the existing optical methods. This represents a new optical technique for surface measurement, which is efficient, practical and cost-effective compared to other existing optical methods such as grids, Moiré fringes, optical triangulation, and so on. This technology can be developed for machine vision and industrial application in Nondestructive Testing and Evaluation (NDTE).

Dedicated to

my family

# Acknowledgements

I would like to express my sincere gratitude to Dr. Walter P.T. North for his guidance, patience and support throughout the duration of this study.

Many thanks are owed to my colleagues, faculty and staff members of the Department of Mechanical, Automotive & Materials Engineering at the University of Windsor whose encouragement and assistance I really appreciated during the course of my graduate studies.

# Table of Contents

## Part I Optomechatronics

## Part II Retroreflective Grating Metrology for 3D surface Measurement

# List of Figures

## Part I Optomechatronics

## Part II Retroreflective Grating Metrology for 3D surface Measurement

# List of Tables

# Nomenclature

| | |
|---|---|
| 3S | Smaller, Swifter, and Smarter |
| DFT | Discrete Fourier Transform |
| PST | Phase Shifting Technology |
| WT | Wavelets Transform |
| D SIGHT | A surface measurement system made by Diffracto Ltd. |
| NDTE | Nondestructive Testing and Evaluation |
| CMM | Coordinate Measurement Machine |
| $\delta$ | The shifting distance of grating |
| L | The distance between the specimen surface and retroreflective screen |
| $\beta$ | The incidence angle of light to the surface of the specimen |
| $\theta$ | The local slope of the surface of the specimen |
| x | The coordinate perpendicular to the grating |
| y | The coordinate parallel to the grating |
| i(x,y) | The intensity of the grating image captured by camera |
| a(x,y) | The unwanted error arising from the variation of the background intensity |
| b(x,y) | The unwanted error arising from the variation of the grating contrast |
| p | The pitch of the grating |

| | |
|---|---|
| $\Phi(x,y)$ | The phase of the deformed grating |
| $n$ | The ratio of distance L to pitch p |
| $c(x,y)$ | $(1/2)b(x,y)\exp[i\Phi(x,y)]$ |
| $f_0$ | $1/p$ |
| $f$ | The spatial frequency in the x-direction |
| $d(x,y)$ | The depth of each point on the surface of specimen |
| $\Delta x$ | The unit length in x direction |
| $\Delta y$ | The unit length in y direction |
| $\alpha$ | The known added phase difference |
| $i_1(x,y)$ | The intensity of the grating image with phase shift $\alpha=0$ |
| $i_2(x,y)$ | The intensity of the grating image with phase shift $\alpha=\pi/2$ |
| $i_3(x,y)$ | The intensity of the grating image with phase shift $\alpha=\pi$ |
| $i_4(x,y)$ | The intensity of the grating image with phase shift $\alpha=3\pi/2$ |
| $\psi$ | A small angle diverted by retroreflector |
| $Z$ | The depth of each point on the profile |
| $\lambda$ | The wavelength of waviness on the quantified artifacts |
| $\omega_0$ | The spatial frequency of waviness on quantified artifacts$(=2\pi/\lambda)$; |
| $C_0$, $C_1$, and $\gamma$ | The coefficients of the trigonometric sum of order one |
| $A_0$, $A_1$, and $B_1$ | The coefficients of the trigonometric sum of order one |
| $\sigma$ | The standard deviation |
| $A$ | The background grey level |
| $B$ | The grating grey level amplitude |

# Part I Optomechatronics

# Chapter 1

# Optomechatronics--An Overview to Modern Technology

## 1.1 Introduction

Engineering is one of the key crafts and professions that has for millennia been part of the driving intellectual energy of economic development and social change as far back as the earliest civilizations[1]. As the twenty-first century nears, Engineering's role is more important than ever. With humanity's growing numbers and demands placing ever increasing pressure on the resources of a shrinking world, creative and thoughtful use of engineering and technology will remain essential for solving the problems of energy, food, transportation, housing, health care, communication, manufacturing, education, and environmental protection and for fulfilling all the other requirements of modern life.

An explosion of technology is occurring. It is not an explosion that affects the outward look of the landscape, as occurred in the period from 1850 to 1950 with the emergence of factories, large bridges and dams, automobiles and airplanes, highway systems, electronic power systems, telephones, and televisions. Instead, it is a revolution in the way things are designed, made, and controlled--in what they are made of and how they work.

This technological revolution is more subtle than past ones but just as pervasive and important in its impact and on human life. Many of the technologies of today and tomorrow are internal rather than external in their function and impact; often they operate on a microscopic and molecular scale-- or even invisibly, in the electromagnetic spectrum.

To adapt to the changing context of engineering, future engineers will have greater intellectual breadth, better communication skills, a penchant to collaboration, and a habit of lifelong learning[2]. Among these characteristics, it is essential that the knowledge they obtain will be broad enough to be comfortable with systems-oriented work and be able to move with relative ease between different specialized areas of engineering research.

Given the rapidity of the technological change, some interdisciplinary and multidisciplinary engineering areas are formed by integrating traditional engineering disciplines with new techniques. In this work, optomechatronics is proposed as a general engineering area for engineers to meet the challenge of intellectual broadness in technology.

## 1.2 Optomechatronic philosophy

### 1.2.1 Introduction

*Information technology* is computer technology appropriate to the encoding, storage, communication, manipulation, and use of information in digital form. *Information engineering* is the synthesis of new and old information techniques, producing the least cost method of distribution of services, production of labor, ecological revitalization to our world and more. Examples include the digital library, electronic education, electronic commerce, computer-based patient records and computer-based collaborative engineering, to name a few.

Information engineering is the fastest growing sector of modern industry. *Microelectronics* has experienced an exponential growth in the last five decades and is heading from the Mega to the Giga and Tera age in terms of speed and pixel density as feature size decreases from 0.5 to 0.05 micron[3]. *Microelectronics and packaging technology* is a keystone in modern industry.

In the past, the integration of electronics with mechanical components has often been more by coincidence or desperation than by design. Microprocessor controllers have often been merely added on to existing electro-mechanical systems. If the best properties of mechanical, electro-mechanical and microelectronic components are considered at the concept stage, a fully integrated design is possible offering dramatic improvement in performance. This is *mechatronics*.

With the increasing application of *optoelectronics and laser technology* to a wide range of consumer products and capital plants, optical engineering may often also need to be considered from the onset of the design exercise. Optical and laser-based technology provides a means of sensing engineering parameters such as distance, velocity, and deformation and can be integrated into equipment and used as a valuable tool at the development stage.

There are other interdisciplines which study the fusion of traditional techniques with microelectronics such as thermoelectronics, piezoelectronics, aviotronics, and so on.

### 1.2.2 Definition

Optomechatronics is the integration of optical, mechanical, electrical and other traditional engineering areas with microelectronics and the combination of machine with information technology.

### 1.2.3 Knowledge structure

The knowledge structure of optomechatronics is shown in Figure 1.1.

### 1.2.4 Characteristics

#### 1.2.4.1 Interfusion

The interfusion of the traditional engineering areas with microelectronics forms the interdisciplines such as mechatronics, optoelectronics, thermoelectronics etc. The purposes of these interdisciplines are to study the sensors which transfer non-electronic signals to an electronic signal and the devices that can be controlled by electronic signals to generate non-electronic variables. The digital computer is the bridge between microelectronics and information technology. Computers and computer networks provide the information infrastructure which can be universally accessible, day and night, at home and at school and at work.

#### 1.2.4.2 Interdependence

The traditional technologies provide important infrastructure for the microelectronics industry and physical support for electronic products, while microelectronics and information technologies are essential for innovation of conventional machines.

Information technology can provide important software tools (CAD/CAM/CAE) to design parts and systems for microelectronic and traditional engineering areas. Although mechanical and optical engineering incorporates microelectronics earlier in the design cycle and is the essential part of optomechatronics, other fusions are also in progress including thermoelectronics, piezoelectronics, acoustoelectronics, etc. The optomechatronic philosophy is unitiation of all the engineering areas.

### 1.2.5 Conclusion

The insular attitude to electronic, optical, and mechanical engineering is initiated at an early stage in the engineer's career by the need to select a single discipline degree course and is perpetuated by the departmental structure of most industrial companies. Optomechatronic philosophy not only offers a remedy to this problem but will also reshape the education and research in engineering in general. *Optomechatronics, energy electronics and new materials and properties* provide the full option in the technology aspect of product design to achieve optimal products. This integration may sound like a Utopian ideal, but if achieved it can have many benefits both to the final product and the efficiency of the company.

## 1.3 Optomechatronic product

### 1.3.1 Introduction

Currently, people in the engineering society are easily confused by all kinds of new concepts such as intelligent machines, smart products, mechatronic products, MEMS (microelectro-mechanical systems), MCMs(multi-chip modules), human-machine systems, and KBS(knowledge-based systems), etc. We prefer the term optomechatronic product to all the names although they are proper on the specific perspectives. A microprocessor is the centerpiece of an optomechatronic product. Computers and robots are the masterpiece of optomechatronic products. A robot is a computer with arms and/or legs. Almost all the modern instruments and equipment are specialized computers.

### 1.3.2 Definition

An optomechatronic product is a machine with knowledge and intelligence, which can process information and take action in response to human needs, other machines and the environment.

### 1.3.3 Generic model

The generic model of optomehatronic products is shown in Figure 1.2.

### 1.3.4 Properties

#### 1.3.4.1 Openness

An optomechatronic product is an open system which is able to interact with human beings, other machines and the environment through corresponding channels. Each channel can be one-way or two-way. Channels are also used to connect cells inside the optomechatronic product.

#### 1.3.4.2 Hierarchy

There are three levels in the hierarchy of an optomechatronic product: physical, logical, and operational. Non-electronic signals can be converted to electronic signals, electronic signals can control physical variables, analog electronic signals can be transferred to digital data, raw digital data can be formatted into multimedia like text, graphical, audio, video, etc.

#### 1.3.4.3 Recursion

There may be one or many optomechatronic products inside an optomechatronic product. One product can be a subsystem of another one.

### 1.3.5 Conclusion

An optomechatronic product incorporates a machine with information into a system. This will allow new sophisticated equipment to be developed.

## 1.4 Future Trends

### 1.4.1 Introduction

The explosion of technology is occurring and new techniques and concepts are appearing very fast. People feel uncertain about technology in the future. We envision three fundamental trends in optomechatronics and the optomechatronic product.

### 1.4.2 Trends

#### 1.4.2.1 Smaller

We are familiar with microengineering, microtechnology, microsoftware, microelectronics, micromechanical, micromechatronics, microoptics, microfluid, etc. and microsystem, micromachine, MEMS (microelectro-mechanical system), and so on. Advances in information devices are made possible by decreasing the bit cell size with a sufficient signal to noise ratio. To accomplish this, it is very important to increase the preciseness in machining, positioning and motion control of recording media and transducers. At the same time, it is also necessary to reduce mechanical disturbances such as vibration, friction, wear and temperature increases. The scientific and engineering techniques used to achieve this goal are *micromechanics, microtribology, and micromechatronics.*

The length scale involved in these devices is shifting from micro/sub-micrometer to nano/sub-nanometer. Micromachine technology, which first originated from LSI manufacturing technology, is now contributing to the innovation of key components used in information equipment. Miniaturization, micro/nano-technology and preciseness are key concepts in the advancement of *information equipment*.

For *precision equipment* such as machine tools, LSI manufacturing equipment, and various types of measuring instruments and so on, it is essential to increase the resolution of physical signals with a wide dynamic range. The science and engineering used for this purpose will be also termed micromechatronics. This includes micromechanisms, mechanics, tribology, machining, measurement and control. In addition, various kinds of scanning microscopes that reveal the nanometer surface structures have recently been developed, and the precision equipment used in this area is now undergoing rapid innovation.

### 1.4.2.2 Swifter

Conventional computers follow a serial model called the *Von Neumann machine*, in which one processor performs one instruction at a time. Although processing speed is being improved rapidly with the advance of VLSI technology, they have not provided enough computational power to satisfy the demand for solving the complex problems in machine vision, motion planning, virtual reality, communication, and so on.

*Parallel processing* is another way to improve computer performance. The parallel computer is the type of high performance computer that harnesses many processors together to solve a problem. A variety of parallel architectures and algorithms have been investigated. Physically, parallel can be implemented in a chip(circuit), package or at the machine level.

The information highway is emerging as the axis of inter-machine communications. Current PCs will become a network of PCs in the future. The highway is a webwork of powerful (high-capacity) computer-communications networks capable of handling everything from video to voice , text to computer data and graphics interchangeably, interactively and at a lightening speed[4].

One of the final goals of optomechatronics is to build an agency which can interact with the real world(human beings, other machines, and the environment) in real time. The response time should be limited only by physical properties of the machine. .

### 1.4.2.3 Smarter

*AI(artificial intelligence)* is an experimental science whose goal is to understand the nature of intelligent thought and action. This goal is shared with a number of established subjects such as philosophy, psychology, and neuroscience. The essential difference is that AI scientists are committed to computational modeling as a methodology for explicating the interpretative processes which underlie intelligent behavior, that relate sensing of the environment to action in it. Early workers in the field saw the digital computer as the best device available to support the many cycles of hypothesizing, modeling, simulating, and testing involved in research into these interpretative processes, and set about the task of developing a programming technology that would enable the use of digital computers as an experimental tool. A considerable amount of time and energy over the last 35 years or so has been given over to the design and development of new programming languages, tools and techniques. While the symbolic programming approach has dominated, other approaches such as non-symbolic neural nets or genetic algorithms have also featured strongly, reflecting the fact that computing is merely a means to an end, an experimental tool, albeit a vital one.

The popular view of intelligence is that it is associated with high level problem solving, i.e. people who can play chess, solve mathematical problems, make complex financial decisions and so on.

The term *Knowledge-Based System(KBS)* involves the integration of AI know-how methods and techniques with methods and techniques from other disciplines such as

Computer Science and Engineering to construct systems that replicate expert level decision making or human problem solving to make it generally available to technical and professional staff in organizations[5]. AI/KBS is migrating into industry and commerce in a wide variety.

### 1.4.3 Conclusion

Optomechatronic products will become smaller and faster, and intelligence and human capabilities will be incorporated into these machines. Will AI created on the materials overgrow human intelligence? The answer is no. AI, like expert systems and neural networks, do not replace human thought anymore than the motor car replaces human feet. No matter how it will be improved, a modern machine essentially has no difference with the earliest man-made artifact. It is a human-made tool but a complicated one.

## 1.5 Conclusion

Under the theory that all things are one, optomechatronics is presented as a united area of engineering forged from different disciplines, traditional and new, science and technology.

Technology has changed human society from the pre-industrial age, through industrial and information ages, to the post-information age. This century will go down in history as the century of technology. In these almost one hundred years we developed the ability to move people and things between any two points on the globe in hours and to keep those points in instantaneous communication. We sow, reap, cook, communicate, manufacture, travel, clothe, entertain, educate, research, manage, cure, and kill by highly technological means.

Engineering will be challenged as never before to shape the nature and quality of life in the twenty-first century. Future engineers will have the optomechatronic vision in technology and must be able to work together efficiently in teams to identify and solve complex problems in industry, academe, government, and society.

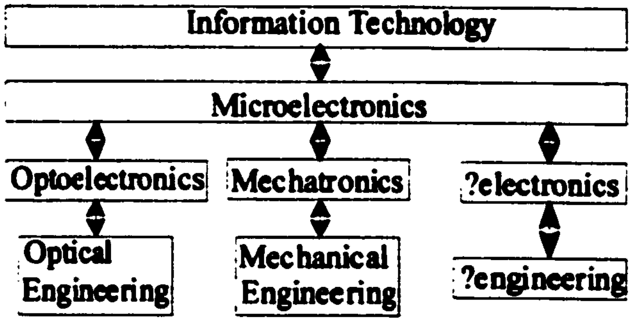

Figure 1.1 The knowledge structure of optomechatronics

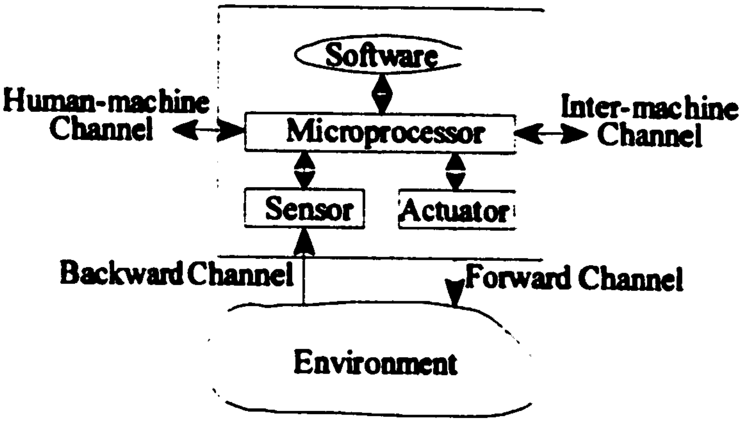

Figure 1.2 The generic model of optomehatronic products

# PART II Retroreflective Metrology for 3D Surface Measurement

# Chapter 1

# General Introduction

## 1.1 "Fit" and "finish" control in the auto industry

Quality control (QC) is very important in the automobile industry. A massive effort is made to improve what is called "fit" and "finish" of the auto sheet metal as this aspect of the product is what all customers can see and appreciate in their purchase.

"Fit" is the measure of "gap" and "flushness" where two sheet metal panels meet, for example the door and car body. The gap must not close such that the two panels interfere nor must it be so large that it looks like sloppy dimensional control of the processes. Where a gap of 5mm was acceptable 10 years ago, better production and assembly control permits this to be reduced to the sub millimeter range and the appearance factor to be much more pleasing. For the manufacturers, this in turn can result in a larger market share. One has only to look at the fit of the Yugo and the Russian Lada. These cars are inexpensive and reliable however it turns customer off when you can look through the gap into the car interior without opening the door! In these cars not nearly enough attention was paid to tolerance or assembly control, because these are very expensive to implement but have little to do with reliability of the product. On the other hand, General Motor had enormous difficulty with the plastic doors and fenders on the Saturn vehicle, while the gap dimension was reduced, the coefficient of expansion of plastics is 10 times that of steel resulting in a relatively large variation in gap dimension, depending on the assembly and/or ambient temperature.

Many automobiles manufactured now implement optical fit measurement in-line and/or after final assembly of the body-in-white(before painting). In this case as many as 100 optical fit measurements are taken during and after body assembly to insure that the process is under control and to monitor the trends such that corrective action can take place upstream in the manufacturing process.

"Finish" on the other hand, is the measure of the surface of the body-in-white panels as the panels are removed from the stamping dies, after they have been handled and stacked/stored/shipped and following assembly of the complete body-in-white vehicle. All stamping, mechanical handling, or assembly damage must be detected and eliminated before painting as painting makes errors much more noticeable. A customer can demand to have a car fixed and repainted for this flaw. As painting reveals these flaws, it is the most notorious of all reasons for customer perceived poor quality of a new vehicle.

A piece of dirt which falls into a die can cause an indent in the hood produced by the die/press operation. Further it can produce the same error in the next few thousand panels, if not corrected. A customer will not put up with this error staring him in the face each day that the car is driven. A die which has become dull modifies the surface with minor but noticeable creases. Furthermore, the hoods are stored/stacked/shipped to the assembly plant resulting in many more opportunities to accumulate handling damage. The assembly process itself results in further opportunities to introduce new errors in the panels. As a result, every auto assembly plant inspects and corrects such handling damage before painting.

Most of these inspections are primitive, manual and subjective.

Take for one example, the so called green room approach where the hood removed from a press is laid out on a bench in an inspection room with a hi-lighting fluid added to make the surface specular. A large number of fluorescent light tubes are located at various locations, green in color as the human eye is most sensitive to green. An inspector then walks around the panel imaging the linear fluorescent tubes through the panel surface. An indent will distort the linear nature of this image and a subjective grading system for quantity and the magnitude of such errors is employed for quality control.

Alternately, in final assembly, operators can be trained to "feel" very small errors with their fingers. Others use a process called "stoning" where a flat sharpening stone is rubbed on a suspected surface. This contacts and reveals an outdent or a zone of indent which is then marked for repair before the painting process.

Others use massive illumination on a hi-lighted surface for multiple inspectors to visually find and mark errors for repair as the body-in-white moves on the assembly line.

A large number of manufacturers use Dsight® on the hi-lighted surface using both visual and/or a CCD camera to identify and qualify the error. The CCD/computer system has the advantage that an area can be identified and examined for the extent and severity of

®: registered trademark

grey level variations to document and judge the error in a consistent and less subjective manner.

In the past ten years Dsight® has been widely used world wide in the auto industry, to quantify the production of sheet metal panels, to monitor the automobile body-in-white assembly before painting, as small indents can become quite noticeable after painting. Dsight® is still subjective as it does not yield contour, rather it responds to local slope variations which must be calibrated by quality control personal who determine the level and extent of a Dsight® evaluated error, which must be repaired.

Glossy black painted surfaces reveal errors to the naked eye much more readily than glossy white painted surfaces. Dsight®, when used with colored painted surfaces, is independent of the color, in which case a color CCD camera is not necessary.

Every effort is made in manufacturing to reduce or eliminate the production of these errors as the repair cost is significant and the bumping and grinding repair of the surface removes some of the zinc rust protection which can compromise the finished painted product.

## 1.2 Research objectives

The objective of this research is to use the Dsight® technology to find slope related errors on specular surfaces and then use gratings in the optical path to extract the phase shift in the distorted grating which in turn yields local slope and ultimately the contour of the surface itself.

Several optical methods to introduce the gratings will be proposed and as well as an evaluation of the typical accuracy, precision, sensitivity and range of the measurements. The goal of this research is to determine of a panel using as much of the Dsight® hardware as possible.

By this procedure, Dsight® can become much more valuable as it will yield more information in the quality control of such manufactured surfaces.

This research will mainly focus on the following areas:

(1) to investigate different optical configurations;

(2) to use both DFT and PST methods to extract phase information in the distorted grating;

(3) to use the quantified artifacts to verify the retroreflective grating metrology.

# Chapter 2

# An Introduction to Retroreflective Grating Generation and Analysis

## 2.1 Retroreflective optics in Dsight®

Dsight® is a recent invention([41]~[44]) which is particularly useful for inspection of specular surfaces to determine if there are local errors as a result of the forming processes. The major advantage is that it employs a low power white light source which can illuminate a large area since the light comes from a radiator of small dimension. Dsight® is also insensitive to the mechanical translation, rotation or vibration of the retroreflector. The light illuminating the surface reflects from the surface to a large area retroreflector. The retroreflector returns the light back to the light source using a second pass over the same surface. In this arrangement the light source and the imaging camera can be conveniently located at the same location. For a surface with no errors, the grey level image will be uniform while one with local errors such as dents, the image has large variations in grey level. These grey levels identify both the location and relative severity of the errors making the system quite useful for this type of inspection.

However, Dsight® in its simplest format, does not yield contour information. The grey levels observed are somehow related the variation of the local slope, giving a subjective representation of the surface which is used to teach good from weak to poor and unacceptable.

In this research, Dsight® was used to detect the location and relative severity of a localized surface error. From industrial applications, Dsight® is known to be very sensitive in detecting even sub micron surface deviations, and as such, forms the basis for the resolution limit of a localized flaw in this research. That is to say, that Dsight® must be able to detect the localized flaw before this fringe based metrology can be used to produce its contour.

While Dsight® responds to local slope variations, it does not responds to general curvature by itself. As it turns out, this is a significant advantage of Dsight®, as inspection for dents on an auto fender panel does not require that the fender panel be precisely registered in the field of view.

Dsight® is an optical process that converts local surface curvature changes into greyscale changes. This enhanced surface inspection technique is used for evaluationg surface distortions, depressions or other slope related protrusions. This process has excellent micron sensitivity and a large dynamic range.

Figure 2.1 shows the basic elements required for the Dsight® process: A camera unit consisting of a CCD camera and a point light source, the surface being inspected and a retroreflective screen(retroreflector). The light from a point light source spreads and strikes the surface where it is reflected onto the retroreflective screen. The retroreflector(such as 3M Scotchlite) is made up of very small(25~75μm diameter), high refractive index glass beads with a silvered reflective coating on the back, bonded to a flexible sheet. This screen returns the light to the surface where it is reflected back to the light source in a very precise path. If any irregularities exist in the surface, the uniform light field upon striking the surface of the specimen will become distorted, and the light field will now have varying grey levels striking the retroreflective screen. If the screen were a perfect retroreflector, each ray of light would follow the exact same path along the optical axis back to the light source. Furthermore, upon being reflected back from the specimen surface, all the distortions occurring to the light field from the first reflection will simply be reversed, i.e., a uniform light field will return to the source. However, the retroreflective screen is not perfect (the light is slightly scattered) and returns a cone of light to the light source via surface. The ray in the diverging cone of light will not trace its incident path back to the light source. When this different path is followed, then the rays in the diverging cone of light will not reflect from the specimen at the exact same point they did the first pass, thus not reversing the distortions in the light field which occurred in the first reflection. Since the rays in this diverging cone do not return precisely to the light source, they may be detected by a camera, or human eyes. Provided that the camera is very close to the optical axis of the incident light source, the intensity variation of the light seen by the camera is therefore a map of the local surface curvature variations on the surface being inspected. Industrially this local surface curvature map is referred to as a Dsight® image and can be used to indicate surface quality or can even be used to infer subsurface conditions[42], which manifest themselves in surface slope variations.

Figures 2.2 and 2.3 show typical automobile sheet metal for an acceptable vehicle with the Dsight® variations showing small slope related errors. These errors are not sufficient to become visible to the customer. The variations can however identify, when a problem in the stamping operation is beginning such that changes can be made to correct this before it becomes a major problem. Furthermore, this signal must be qualitatively assessed for severity as this image does not yield the contour.

## 2.2 Fringe-based optical metrology

Fringe-based optical metrology generally comprises two major processes, i.e., (a) fringe generation by using optical systems and (b) fringe analysis based on signal processing. A variety of fringe analysis methods have been applied to the fringes generated by interferometers, reflective gratings, projection grids, Moiré methods, etc([20]~[40]). The key to the success of modern fringe-based metrology is good interaction and match between the fringe generation and fringe analysis. A good fringe design is essential for realization of the interaction and match, as shown in Figure 2.4.

Those and other optical methods are extensively employed to inspect and/or quantify surfaces for contour profile, roughness, local displacements, cracks and other flaws in general. Each of the methods have their advantages and disadvantages or application for a specific class of measurement.

In this research the problem is the inspection of quasi flat specular surfaces typical of painted automobile sheet metal panels, the dies used to form these sheet metal panels, plastic parts or body-in-white panels which have been highlighted with a liquid surface to make them specular, and so on.

This fringe based metrology proposed here, along with Dsight, can however contour the curvature of the fender panel as well as the localized surface errors.

Having identified the surface error using Dsight, a linear grating is placed on the retroreflector such that this surface error would modulate the grating.

In the beginning of this research using D SIGHT®, we placed a coarse linear grating of constant pitch on the retroreflector itself to capture the image of the grating through the surface of sample. Local errors in the slope cause the grating to be distorted and shifted in response to the dimensional change in the profile.

These distortions then carry the information of the profile dimension. This profile dimension can be extracted by measurements taken directly from the image of the distorted grating or by further processing the grating information in order to extract more resolution for the dimensional measurements.

## 2.3 Retroreflective grating generation and modelling

Retroreflector optics returns any light from a light source on a very precise optical path back to the light source. This precision in optical geometry permits us to know exactly where the light path was both leaving the light source as well as returning to the light source. This precision is crucial as it allows us to model the optical system much more accurately than when imaging light from a diffuse surface, which scatters light in all directions.

An example of an optical configuration for retroreflective grating metrology is shown schematically in Figure 2.5. Because the surface is specular, the optical axis was as close to perpendicular to the surface as was possible to minimize parallax distortion. Furthermore the panel and retroreflector are themselves parallel. All of figures to follow, show this optical axis at an arbitrary angle so as to better demonstrate the path of individual rays. In this simple case, the black straight linear grating is attached to the retroreflective screen and observed through the surface of the specimen. The grating is physically located to encompass the zone of the flaw to be measured. If the surface of the specimen is very flat and has no flaw, a uniform grating pattern is observed and, conversely, if the surface has some flaws, the pattern will be bent and shifted due to the variation of slope. The shifting distance $\delta$ can be calculated by

$$\delta=L[\tan(\beta+2\theta)-\tan(\beta)] \qquad (2.1)$$

where

$L$ is the distance between the specimen surface and retroreflective screen;

$\beta$ is the incidence angle of light to the surface of the specimen;

$\theta$ is the local slope of the surface of the specimen.

Because $\theta$ is relatively small and $\beta$ is close to zero, equation(2.1) can be simplified as

$$\delta=2L\theta \qquad (2.2)$$

Because the distance $L$ is constant, equation 2.2 indicates that there is a linear relationship between the shifting distance $\delta$ and the local slope $\theta$.

## 2.4 Schematic diagram for retroreflective grating metrology

The schematic diagram of retroreflective grating metrology is shown in Figure 2.6. A grating generator can produce a uniform grating by attachment, painting, projection, moiré methods, etc. The uniform grating is modulated in phase by the variation of local slope on the surface under test. The distorted grating is captured by an image grabber. The phase information in the distorted grating image is extracted by a phase demodulator implemented in software. The local slope on the surface under test is proportional to the phase in the distorted grating image and can be obtained from this phase. The contour of the surface is found by integrating the slope.

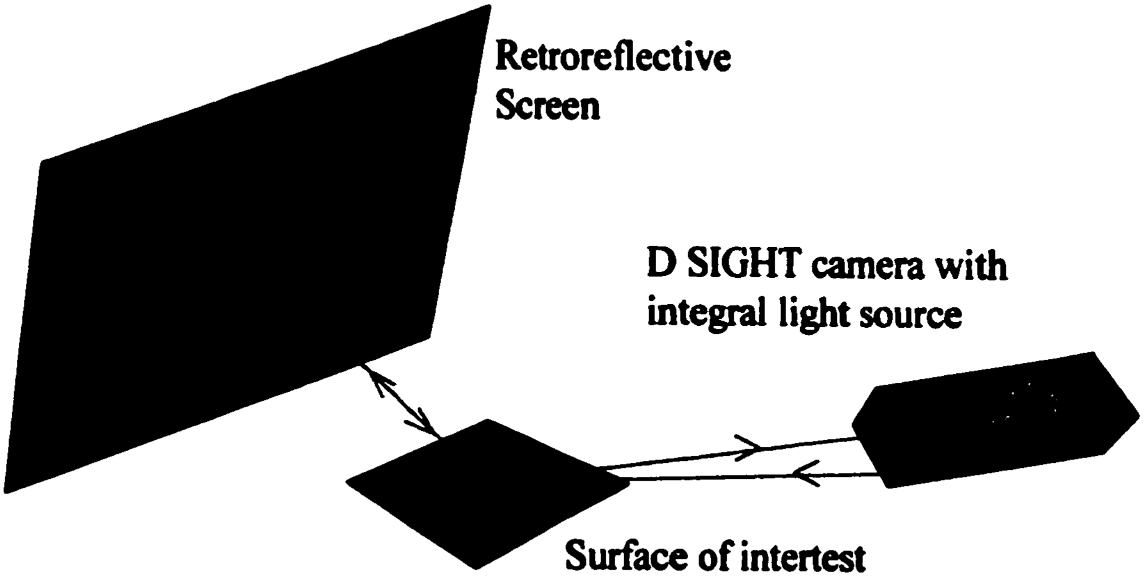

Figure 2.1 The basic D SIGHT® arrangement

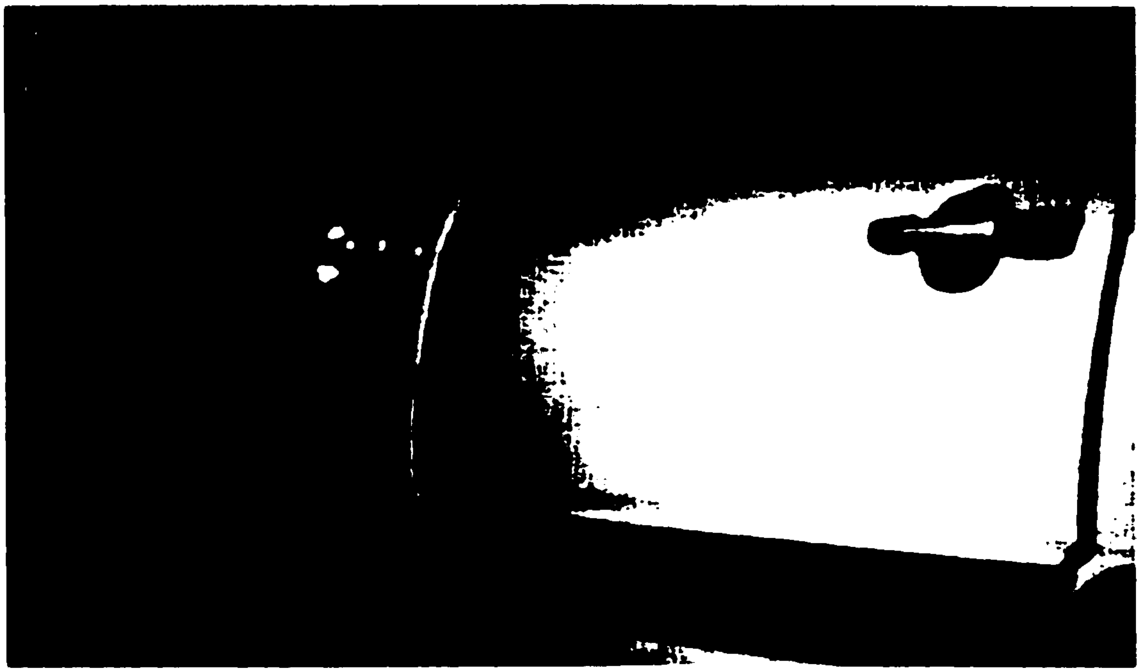

Figure 2.2a The image of a car door without Dsight®

Figure 2.2b The image of the same car door with Dsight®

Figure 2.3a The image of a car body without Dsight®

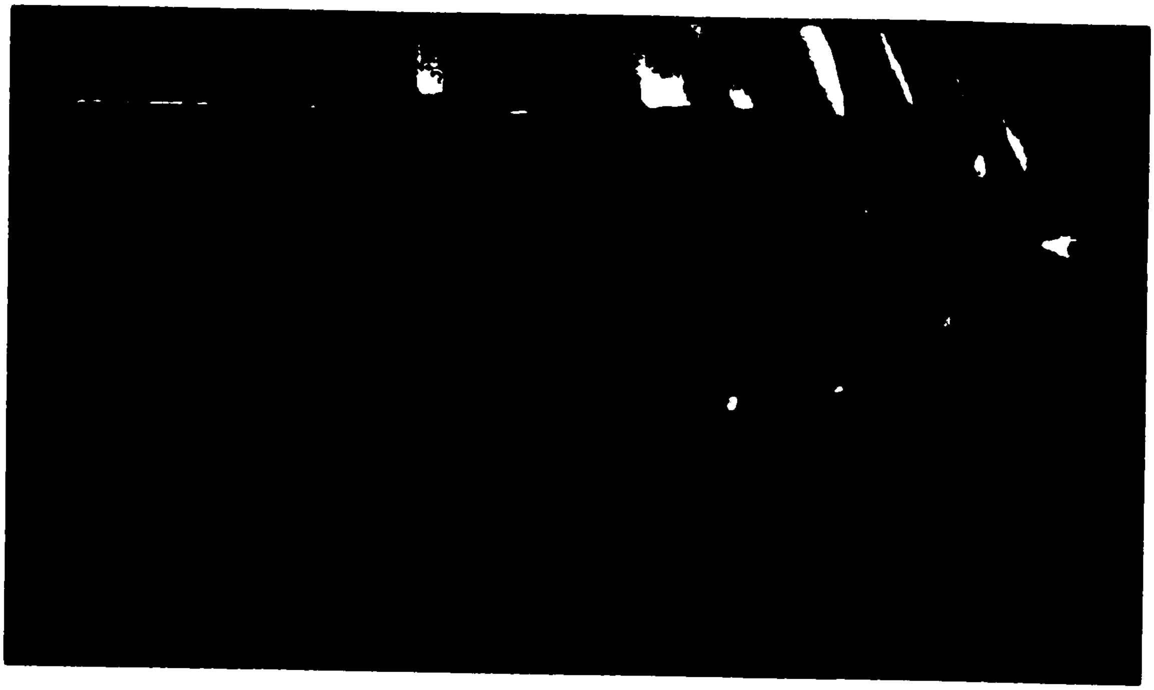

Figure 2.3b The image of the same car body with Dsight®

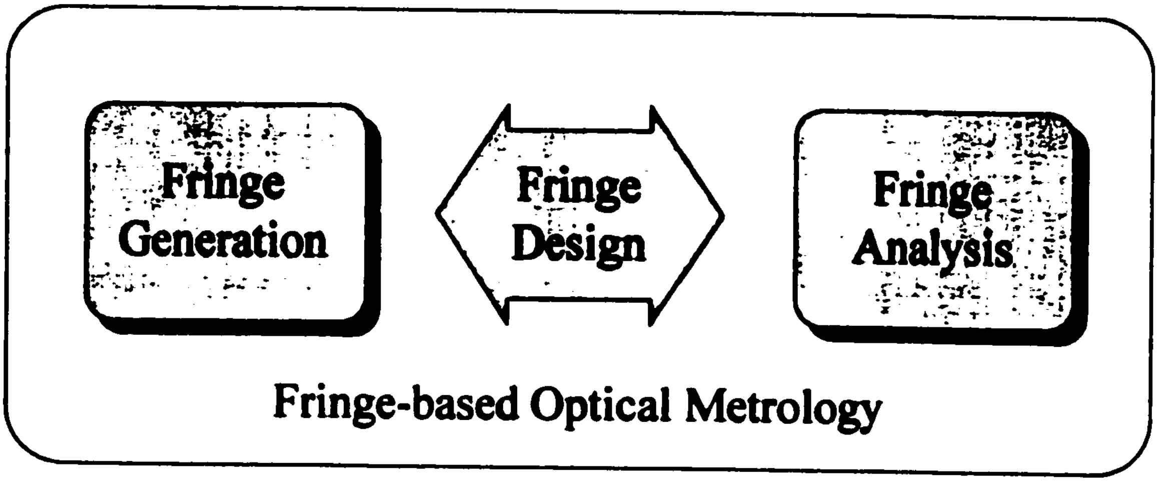

Figure 2.4 Fringe-based optical metrology comprised of

fringe generation and analysis

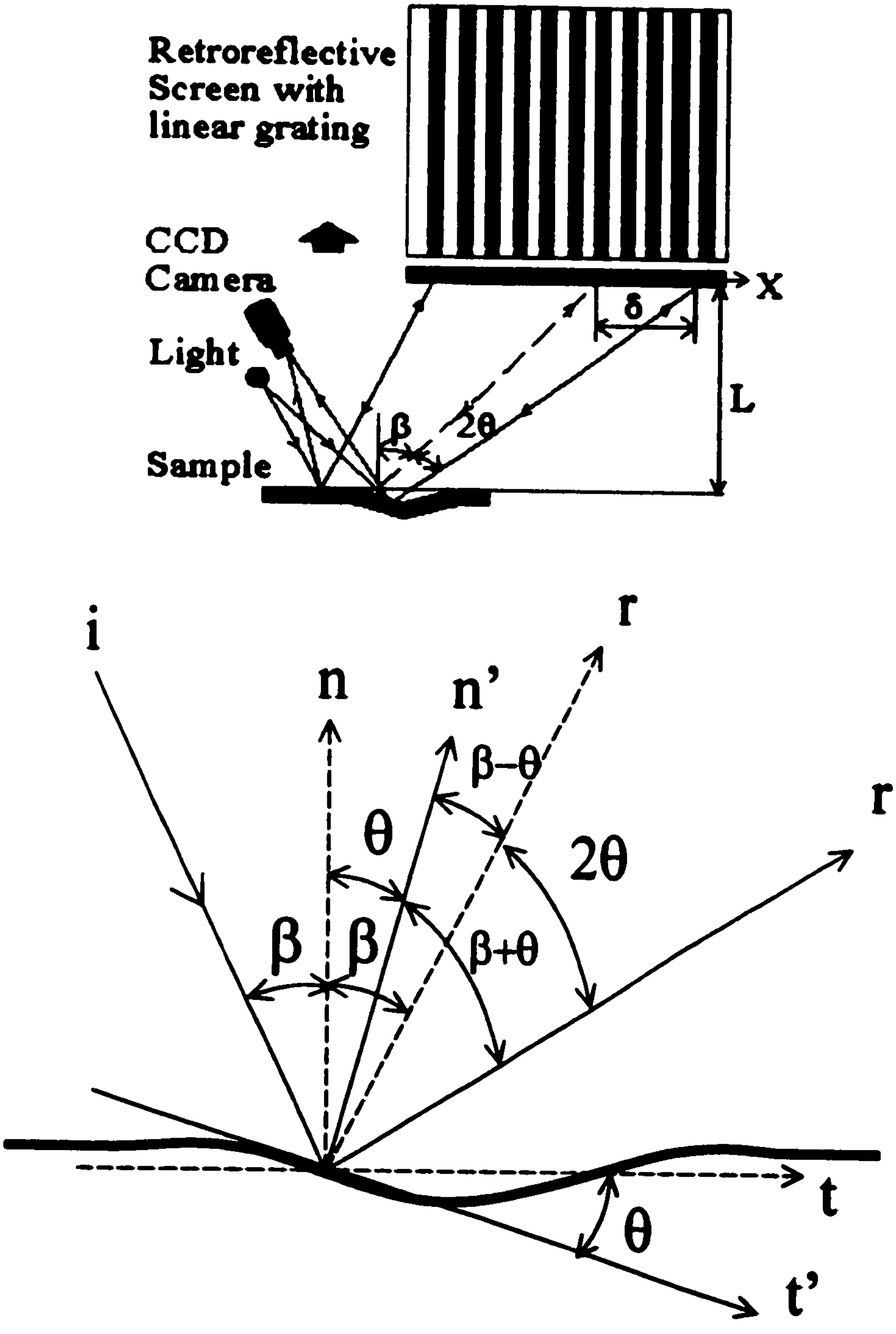

Figure 2.5 An example of optical configuration for

retroreflective grating metrology

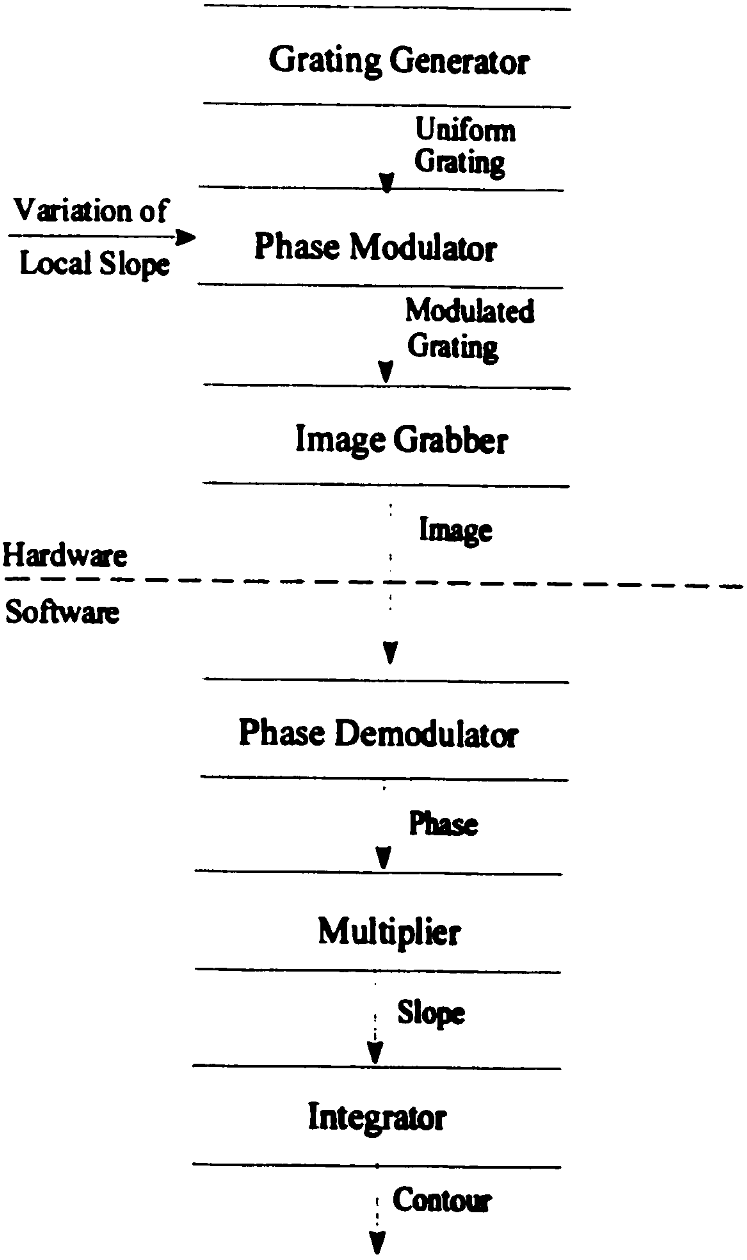

Figure 2.6 The schematic diagram of retroreflective grating metrology

# Chapter 3

# Retroreflective Grating Analysis by Discrete Fourier Transform(DFT)

## 3.1 Introduction

The grating analysis by Discrete Fourier Transform(DFT) is a technique that transfers the grating image from spatial domain to frequency domain and is then converted back to the spatial domain. By this procedure, it is easy to separate or extract the phase information from the unwanted noise arising from the variations of the background intensity and grating contrast. The Fourier method has the advantage of requiring only one frame of a grating image for the analysis. This makes it particularly attractive for dynamic applications or instances where vibrations make measurements difficult. A variety of DFT algorithms can be used to extract the phase information ([47]~[51]). However, difficulties with this method are inevitable near edges and at discontinuities.

The phase information obtained by the Fourier method is wrapped into the principal value ranging from $-\pi$ to $\pi$, which has to be unwrapped. The phase unwrapping may be hindered by the existence of singular points or defects in the phase information. The singular points can be generated by noise and/or under sampling, and may be unavoidable in the measurements from objects with rough surfaces and/or of discontinuous contour. Various noise-immune algorithms have been proposed to cope with the singular points ([52]~[58]).

## 3.2 Modeling the grating image

Figure 3.1 shows an example of system arrangement for retroreflective grating analysis by the Fourier method. Dsight® is first used to identify and locate a surface error. An accurate grating can then be attached to the retroreflector so as to incorporate the zone of the error which is to be contoured. The figure shows the point light source very close to the CDD camera as the retroreflector is very efficient in returning the light to the light source. In this case the retroreflector is parallel to the surface under test and since the surface is quite smooth, the angle of illumination incidence is close to zero degrees. A frame grabber captures the image and the computer processes and displays the result.

If the surface of the specimen is perfect, the intensity of the image captured by the camera can be modeled as

$$i(x,y)=a(x,y)+b(x,y)\cos[(2\pi/p)x] \tag{3.1}$$

where a(x,y) and b(x,y) represent the unwanted noise arising from the variations of the background intensity and grating contrast. p is the pitch of the grating.

If there are some slope related defects on the surface of specimen, the deformed grating, due to the change of slope on the surface, can be modeled as

$$i(x,y)=a(x,y)+b(x,y)\cos[(2\pi/p)x+\Phi(x,y)] \quad (3.2)$$

where $\Phi(x,y)$ is the phase of the deformed grating, and

$$\Phi(x,y)=(2\pi/p)\delta=(2\pi/p)[2L\theta(x,y)]=4\pi(L/p)\theta(x,y)=4\pi n\theta(x,y) \quad (3.3)$$

and n is the ratio of distance L to pitch p.

## 3.3 Algorithm

A variety of DFT(Discrete Fourier Transform) algorithms can be used to extract the phase information from Eq.(3.2). Here, a simple columnwise DFT method is applied to the system. Eq.(3.2) can be rewritten in the following form for the convenience of explanation.

$$i(x,y)=a(x,y)+(1/2)b(x,y)\{\exp[i(2\pi f_0x+\Phi(x,y))] \\ +\exp[-i(2\pi f_0x+\Phi(x,y))]\}$$

$$i(x,y)=a(x,y)+c(x,y)\exp[(2\pi f_0x)i]+c^*(x,y)\exp[(-2\pi f_0x)i] \quad (3.4)$$

with

$$c(x,y)=(1/2)b(x,y)\exp[i\Phi(x,y)] \quad (3.5)$$

and $f_0=1/p$,and * denotes a complex conjugate.

Next, Eq.(3.4) is Fourier transformed with respect to x, and we have

$$I(f,y)=A(f,y)+C(f-f_0,y)+C^*(f+f_0,y) \quad (3.6)$$

where the capital letters denote the corresponding variables in the frequency domain and f is the spatial frequency in the x-direction. Since the spatial variations of a(x,y),b(x,y),and Φ(x,y) are slow compared with the spatial frequency $f_0$, the Fourier spectra in Eq.(3.6) are separated by carrier frequency $f_0$, as is shown in Figure 3.2. We make use of either of the two spectra on the carrier, say $C(f-f_0,y)$, and shift it by $f_0$ on the frequency axis toward the origin to obtain C(f,y). Note that the unwanted background variation a(x,y) has been filtered out in this stage. Again, we use the inverse Fourier transform of C(f,y) with respect to f and obtain c(x,y),defined in Eq.(3.5). Then we calculated a complex logarithm of Eq.(3.5)

$$\log[c(x,y)]=\log[(1/2)b(x,y)]+i\Phi(x,y) \qquad (3.7)$$

Now we have the phase Φ(x,y) in the imaginary part completely separated from the unwanted amplitude variation b(x,y) in the real part. The phase so obtained is indeterminate to a factor of 2π as is shown in Figure 3.3a. In most cases a computer-generated function subroutine gives a principal value ranging from -π to π. These discontinuities can be corrected by a phase unwrapping algorithm. The continuous profile of phase distribution is shown in Figure 3.3b.

If we rearrange the Eq.(3.3), we have the local slope of the sample surface

$$\theta(x,y)=\Phi(x,y)/(4\pi n) \qquad (3.8)$$

The depth of each point on the surface of specimen d(x,y) can be found by integrating slope in the x direction

$$d(x,y)=\int\theta(x,y)dx \qquad (3.9)$$

## 3.4 Experiment

In the following experiments, the parameters of the system configuration are set as follows.

L=270cm(the distance between the specimen surface and retroreflective screen),

p=1.00cm(the pitch of the grating),

n=270(the amplification of the optical configuration),

Δx=0.150mm(unit length in x direction), and

Δy=0.170mm(unit length in y direction).

Two groups of dents are tested. They were made on the surfaces of 10cm x 10cm metal sheet having 1.00mm thickness. The straight linear grating with rectangular profile and 1.00cm pitch is attached to the retroreflective screen.

Figure 3.4a shows the grating image with two indents(dent 1 and 2) on the same specimen surface. Figure 3.4b shows the slope of the surface calculated by the columnwise DFT along the x direction. There are discontinuities in the y direction through the centers of the dents, which arise from the large sampling distance dx. Figure 3.4c shows the contour of the surface with the dent 1 and 2 in the dimension of microns. Figure 3.4d shows the maximum depths of the dent 1 and 2.

Figure 3.5a shows the grating image with one indent(dent 3) and one outdent(dent 4) on the same surface. Figure 3.5b shows the slope of the surface with the dent 3 and 4. Figure 3.5c shows the contour of surface with the dent 3 and 4. Figure 3.5d shows the maximum depths of the dent 3 and 4.

In order to verify the accuracy of the columnwise DFT method, we measure the surface contour through the center of the dents by using the Rank Taylor Hobson machine, recognizing that it is difficult to ensure that the trace passes through the plane having the maximum excursion.

Table 3.1 lists the comparison of the maximum values calculated by the columnwise DFT method with the results from the Rank Taylor Hobson machine. The experiment indicates that the system can determine the amplitude of the defect and the polarity(indent/outdent). The discontinuities in the slope map of the dents presented in Figures 3.4b and 3.5b result from the physical characteristics of the dents. The slope of an indent(outdent) changes abruptly from a negative maximum value(a positive maximum value) to a positive maximum value(a negative maximum value) near the bottom of the dents in the x direction. This is verified by the physical measurements presented in Figures 3.7b and 3.8b of the next section.

The "noisy" contour as indicated in the figures 3.4c, 3.4d, 3.5c, and 3.5d arises from the large sampling length dx and the direction of integration. The slope changes more rapidly near the bottom of the defects on the surface. Because the surface is uniformly sampled, the area near the bottom is undersampled. The slope value has maximum uncertainty in the bottom. When we integrate from one side along x direction, the errors will spread to the other side of the surface.

The noise could be reduced by integrating in the positive x direction and then in the negative x direction if we could make sure that the two integrating start points are at the same depth.

## 3.5 Comparison of the DFT method with physical measurements

A small indent was made on a 10cm x 10cm metal sheet having 1.00mm thickness. The straight linear grating with rectangular profile is placed on the retroreflective screen. The columnwise DFT method is applied for grating analysis.

Figure 3.6a shows the grating image with the indent on the specimen surface. Figure 3.6b shows the slope of the surface calculated by the columnwise DFT along the x direction. Figure 3.6c shows the contour of the surface with the indent in the dimension of microns. Figure 3.6d shows the maximum depth of the indent.

In order to verify the accuracy of the technique, the profile was measured through the center of the same dent by using a Rank Taylor Hobson machine. The surface profile is shown in Figure 3.7a, and the maximum value identified in Figure 3.7b.

The Rank Taylor Hobson machine consists of a Form Talysurf Series Version 1.02, a 50mm Transverse Unit and an Inductive Gauge Unit with interchangeable styli. The resolution using 1mm range stylus arm is 32nm. The tip radius(the Standard Conical Diamond 112/2099) is 1.5-2.5μm. The stylus force over full range is 70-100mgf.

In a second procedure to confirm the measurement method, a 3D Coordinate

Measurement Machine(CMM) was used to measure the area with the indent in it. The surface contour is shown in Figure 3.8a and maximum depth in Figure 3.8b.

The machine model is DEA CMM Gauge 2000. Its measuring range is X-Axis 458mm, Y-Axis 510mm and Z-Axis 406mm. The linear displacement accuracy is X-Axis 5.0μm, Y-Axis 5.0μm and Z-Axis 5.0μm. The repeatability is 4.0μm. The Renishaw type probe has a small ball of 0.5mm diameter to contact the surface.

Table 3.2 compares the maximum excursions as obtained from retroreflective grating analysis with conventional physical contacting measurements.

In this case the physical contacting measurements were taken using a Rank Taylor Hobson profilometer which scans contour in a linear fashion over a prescribed distance. The probe is a sharp point drawn over the surface with small pressure so as not to scratch or deform the surface. Neither condition is perfectly satisfied as even the small pressure can distort a surface and the sharp point always leaves some type of scratch. This approach also has the disadvantage that the operator must decide the center of the indent which to scan.

A DEA CMM was also used to scan a surface area in a point by point procedure which is very time consuming. In this case, an area of 10 mm by 10 mm was scanned in more than 60 minutes. The Renishaw type probe with resolution 0.5 μm has a small ball of diameter 0.5 mm to contact the surface which applies a significant pressure making it impossible to repeat the surface profile unless the surface itself is massively rigid. The small pressure was also sufficient to mark the bright surface of the sample.

In both instruments, the measuring head has significant dimensions, and both instruments are very expensive. They represent the industrial standard.

## 3.6 The maximum range of measurement in the second derivative

Since DFT is based on filtering for selecting either of the two spectra on the carrier frequency $f_0$, the carrier frequency must separate them from the spectrum of the unwanted background variation. This condition limits the maximum range of measurement for the second derivative of a surface.

The image of the deformed grating due to the change of slope on the surface under test was modeled as Eq.(3.2), which is repeated here.

$$i(x,y)=a(x,y)+b(x,y)\cos[(2\pi/p)x+\Phi(x,y)] \tag{3.2}$$

Because the columnwise DFT method was used to analyze the image slice by slice in the x direction, the Eq.(3.2) is reduced to the next equation.

$$i(x) = a(x) + b(x)\cos[2\pi f_0 x + \Phi(x)] \tag{3.10}$$

Where $f_0=1/p$.

We define a local spatial frequency

$$\begin{gathered} f = \frac{1}{2\pi}\frac{d}{dx}[2\pi f_0 x + \Phi(x)] = f_0 + \frac{1}{2\pi}\frac{d\Phi(x)}{dx} = f_0 + \frac{1}{2\pi}\frac{d[4\pi n\theta(x)]}{dx} \\ f = f_0 + 2n\frac{d\theta(x)}{dx} \end{gathered} \tag{3.11}$$

Let $f_b$ be the maximum frequency of the background variation, and for the spectrum on the carrier frequency to be separated, it is necessary that

$$
\begin{aligned}
&f_b < (f)_{\min} \\
&f_b < f_0 - 2n\left|\frac{d\theta(x)}{dx}\right|_{\max} \\
&\left|\frac{d\theta(x)}{dx}\right|_{\max} < \frac{f_0 - f_b}{2n} < \frac{f_0}{2n} = \frac{1/p}{2(L/p)} = \frac{1}{2L}
\end{aligned}
\tag{3.12}
$$

where $\left|\frac{d\theta(x)}{dx}\right|_{\max}$ denotes the maximum absolute value which is the larger value of

$\left|\left[\frac{d\theta(x)}{dx}\right]_{\max}\right|$ and $\left|\left[\frac{d\theta(x)}{dx}\right]_{\min}\right|$.

The condition states in the DFT method, that there is a limitation for the maximum second derivative to be measured, which is related to the distance L between the surface under test and the retroreflector. It can be extended by decreasing L to prevent the phase from being overmodulated, but this responds to reducing the sensitivity of the measurement. But the retroreflective metrology retains a sensitivity sufficient for the most applications since it can detect a phase distribution much less than $2\pi$. This was demonstrated by the experiments.

In the measurement, since L is 2700mm then the maximum value of the second derivative allowed by the DFT method is

$$
\left|\frac{d\theta(x)}{dx}\right|_{\max} <= \frac{1}{2L} = \frac{1}{2 \times 2.70 \times 10^{3} mm} = 1.85 \times 10^{-4} rad/mm
\tag{3.13}
$$

The maximum slope change in adjacent pixels is

$$|\Delta\theta|_{\max} = \left|\frac{d\theta(x)}{dx}\right|_{\max} \times \Delta x = 1.85\times10^{-4}\,rad/mm \times 0.15mm = 2.78\times10^{-5}\,rad \tag{3.14}$$

The maximum depth change in adjacent pixels is

$$\Delta d = |\Delta\theta|_{\max} \times \Delta x = 2.78\times10^{-5}\,rad \times 0.15mm = 4.16\times10^{-6}\,mm = 4.16nm \tag{3.15}$$

## 3.7 Conclusion

Advantages:

1. Retroreflective grating analysis by DFT has been used to determine the contour of a sheet metal dent and confirmed by mechanical contacting measurement.
2. This procedure also determines polarity i.e. indent VS outdent.
3. It is capable of measuring small dents of the order of 10microns depth.
4. Because the method is optical, it is noncontacting.
5. The method generate 3D contour of a significant area rather than a point by point measurement(CMM) or a linear scan(Taylor Hobson Technology).
6. It yields results much faster than CMM or Taylor Hobson Technology.
7. It requires only one image frame of the surface which can have advantages if the surface is not stationary.
8. The DFT method eliminates noise due to background and grating contrast. It is more powerful than simply observing the distorted grating image and ordering the grating

image centers.

Disadvantages:

1. Each point in the surface contour is determined by light from many points on the surface.
2. Undersampling leads to cumulative error which is propagated to other areas.
3. Image fidelity is degraded by discontinuities and the presence of edges.
4. The surface under test must be quasi flat and specular.
5. Dsight® must be sensitive enough to identify and locate any error which is subsequently scanned.
6. The range of measurement has a limitation to the second derivative of the surface under test.

An error analysis of the DFT method is presented in Appendix C.

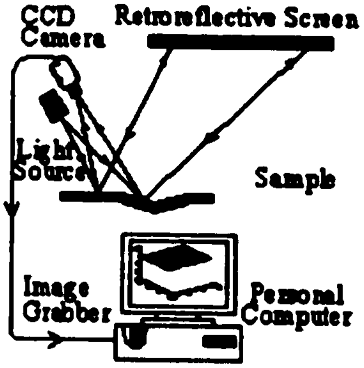

Figure 3.1 An example of system arrangement for retroreflective grating analysis by the Fourier method

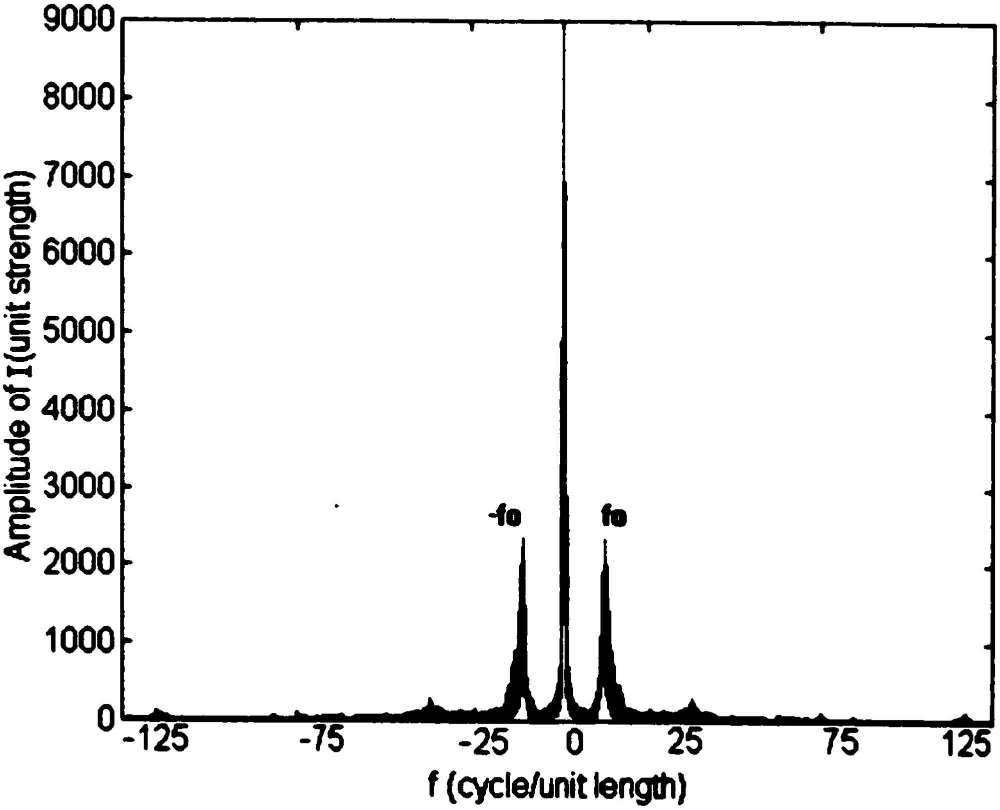

Figure 3.2 The Fourier spectra of deformed grating along x direction

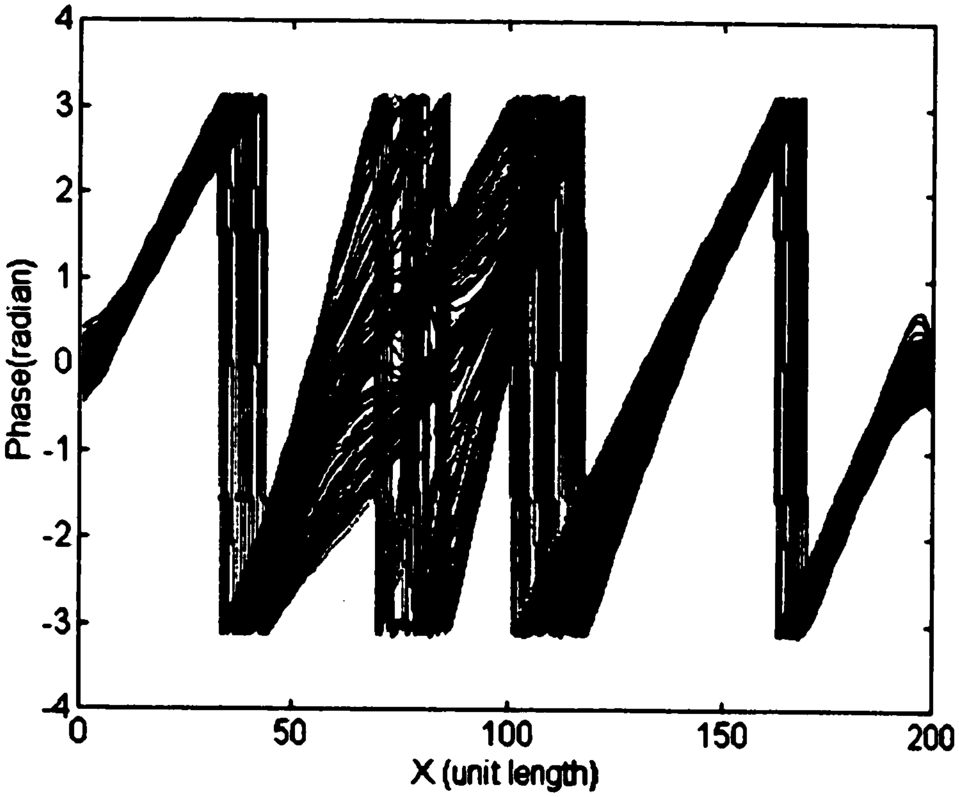

Figure 3.3a An example of a discontinuous phase distribution

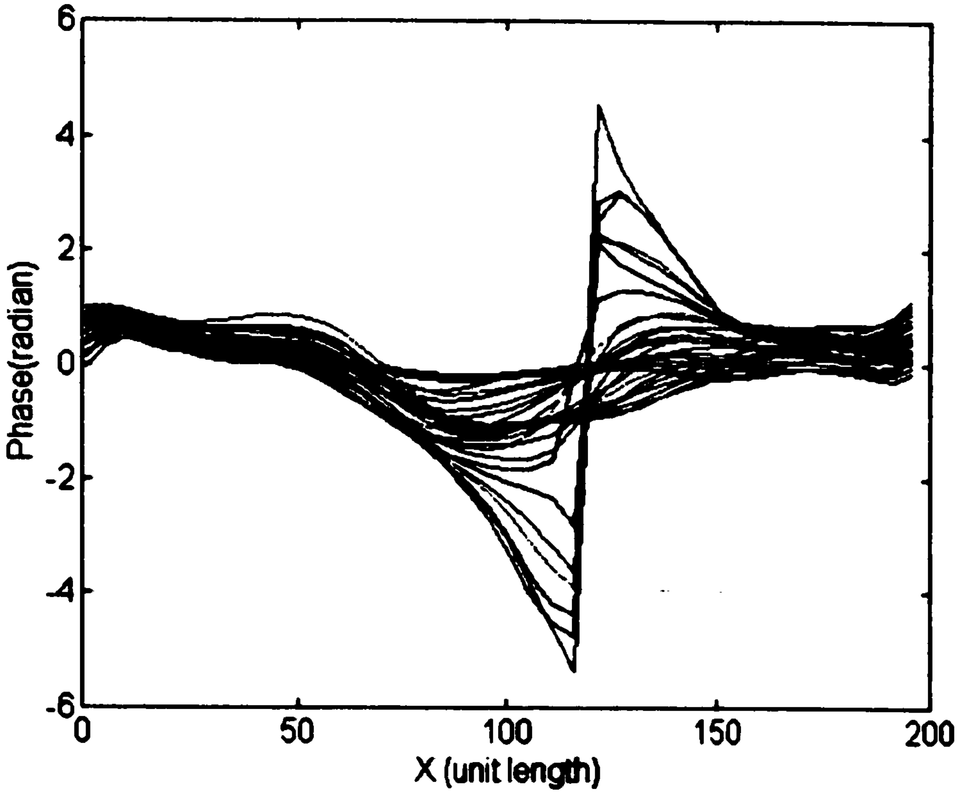

Figure 3.3b The continuous phase profile

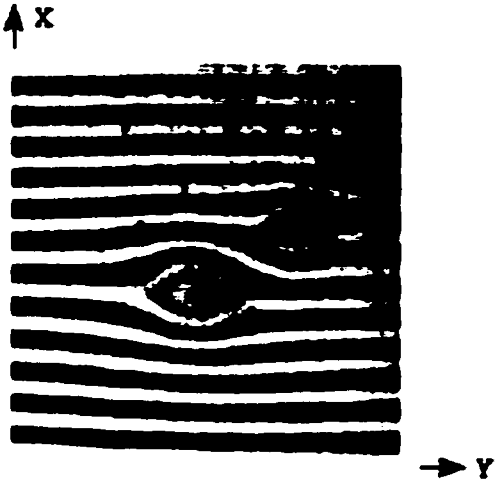

Fig.3.4a The grating image with two indents(dent 1 and 2)

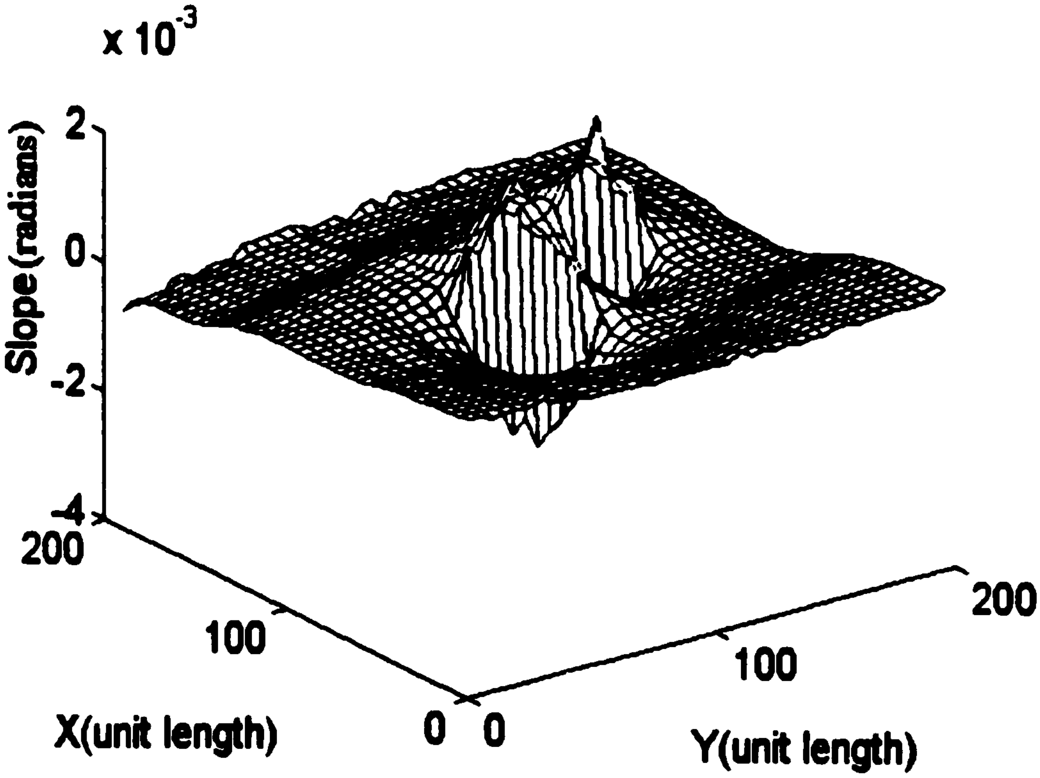

Figure 3.4b The slope of the surface with dent 1 and 2 calculated by the columnwise DFT along the x direction

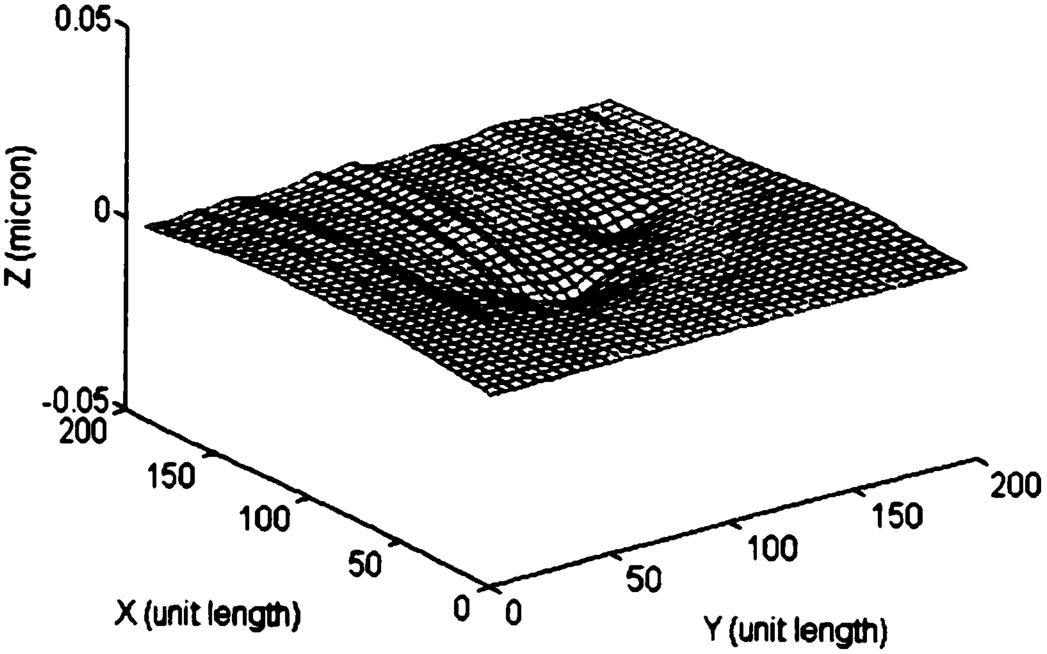

Figure 3.4c The contour of the surface with dent 1 and 2 displayed in 3D

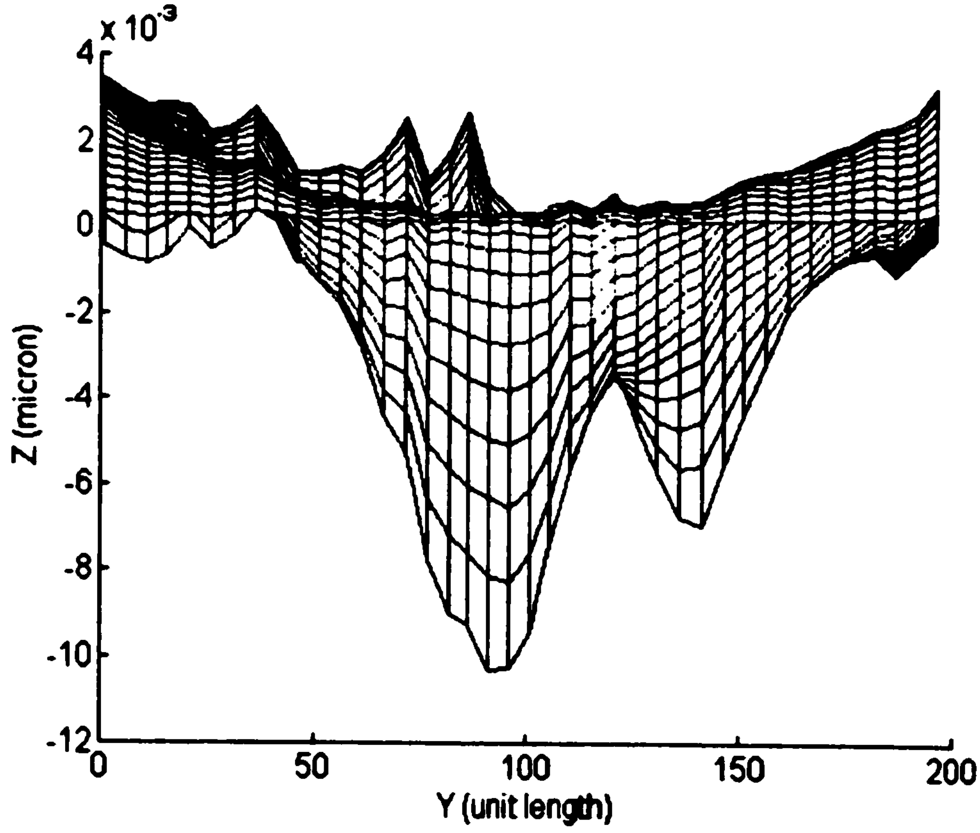

Figure 3.4d The contour of the surface with dent 1 and 2 displayed in 2D

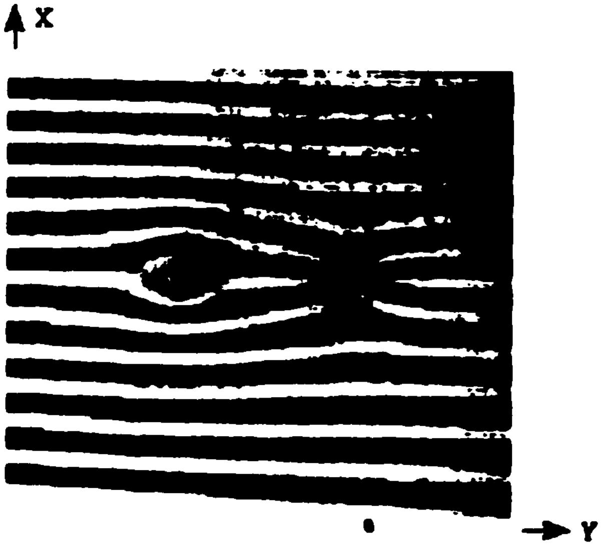

Figure 3.5a The grating image with one indent(dent 3) and one outdent(dent 4)

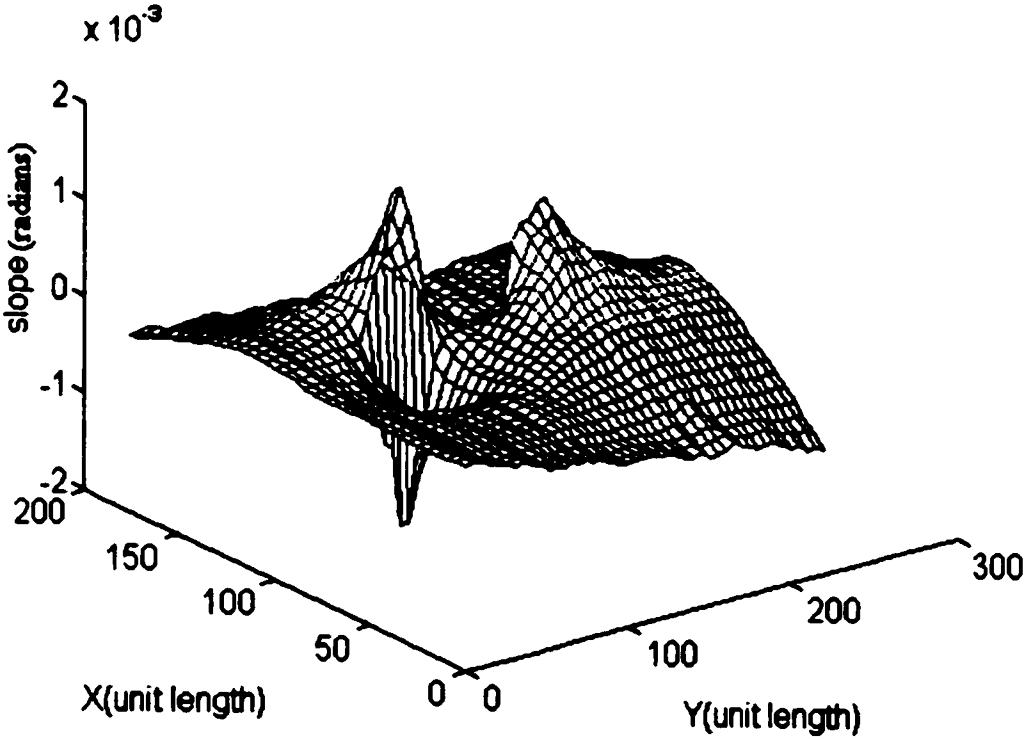

**Figure 3.5b** The slope of the surface with dent 3 and 4 calculated by

the columnwise DFT along the x direction

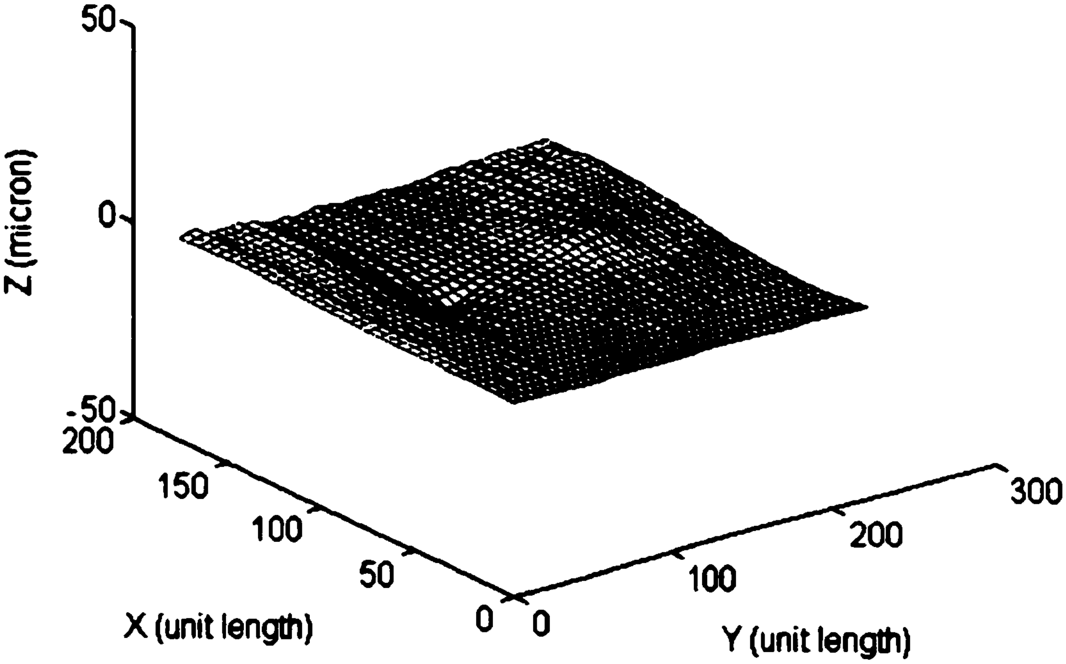

Figure 3.5c The contour of the surface with dent 3 and 4 displayed in 3D

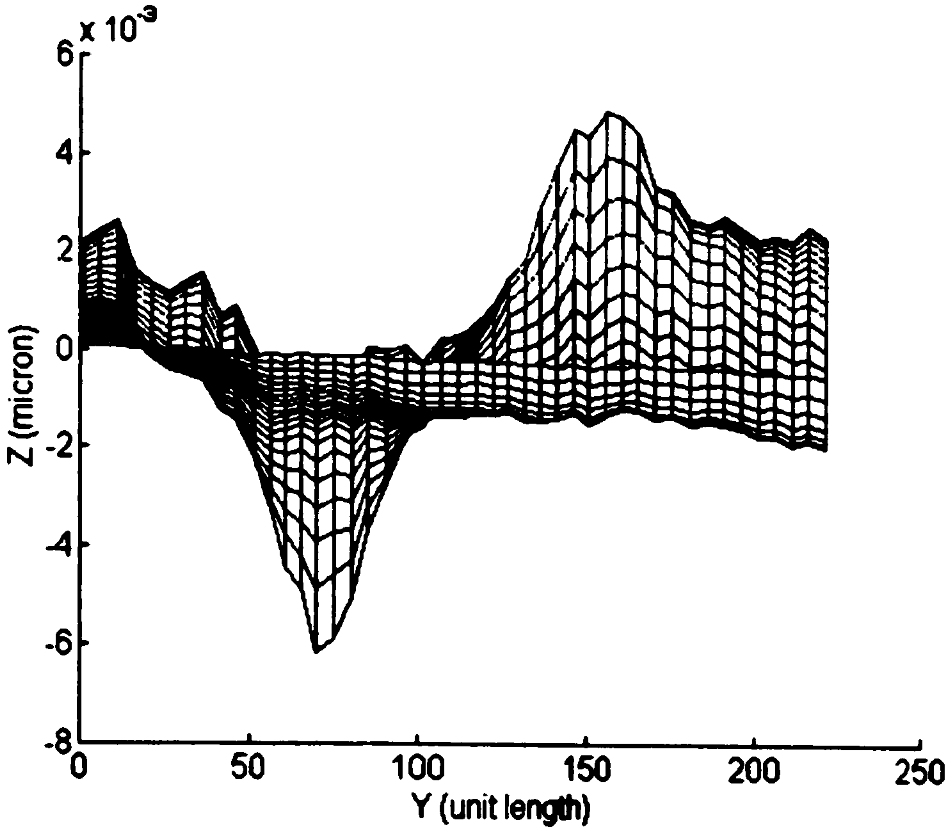

Figure 3.5d The contour of the surface with dent 3 and 4 displayed in 2D

| Dent | Columnwise DFT | Rank machine |
|---|---|---|
| 1 | -6.0μ | -6.0μ |
| 2 | -10μ | -9.0μ |
| 3 | +5.0μ | +4.5μ |
| 4 | -6.0μ | -5.5μ |

Table 3.1 The comparison of the columnwise DFT method with physical measurement by the Rank Taylor Hobson machine

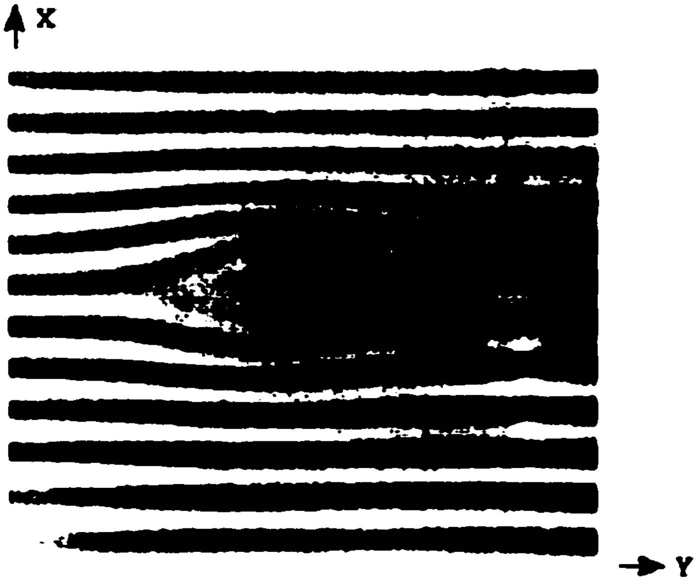

Figure 3.6a The grating image with an indent

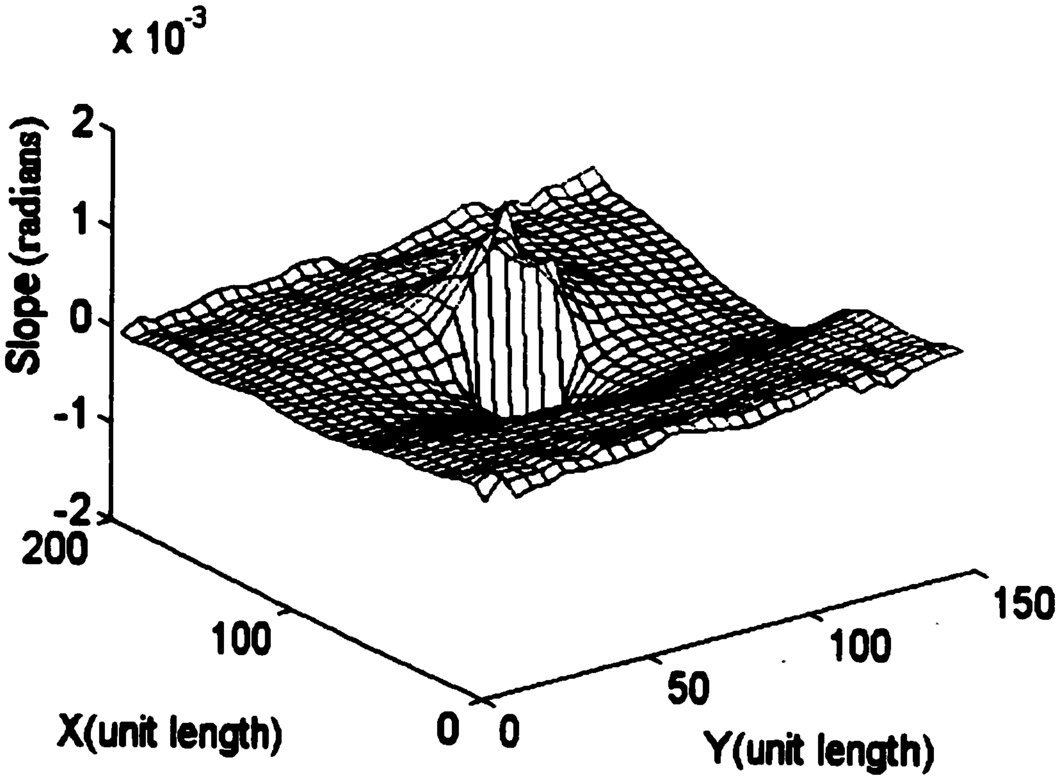

Figure 3.6b The slope of the surface with the indent calculated by the columnwise DFT along the x direction

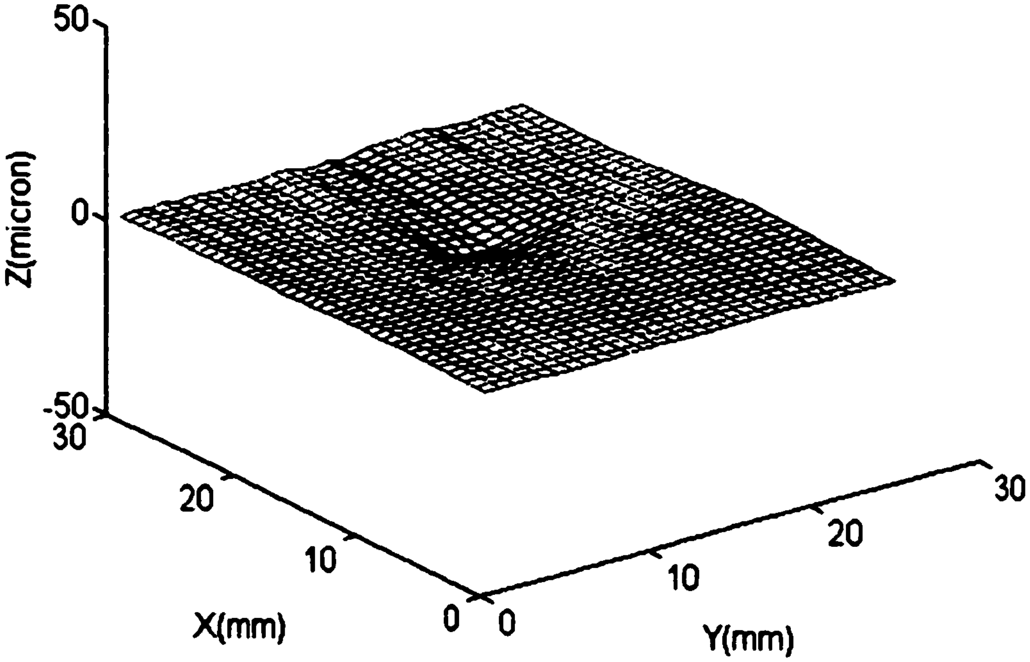

Figure 3.6c The contour of the surface with the indent calculated by retroreflective grating analysis and displayed in 3D

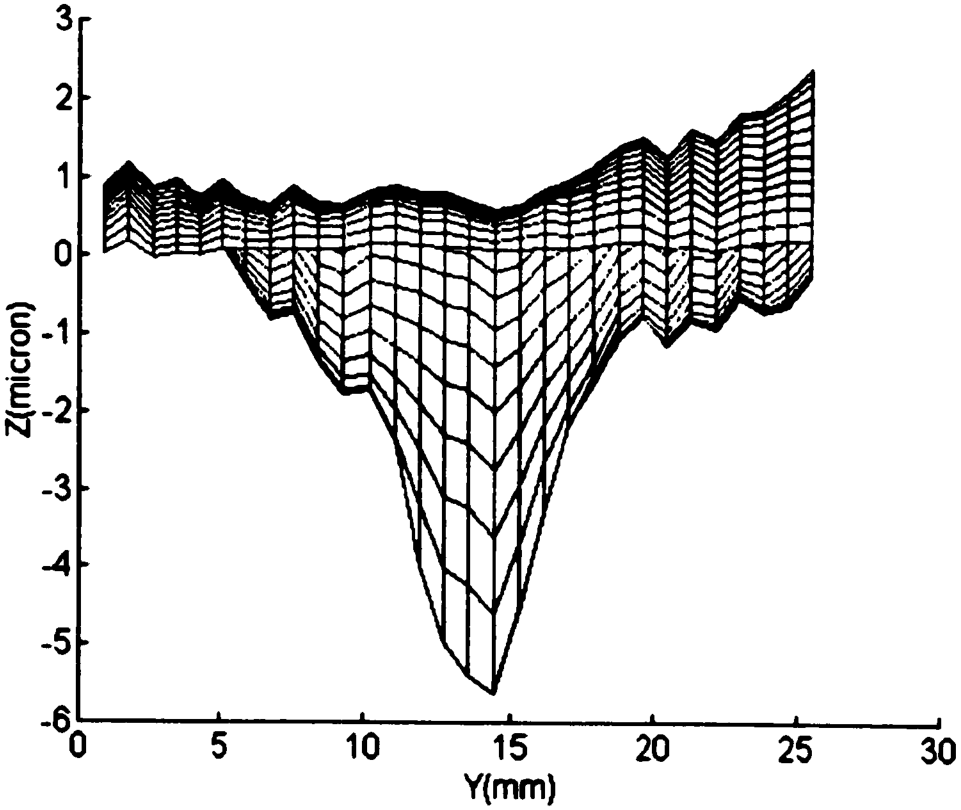

Figure 3.6d The contour of the surface with the indent calculated by retroreflective grating analysis and displayed in 2D

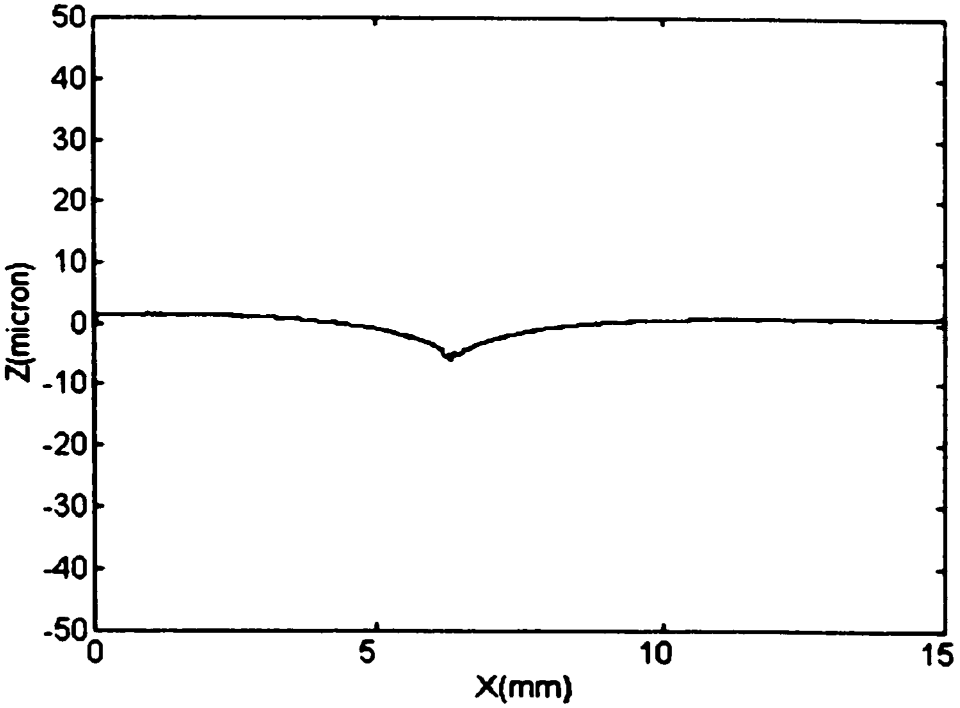

Figure 3.7a The profile measured by the Rank Taylor Hobson machine through the center of the indent

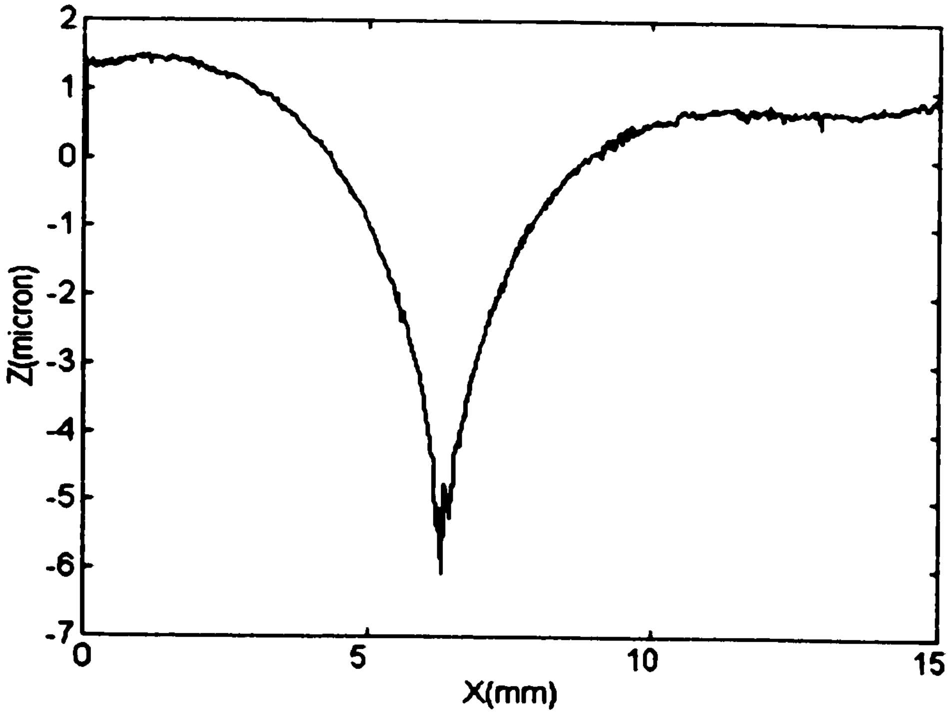

Figure 3.7b The maximum depth measured by the Rank Taylor Hobson machine through the center of the indent

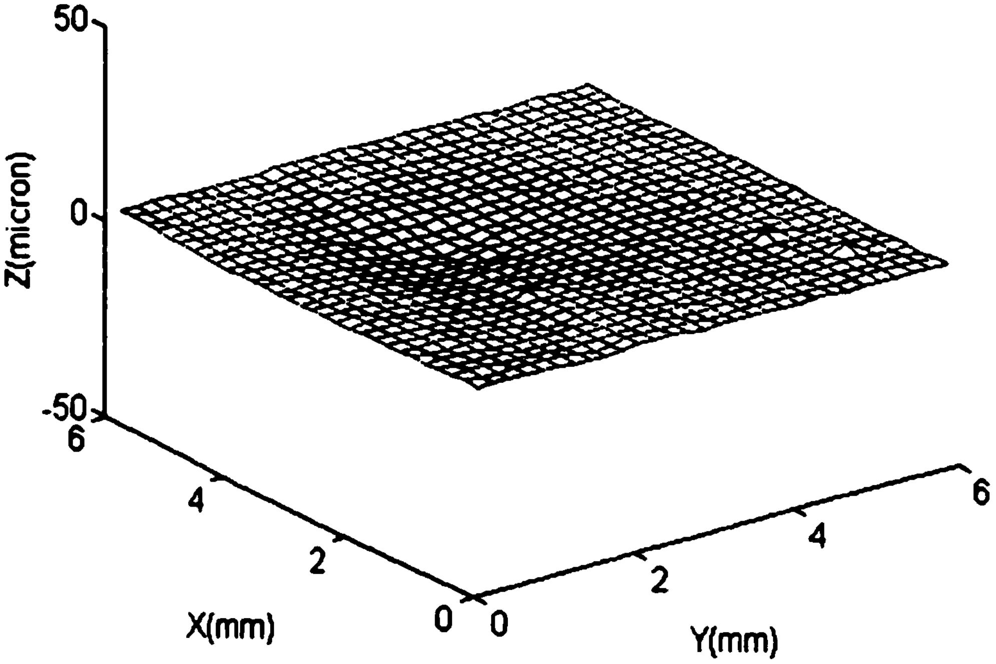

Figure 3.8a The surface contour measured by the CMM

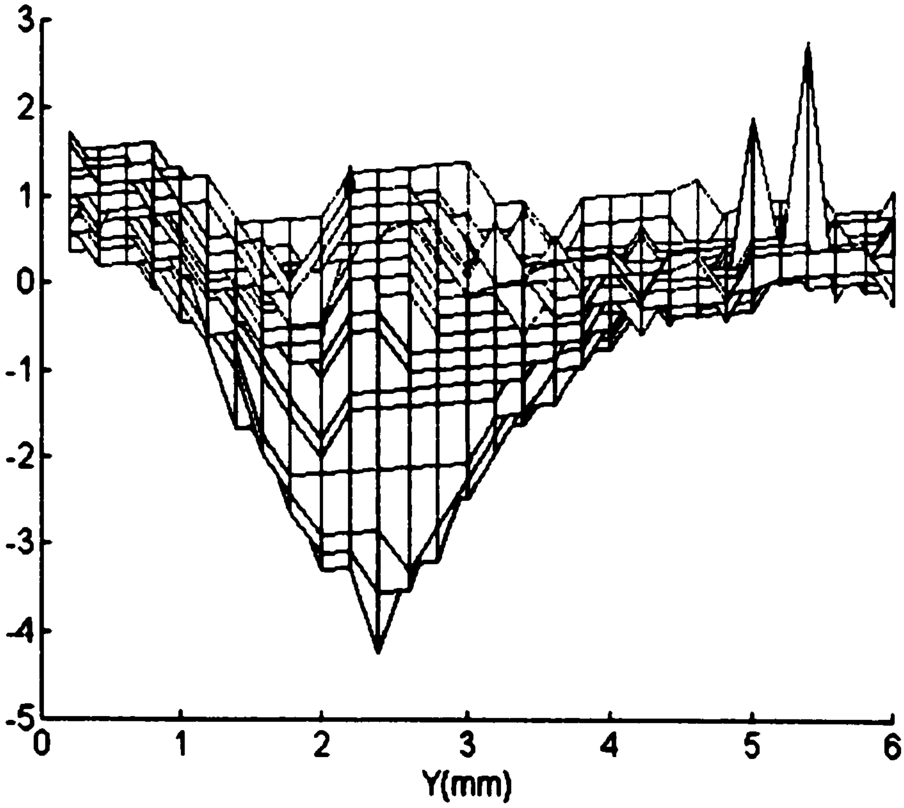

Figure 3.8b The maximum depth measured by the CMM

| Method | Maximum Contour Measurement | Comparison |
|---|---|---|
| The DFT method | -6.0 microns | |
| Taylor Hobson Machine | -5.5 microns | 8.33% |
| Coordinate Measurement Machine | -4.5 microns | 25.0% |

Table 3.2 The comparison of DFT retroreflective grating analysis with physical measurements

# Chapter 4

# Retroreflective Grating Analysis by Phase Shifting Technology(PST)

## 4.1 Introduction

Phase Shifting Technology(PST) is a highly accurate data acquisition and analysis method that efficiently utilizes several frames of information for each measurement. The origins of the idea seem to date from the early days of photoelastic interferometry when simple compensators were used to improve measurements of birefringence. The approach has gained popularity with the advent of powerful microcomputers and improved electronic imaging technology. It has been successfully used with interferometers, projection grids, moiré methods, etc.([59]~[65]) to produce surface contours and deformation measurements. In this present work, the advantages of phase shifting have been applied to the retroreflective grating technique, yielding a system capable of recording a phase shifted grating for the slope and out-of-plane displacement measurement of a sample surface. Using this method, the phase of a grating of interest can be determined at each pixel location, so that the resolution of the phase measurements is limited primarily by pixel discrimination and geometry. The relative phase can be measured at any point on the sample surface independent of the background intensity and grating contrast.

## 4.2 Modeling the grating image

An example of the system arrangement for retroreflective grating analysis by the phase shifting method is shown in Figure 4.1, which is similar to the example of system arrangement of retroreflective grating analysis by the Fourier method. Here, phase shifting is induced by moving the grating, typically one quarter of the grating pitch each time.

If the surface of the sample is very flat and has no flaw, a uniform grating pattern is observed. Conversely, if there are some slope related flaws on the surface, image of the grating will be deformed due to the variation of slope. The grating must also be given a rigid body shift in one direction. The intensity of the image containing the deformed and shifted grating pattern can be modeled as

$$i(x,y) = a(x,y) + b(x,y)\cos[(2\pi / p)x + \Phi(x,y) + \alpha] \tag{4.1}$$

with

$$\Phi(x,y) = 4\pi n\theta(\mathrm{x},\mathrm{y}) \tag{4.2}$$

where a(x,y) and b(x,y) represent the unwanted errors arising from the variations of the background intensity and grating contrast, respectively; p is the pitch of the grating; Φ(x,y) is the phase of the deformed grating; α is a known added phase difference; θ is the local slope of the surface of the specimen; and n(n=L/p) is the optical amplification of the system; L is the distance between the specimen surface and retroreflective screen.

## 4.3 Algorithm

Many different algorithms for the determination of phase Φ(x, y) have been published, and others are appearing at a rapid rate. Some techniques change the phase Φ(x, y) by a known amount between intensity measurements, whereas others integrate the intensity while the phase Φ(x,y) is being shifted. The first is the so-called phase-stepping technique, and the second is usually referred to as an integrating-bucket technique[21]. According to the number of recorded intensity measurements, the phase can be calculated using a variety of methods, such as least-squares, three-step, four-step, Carre technique, etc. Because there are three unknowns(a(x,y), b(x,y) and Φ) in Eq.(4.1), a minimum of three recorded measurements is necessary to determine the phase Φ(x,y).

The method adopted for this work is the well-known three step(or four frames) algorithm. In this case, α=0, π/2, π, and 3π/2. The phase at each point is

$$\Phi(x,y)=\tan^{-1}\left(\frac{i_4(x,y)-i_2(x,y)}{i_1(x,y)-i_3(x,y)}\right) \tag{4.3}$$

where $i_1(x,y)$ through $i_4(x,y)$ correspond to the intensities at a point x for the four values of α, respectively. Because Φ(x,y) is determined by the differential measurement of intensity at points quite close together, the variations a(x,y) and b(x,y) are very much reduced. The phase so obtained is modulo 2π. These have to be unwrapped to produce the desired phase map.

To calculate the local slope of the sample surface, we rearrange the Eq.(4.2) and have

$$\theta(x,y) = \Phi(x,y) / (4\pi n) \tag{4.4}$$

The depth of each point on the surface of the specimen d(x,y) can be found by integrating slope in the x direction.

$$d(x,y) = \int \theta(x,y)dx \tag{4.5}$$

## 4.4 Experiment

In the following experiment, the parameters of the system configuration are set as p=1.00cm(the pitch of the grating), n=270(the amplification of the optical configuration), and Δx=1.35mm(unit length in x direction), and Δy=1.53mm(unit length in y direction). The experimental steps were as follows:

(1) A small indent was made on a 10cm x 10cm metal sheet with 1.00mm thickness.

(2) The linear grating with rectangular profile and 1.00cm pitch is placed on the retroreflective screen.

(3) Four frames of images shown in Figure 4.2a through Figure 4.2d were captured corresponding to the phase shifts of α=0, π/2, π and 3π/2, respectively. This was accomplished by mounting the grating on a linear slide whose position can be measured ±0.1mm which in this case is equivalent to

$$\frac{0.1mm}{10mm} \times 360\ \deg rees = 3.6\ \deg rees \quad or \quad \frac{0.1mm}{10mm} \times 2\pi\ rad = 0.0628\ rad \tag{4.6}$$

(4) The phase map modulo $2\pi$ shown in Figure 4.3a was calculated according to Eq.(4.3) and the desired phase map shown in Figure 4.3b was reconstructed by an unwrapping algorithm.

(5) The local slope of the sample shown in Figure 4.4 was calculated according to Eq.(4.4).

(6) The contour of the sample surface shown in Figure 4.5 was found according to Eq.(4.5) and the maximum depth of the indent on the sample surface shown in Figure 4.6 is about 5.5 microns.

In order to verify the accuracy of the three-step(four frames) PST technique, the profile was measured through the center of the same dent by using a Rank Taylor Hobson machine. Table 4.1 compares the maximum excursions as obtained from retroreflective grating analysis with conventional physical contacting measurement by the Rank Taylor Hobson machine.

The experiment shows that the method can determine the defect size, shape and polarity(indent/outdent).

## 4.5 Conclusion

Advantages:

1. Retroreflective grating analysis by PST has been used to determine the contour of a

sheet metal dent and confirmed by mechanical contacting measurement.

2. This procedure also determines polarity i.e. indent VS outdent.
3. It is capable of measuring small dents of the order of 10 microns depth.
4. Because the method is optical, it is noncontacting.
5. The method generate 3D contour of a significant area rather than a point by point measurement(CMM) or a linear scan(Taylor Hobson Technology).
6. It yields results much faster than CMM or Taylor Hobson Technology.
7. It determines the phase independently at each point without need to consider data from other points in the image.
8. It is not like the DFT method which has a limitation to the second derivative of the surface under test.
9. Because of the pixel size, many pixels of information each from close proximity are used to determine the phase. This leads to better resolution as compared to the DFT method.
10. The PST method can eliminate the variations in background and grating contrast as shown in equation 4.3. It is more powerful than simply observing the distorted grating image and ordering the grating image centers.

Disadvantages:

1. It requires four frames of image. The grating has to be physically shifted three times each by a precise amount.

2. Undersampling leads to cumulative error which is propagated to other areas.
3. The surface under test must be quasi flat and specular.
4. Dsight® must be sensitive enough to identify and locate any error which is subsequently scanned.
5. It is not applicable for dynamic applications or instances where vibrations make it difficult to constantly step.

An error analysis of the PST method is presented in Appendix C.

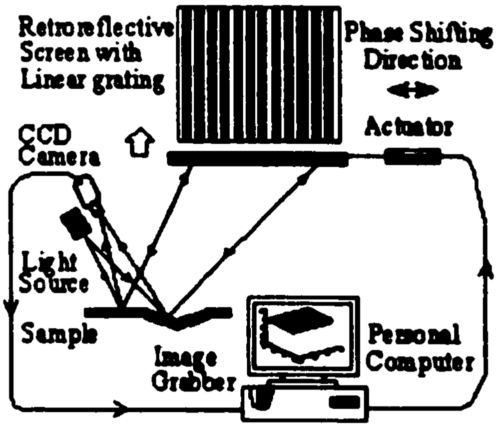

Figure 4.1 An example of system arrangement of retroreflective grating analysis by the phase shifting method

Figure 4.2a The grating image for an indent with phase shift $\alpha$=0

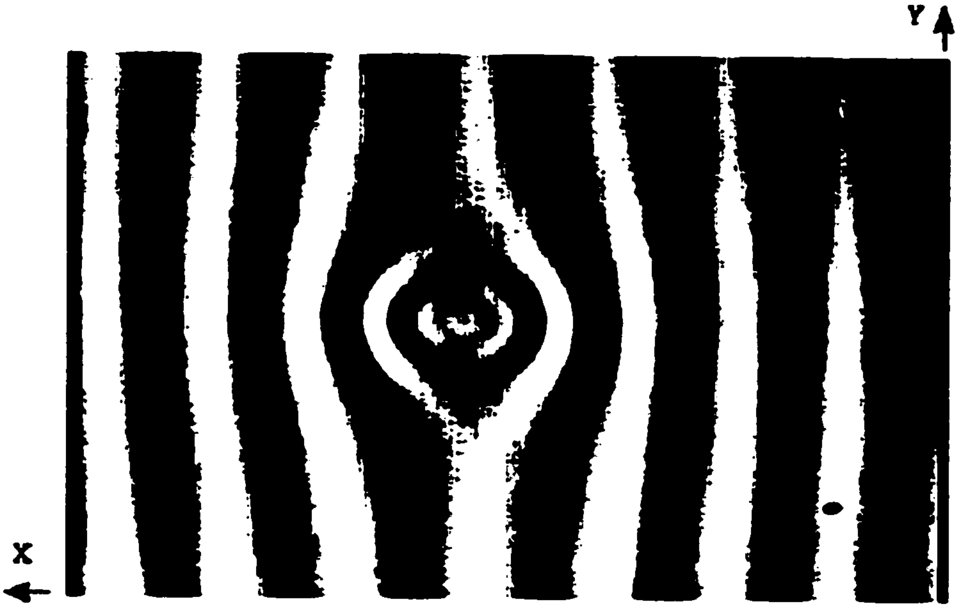

Figure 4.2b The grating image with phase shift $\alpha=\pi/2$

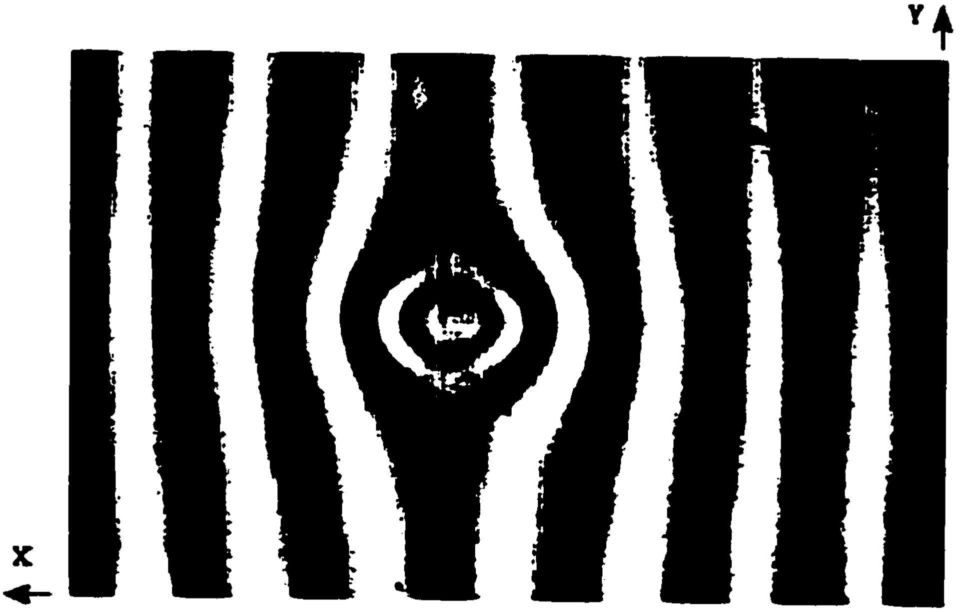

Figure 4.2c The grating image with phase shift α=π

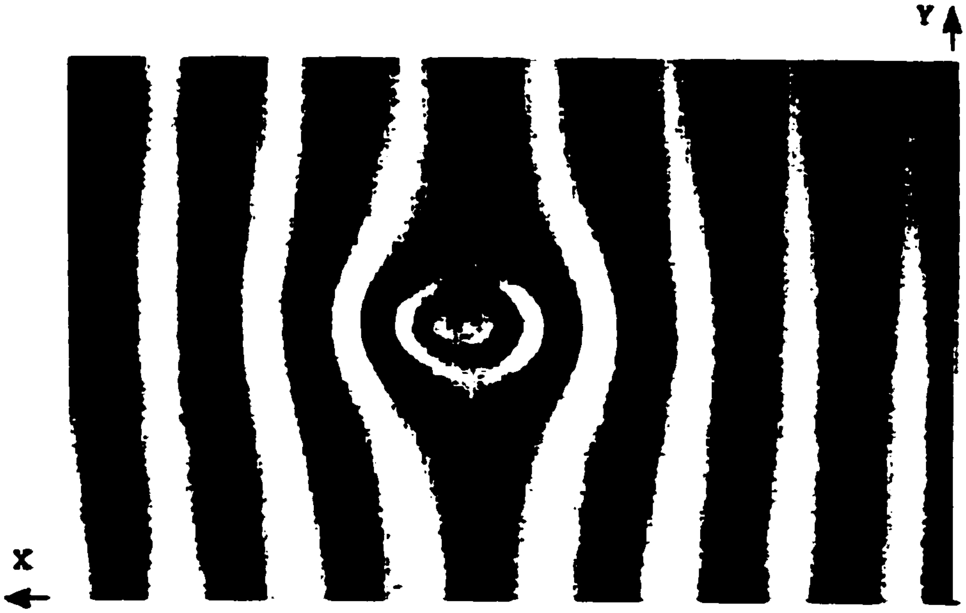

Figure 4.2d The grating image with phase shift $\alpha=2\pi/3$

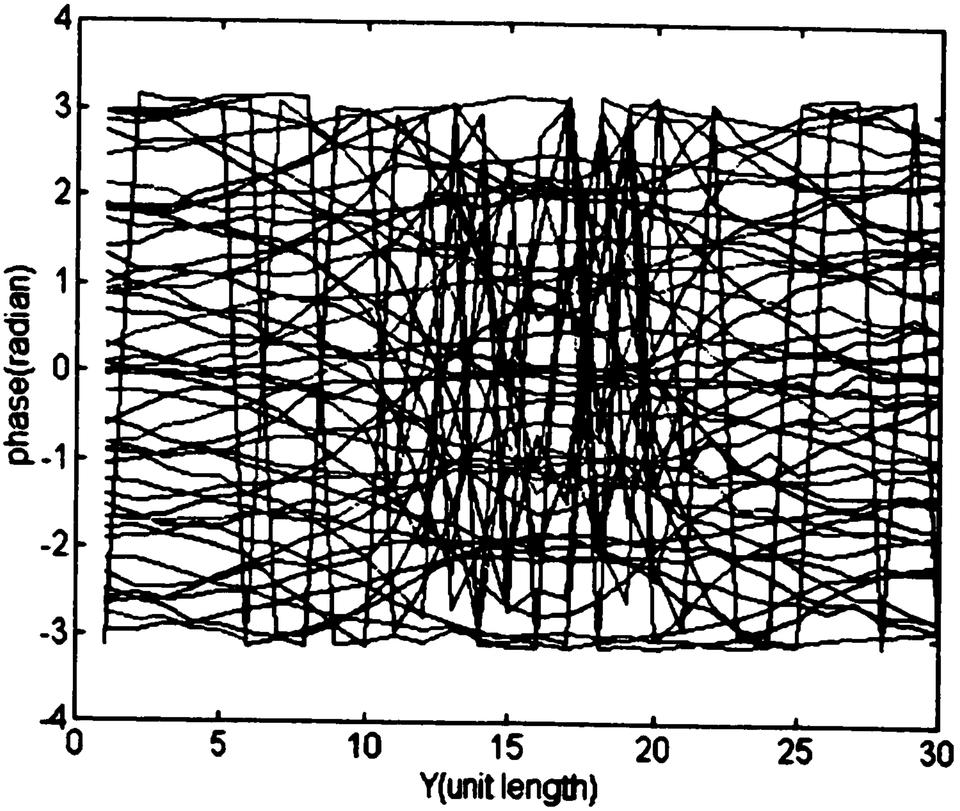

Figure 4.3a The phase map modulo 2π

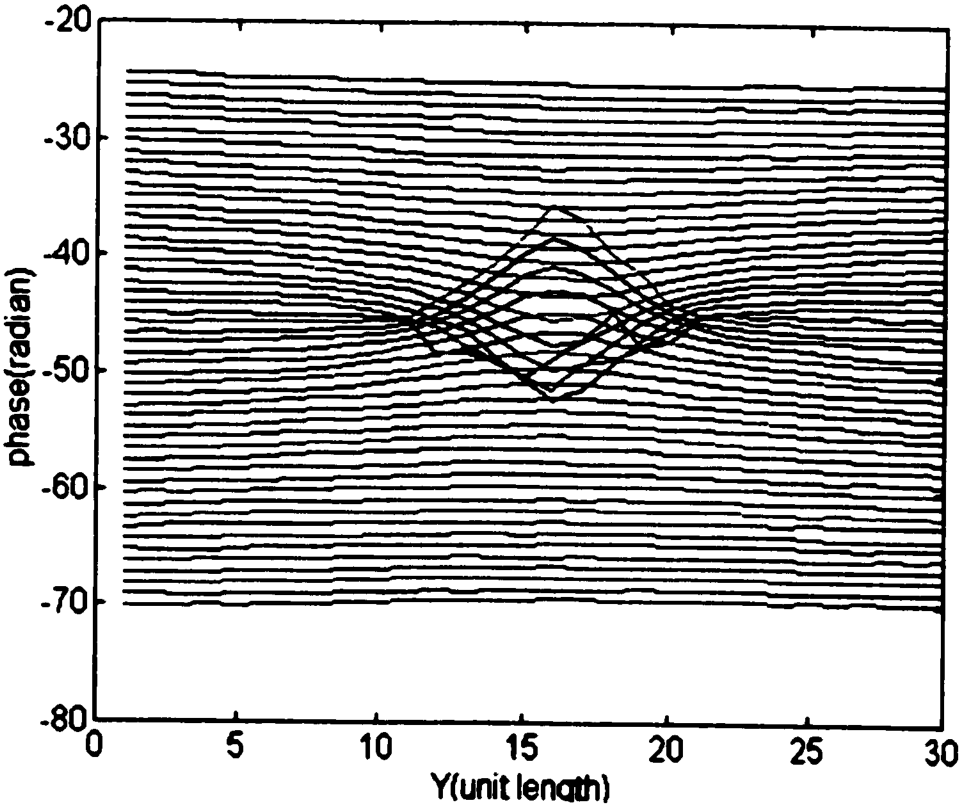

**Figure 4.3b** The desired phase map$[(2\pi/p)x+\Phi(x, y)]$

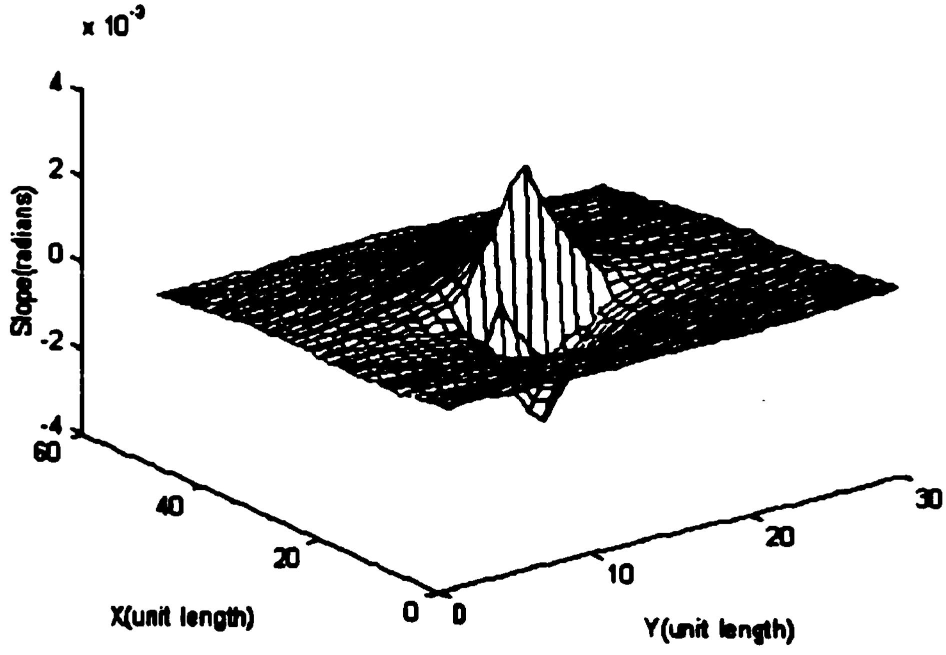

Figure 4.4 The slope of the sample surface

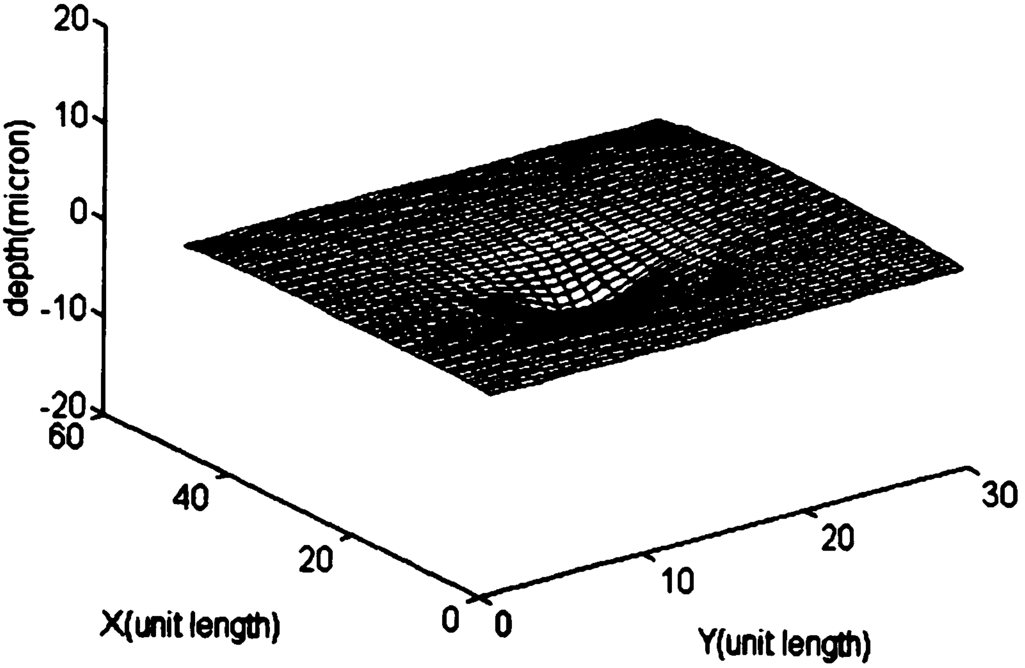

Figure 4.5 The contour of the sample surface

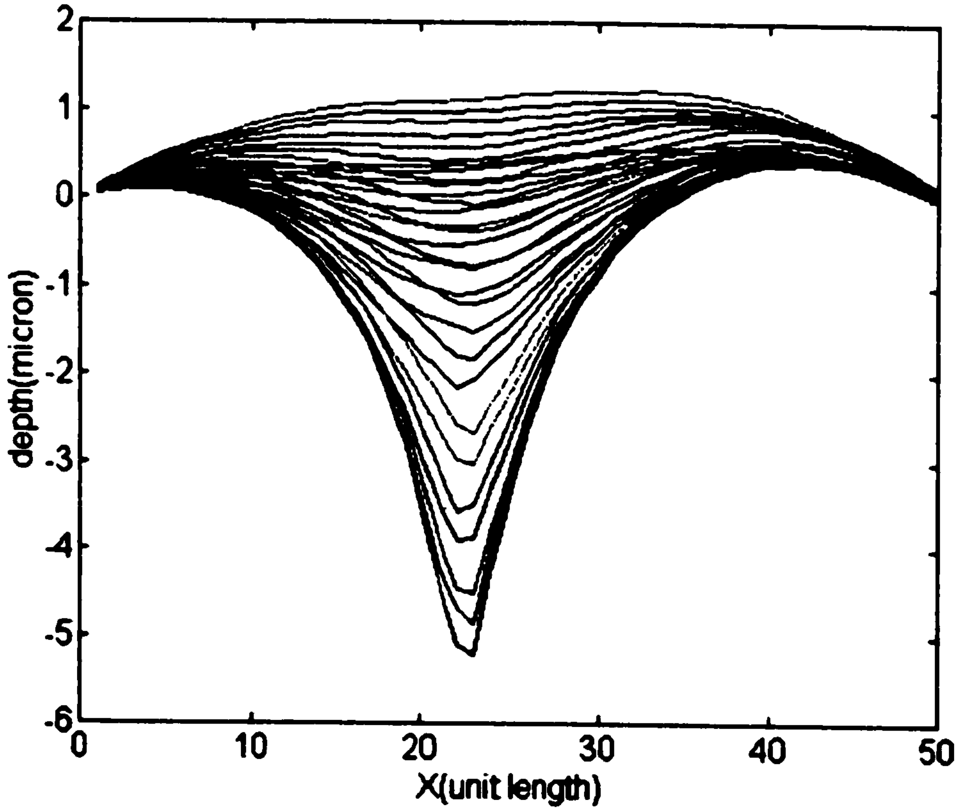

Figure 4.6 The maximum depth of the indent on the sample surface

| Method | Maximum Contour Measurement |
|---|---|
| Three-step PST | -5.5 microns |
| Rank machine | -6.0 microns |

Table 4.1 The comparison of the three-step PST method with physical measurement by the Rank Taylor Hobson machine

# Chapter 5

# Retroreflective Projection Gratings

## 5.1 Introduction

In previous methods, the grating was physically attached to the retroreflective screen. This makes it cumbersome to change the grating pitch or geometry or to mechanically move the grating in order to use phase shifting technology. In this work, the retroreflective projection grating method is investigated. It is more flexible to change the properties of the grating or shift it, because the grating is optically generated by projection. Three different types of optical arrangement have been studied. The method is tested with some dents on a piece of bright sheet metal.

## 5.2 Optical configurations

The essential components for the retroreflective projection grating technique are a camera, a projector, the surface to be inspected and a retroreflective screen. There are three kinds of optical configuration which determine how to position the camera and projector.

Shown in Figure 5.1a is the first optical arrangement. Light rays from the projector carrying the grating image strike the surface of the sample, reflect off it and strike the retroreflective screen. The properties of this screen is that it can efficiently return any light back to the source but diverged over a small angle. If we focus the projector on the screen, the grating can be observed by the camera located in front of the retroreflective screen for a small angle ψ. In the process, the grating will be modulated if there are some slope-related defects on the surface of the sample. Any grating distortion is due to contour amplitude at a given angle of incidence as in classical optical triangulation. But the experiments show that the modulation is not sufficient enough to make the measurement possible.

In stead, we put the camera close to the projector as is shown in the second configuration of Figure 5.1b. As before, light rays from the projector strike the surface, reflect off it and strike the retroreflective screen. Any reflected rays which reach the screen are re-directed to once again reflect off the surface, after which they are naturally aimed towards the vicinity of the projector. Because the camera lens is near the projector it can collect a useful percentage of those returned rays. This optical process is a two-pass phenomenon in which the surface is illuminated twice, once by the projector and once by the retroreflective screen. With each pass, a defect modulates the grating once and creates a visible 'signature' which is dependent on the defect size, shape, polarity and the illumination. The first pass forms the primary signature on the screen and the second-pass forms the "secondary" signature on the surface. The image captured by the camera consists of these two signatures superimposed. The second signature gives a better signal to noise ratio and is more reliable. Experimentation has shown that, with proper configuration, the primary signatures can be subdued to such an extent to make them essentially invisible.

In order to completely eliminate the primary signature, the projector is put in front of the retroreflective screen and the grating image focused on it as is shown in the third configuration of Figure 5.1c. Light rays from the projector carrying the grating are focussed onto the retroreflective screen and form a uniform grating pattern on it. The reflected light is re-directed to reflect off the surface of the sample towards the vicinity of the camera for a small angle ψ. In this process, the grating is modulated only once and tests show that the modulation is sufficient to make a measurement.

## 5.3 Summary

For the first configuration in Figure 5.1a:

The advantage is that the grating is modulated only once, and

The disadvantage is that the modulation has a weak signal/noise ratio.

For the second configuration in Figure 5.1b:

The advantages are:

(1) The equipment is compact.

(2) The modulation has sufficient signal/noise ratio.

The disadvantage is that the grating is modulated twice.

For the third configuration in Figure 5.1c:

The advantages are:

(1) The grating is modulated only once

(2) The modulation has sufficient signal/noise ratio.

The disadvantage is that the camera and the projector are separated.

## 5.4 Experiment

In the following experiment, the second configuration of Figure 5.1b is used for retroreflective grating metrology. The parameters of the configuration are set as p=1.00cm(the pitch of the grating), n=270(the amplification of the optical configuration), dx=0.75mm(unit length in x direction), and dy=0.85mm(unit length in y direction).
A small indent was made on a 10cm x 10cm bright metal sheet with 1mm thickness. The linear grating with rectangular profile and 1.00cm pitch was projected onto the retroreflective screen. The grey level of the image captured by camera is shown in Figure 5.2a and Figure 5.2b. The columnwise DFT method is applied to extract the phase information. The local slope of the sample surface is shown in Figure 5.3. Figure 5.4 shows the contour of the specimen surface in the dimension of microns.

## 5.5 Conclusion

The second and third configurations are each useful because the grating modulation is due to sample slope related information, which has the advantage of light lever arm amplification. The equipment is more compact in the second configuration while the third one has the grating only being modulated once.

The experiment shows that the second configuration results with better signal/noise ratio and ease of application. The third configuration will be used for the measurement of surface waviness in the next chapter.

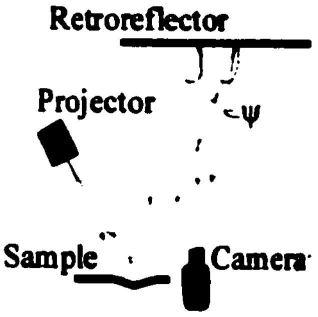

Figure 5.1a The first configuration

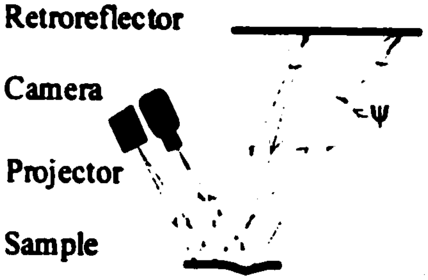

Figure 5.1b The second configuration

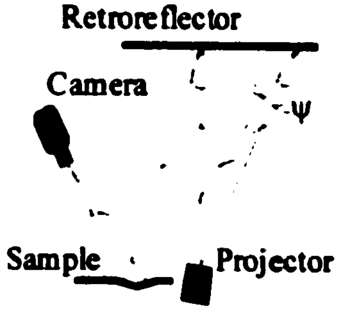

Figure 5.1c The third configuration

Figure 5.2a For an indent, the grey level of the image captured by the camera

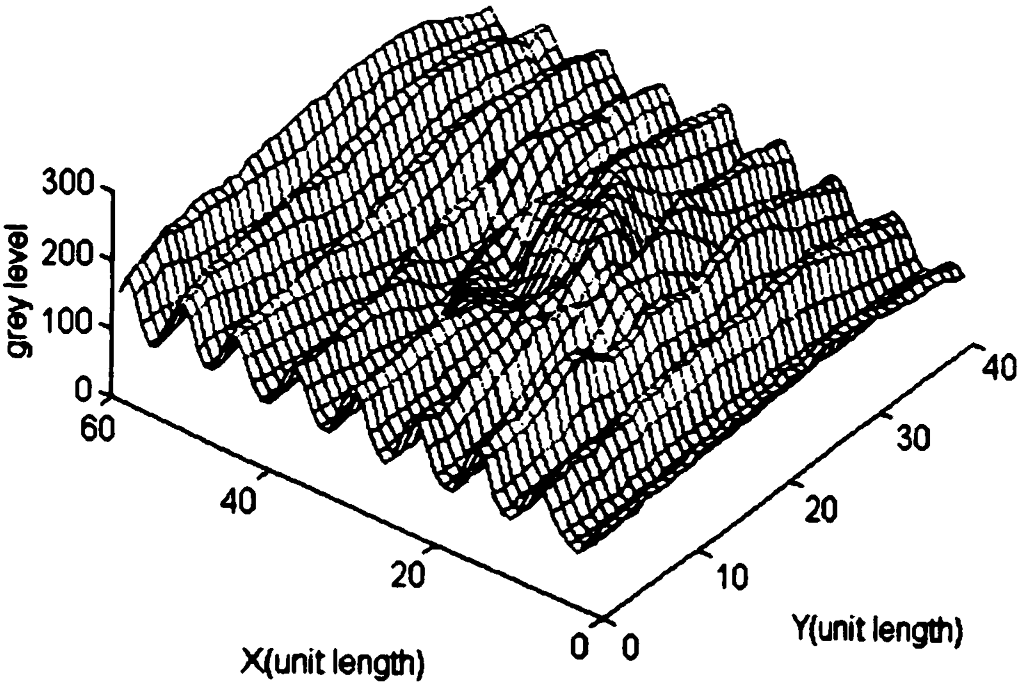

Figure 5.2b The grey level of the image displayed in three dimensions

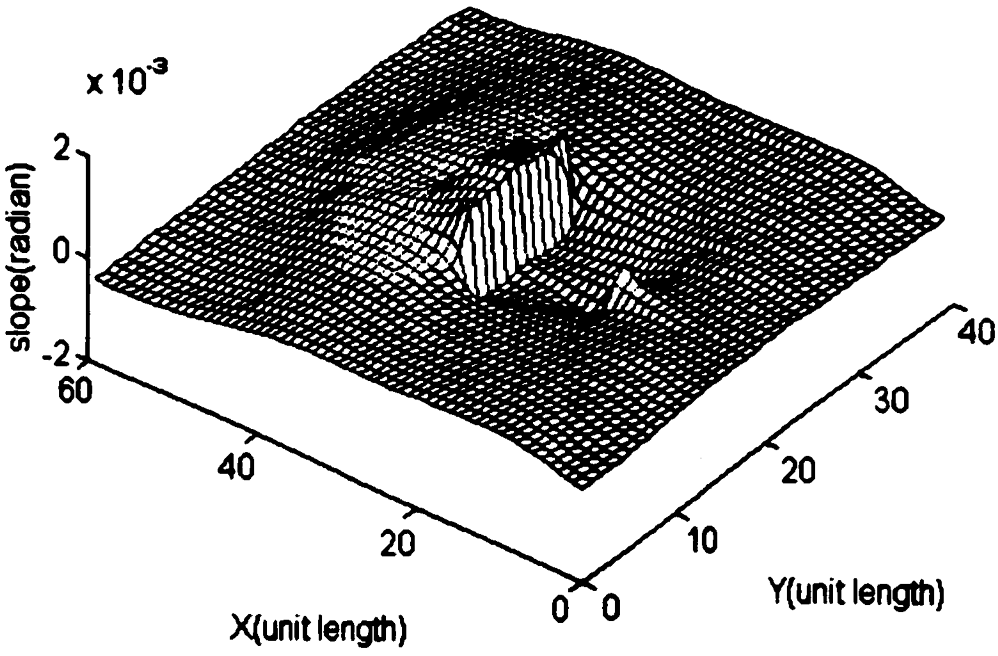

Figure 5.3 The slope of the sample surface

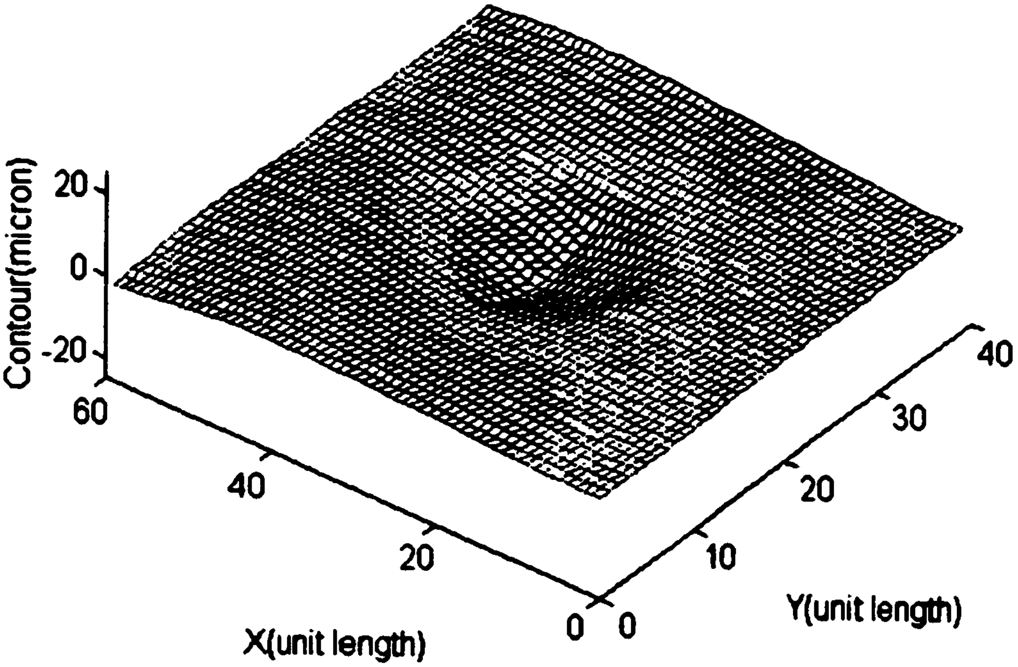

Figure 5.4 The contour of the sample surface

# Chapter 6

# Analysis of 3D Surface Waviness on Calibrated Artifacts by Retroreflective Metrology

## 6.1 Introduction

Confirming measurements using the Taylor Hobson and CMM systems introduce their own errors as both are contacting measurements. As the CMM probe has a physical finite size hence the question "where is the contact point on the Renishaw probe ball". Both systems apply a force, small, but sufficient to result in the deformation of the test surface. However, two calibrated waviness artifacts became available from Diffrato®. These were manufactured to calibrate Dsight® for waviness measurements. As these artifacts are themselves specular and of known contour they can be used in a noncontact measurement to compare to these retroreflective grating measurements.

Further these retroreflective grating measurements result by definition and results need not be calibrated whereas the Taylor Hobson, CMM, and Dsight® methods all require calibration.

In this work, the surface waviness of the standard artifacts was measured by the retroreflective grating metrology. The grating image was produced by projection, using the third optical configuration. The three-step algorithm of Phase Shifting Technology

(PST) was applied to analyze the image.

## 6.2 Standard Artifacts

The need to set surface quality standards for process control is particularly important for those products whose appearance is critical to customer acceptance. The dimensional aspects of surface quality can be divided into five distinct regions. A widely accepted definition of the regions is given in table 6.1[89]. In fact, the only dimensional region that has acceptable calibrated artifacts and measurement procedures is the surface roughness region.

The two regions examined here are long and short waviness. There are reference artifacts available at Diffracto® for use in calibration of surface measurement systems such as the Diffrato D SIGHT® AS2 and TPS systems. Those artifacts provide some standardization and traceability to surface waviness measurement.

These artifacts are flat aluminum plates with diamond turned sine waves cut into one surface. This surface is then optically overcoated to provide protection against oxidation and scratches. A schematic of these artifacts is shown in Figure 6.1. The dimension of the plates is 305±0.25mm by 305±0.25mm with 25.0±0.25mm thickness. The period of waviness on the surface is 40±0.25mm. Three different artifacts with 0.016±0.001mm, 0.008±0.001mm and 0.000±0.001mm peak-to-peak waviness amplitudes were tested. The surface function generation always begins at center point, A, with amplitude at a minimum.

The artifact amplitude was guaranteed to be accurate to ±0.001mm over the entire surface, using a $CO_2$ laser interferometer measurement. However like a typical optical element guaranteed to some accuracy, it is unknown where specifically this discrepancy might occur on the artifact.

## 6.3 Nonlinear model for the optical process

Shown in Figure 2.5 is the example of the optical configuration for retroreflective grating metrology. In the section 2.3, a linear model for the optical process is derived in the equations 2.1 and 2.2, which are repeated here for convenience:

$$\delta = L[\tan(\beta+2\theta)-\tan(\beta)] \tag{2.1}$$

$$\delta = 2L\theta \tag{2.2}$$

The Taylor series of $\tan(\beta+2\theta)$ can be expressed as

$$\tan(\beta+2\theta) = \tan(\beta) + \frac{(2\theta)^1}{1!}\frac{d}{d(2\theta)}[\tan(\beta)] + \frac{(2\theta)^2}{2!}\frac{d^2}{d(2\theta)^2}[\tan(\beta)] + \Lambda \tag{6.1}$$

Since the previous experiments show that $\theta$ is usually less than 0.005, we can neglect the terms of order higher than one in the equation 6.1. Substituting it into the equation 2.1, we have

$$\begin{gathered} \delta = L\left\{\tan\beta + 2\theta \cdot \frac{d}{d(2\theta)}[\tan(\beta)] - \tan\beta\right\} \\ \delta = L \cdot 2\theta \cdot \frac{d}{d(2\theta)}[\tan(\beta)] = 2L\theta\frac{1}{\cos^2\beta} = 2L\theta(1+\tan^2\beta) \end{gathered} \tag{6.2}$$

The phase of a deformed grating is described in the equation 3.3, which is repeated here for convenience.

$$\Phi(x, y)=(2\pi/p)\delta=(2\pi/p)(2L\theta)=4\pi(L/p)\theta=4\pi n\theta(x, y) \tag{3.3}$$

If we substitute the equation 6.2 into the equation 3.3, we have

$$\begin{aligned}\Phi(x,y) &= (2\pi / p)\delta = (2\pi / p)\cdot 2L\theta(1+\tan^2\beta)\\ \Phi(x,y) &= 4\pi(L/p)\theta(1+\tan^2\beta) = 4\pi n(1+\tan^2\beta)\theta(x,y)\end{aligned} \tag{6.3}$$

The equation 6.3 includes the illumination angle $\beta$ into the phase expression. If $\beta$ is relatively small, the equation 6.3 is reduced to the equation 3.3. The relative error between the linear and nonlinear models can be calculated as

$$Error = \left|\frac{4\pi n\theta-[4\pi n\theta(1+\tan^2\beta)]}{4\pi n\theta(1+\tan^2\beta)}\right| = \left|\frac{-\tan^2\beta}{1+\tan^2\beta}\right| = \sin^2\beta \tag{6.4}$$

Figure 6.2 plots the error as a function of $\beta$. Table 6.2 shows the error as $\beta$ changes and shows that, for an error less than 1%, the linear model has a small field of view ($\beta<5°$). In all of the previous experiments, the zone of the indents was small, typically $\beta<1°$.

## 6.4 Amplitude estimation of surface waviness on the standard artifacts

We know that the wavelength of waviness on the surface, $\lambda$, is 40.0mm. The profile through the wave center can be described as a trigonometric sum of order one:

$$Z = C_0 + C_1\cos(2\pi\omega_0 x+\gamma) = A_0 + A_1\cos(2\pi\omega_0 x) + B_1\sin(2\pi\omega_0 x) \tag{6.5}$$

where

Z is the depth of each point on the profile;

$\omega_0$ is the spatial frequency ($=2\pi/\lambda$);

x is the coordinate along the x direction;

$C_0$, $C_1$, $\gamma$, $A_0$, $A_1$, and $B_1$ are the coefficients to be found.

We can use the least squares trigonometric approximation to find $A_0$, $A_1$, and $B_1$. The amplitude of the waviness can be calculated as

$$C_1 = \sqrt{A_1^2 + B_1^2} \tag{6.6}$$

## 6.5 Experiment

In the following experiments, the nonlinear model for the optical process was used with $-12.5° < \beta < 12.5°$, and the waviness amplitude calculated from experimental data by the least squares trigonometric approximation. The surface with 16.0±1.0 microns peak-to-peak amplitude, the surface with 8.0±1.0 microns peak-to-peak amplitude, and a calibrated flat surface were tested.

The parameters of the system configuration are set as

L=2500 mm(the distance between the specimen surface and retroreflective screen), dx=4.36 mm(unit length in x direction), and dy=4.36mm(unit length in y direction), p=40.0 mm(the pitch of the grating on the retroreflective screen) and n=62.5(the amplification of the optical configuration).

The experimental procedure was as follows:

(1) The slide with a linear grating is placed in the projector;

(2) Four frames of image were captured corresponding to the phase shifts of $\alpha=0$, $\pi/2$, $\pi$ and $3\pi/2$, respectively, by physically moving the slide, which is attached to the projector;

(3) The phase map modulo $2\pi$ was calculated by the three-step phase shifting algorithm and the desired phase map was reconstructed by an unwrapping algorithm;

(4) The local slope of the sample was calculated;

(5) The contour of surface waviness was found by integration of the slope.

The four frames of grating images for the standard artifact with 0.016mm amplitude are shown in Figure 6.3a through Figure 6.3d corresponding to the phase shifts of $\alpha=0$, $\pi/2$, $\pi$ and $3\pi/2$, respectively. Figure 6.3e shows the intensity of central slices of the four grating images. Figure 6.3f shows the phase of the central line calculated by the PST method. Figure 6.3g shows the slope of the central line calculated by using the nonlinear model. Figure 6.3h shows the profile of the central line calculated by integration of the slope. Table 6.3a shows the peak-to-peak amplitudes on the profile of the central line. Figure 6.3i shows the error band of the peak-to-peak amplitudes on the central line.

Figure 6.3j shows the peak-to-peak amplitude of the central line calculated by the least squares trigonometric approximation. Table 6.3b shows the error summary of peak-to-peak amplitude measurement.

The four frames of grating images for the standard artifact with 0.008mm amplitude are shown in Figure 6.4a through Figure 6.4d corresponding to the phase shifts of $\alpha=0$, $\pi/2$, $\pi$ and $3\pi/2$, respectively. Figure 6.4e shows the intensity of central slices of the four grating images. Figure 6.4f shows the phase of the central line calculated by the PST method. Figure 6.4g shows the slope of the central line calculated by using the nonlinear model. Figure 6.4h shows the profile of the central line calculated by integration of the slope. Table 6.4a shows the peak-to-peak amplitudes on the profile of the central line. Figure 6.4i shows the error band of the peak-to-peak amplitudes on the central line. Figure 6.4j shows the peak-to-peak amplitude of the central line calculated by the least squares trigonometric approximation. Table 6.4b shows the error summary of peak-to-peak amplitude measurement.

The four frames of grating images for the standard artifact with flat surface are shown in Figure 6.5a through Figure 6.5d corresponding to the phase shifts of $\alpha=0$, $\pi/2$, $\pi$ and $3\pi/2$, respectively. Figure 6.5e shows the intensity of central slices of the four grating images. Figure 6.5f shows the phase of the central line calculated by the PST method. Figure 6.5g shows the slope of the central line calculated by using the nonlinear model. Figure 6.5h shows the profile of the central line calculated by integration of the slope. Table 6.5 shows the error summary of profile measurement of the central line for the artifact with flat surface

Figure 6.6a shows the measured contour of the surface waviness on the calibrated artifact with 0.016mm peak-to-peak amplitude displayed in 3D mesh. Figure 6.6b shows the measured contour of the surface waviness on the calibrated artifact with 0.008mm peak-to-peak amplitude displayed in 3D mesh.

Figure 6.7a shows the measured contour of the surface waviness on the calibrated artifact with 0.016mm peak-to-peak amplitude displayed in grey-level image. Figure 6.7b shows the measured contour of the surface waviness on the calibrated artifact with 0.008mm peak-to-peak amplitude displayed in grey-level image.

Figure 6.8a shows the Dsight® image of the surface waviness on the calibrated artifact with 0.016mm peak-to-peak amplitude(improved by an histogram equalization algorithm). Figure 6.8b shows the Dsight® image of the surface waviness on the calibrated artifact with 0.008mm peak-to-peak amplitude(improved by an histogram equalization algorithm).

## 6.6 Conclusion

The experiments show that the contour and amplitude of the surface waves on the standard artifacts can be recovered successfully, using nonlinear PST retroreflective grating technology.

The precision and accuracy of the measurement are summarized in Table 6.6.

Possible errors of the measurement:

The largest error occurs in the artifacts themselves which is guaranteed to less than 1 micron, using a $CO_2$ laser in an interferometer to quantify the artifacts. This can not be easily improved. Furthermore this $\pm 1\mu m$ error could occur anywhere on the artifact in which we have $16 \pm 1\mu m$ peak-to-peak amplitude.

Other sources of experimental error, in their order of significance are: lens resolving power, nonlinear lens, imager contrast variation, measurement of grating pitch p, the phase shift of the grating, measurement of the distance L, optical modeling and others. However, it is estimated that none of these result in an error as large as the ±1μm error in the artifact itself, as this artifact error could be as large as 6.3% for the16μm artifact and 12.5% for the 8μm artifact.

For the "flat" artifact, the standard deviation is 0.30μm as shown in table 6.5 and it is assumed here that this is representative of the total experimental error.

For the error measurement see the Appendix C.

For the sensitivity, resolution, range and minimum suitable pitch of the measurement see the next chapter.

| | *Wavelength* | *Amplitude* |
|---|---|---|
| Surface Roughness | 0 to 0.5mm | <1μm |
| Surface Texture | 0.5 to 6mm | <1μm |
| Short Waviness | 6 to 25mm | <10μm |
| Long Waviness | 25 to 200mm | <25μm |
| Surface Shape | >200mm | >25μm |

Table 6.1 The dimensional aspects of surface quality

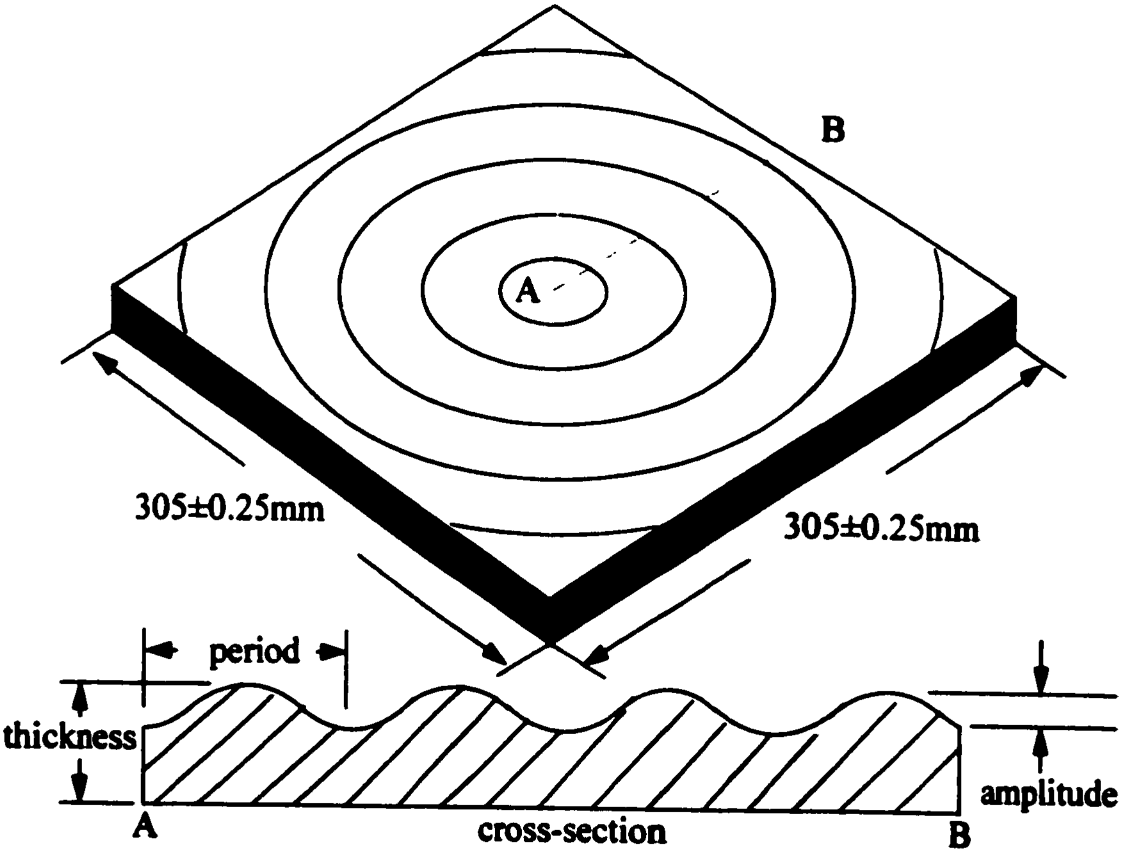

Figure 6.1 A schematic of the standard artifacts

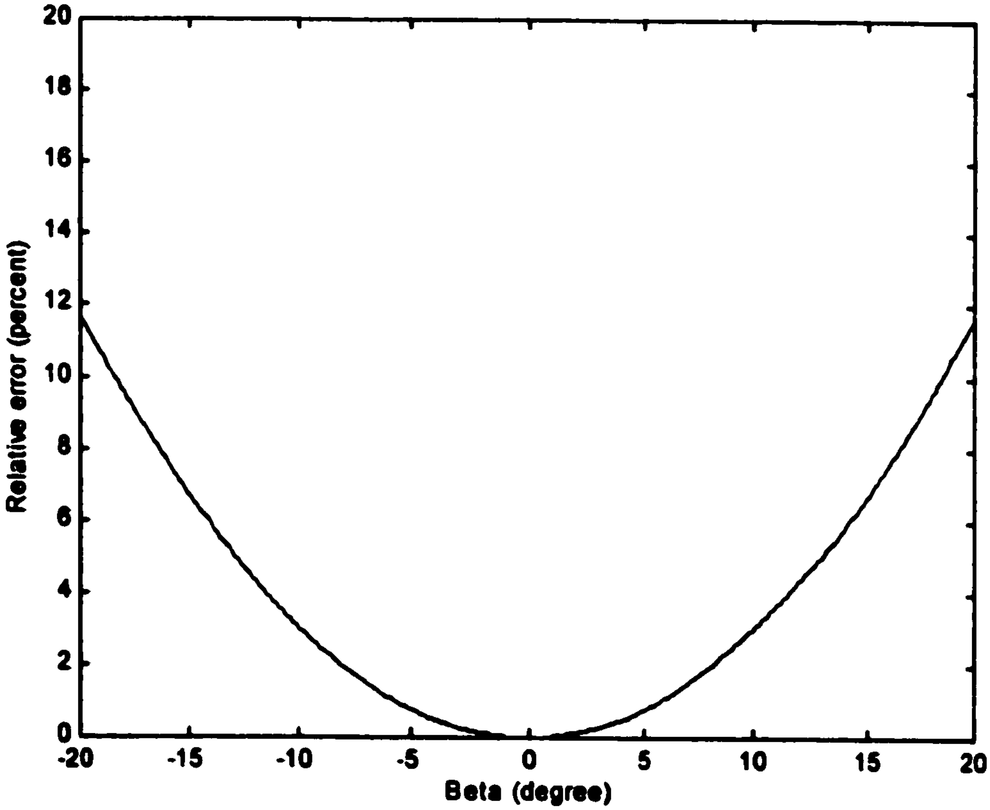

Figure 6.2 The relative error between the linear and nonlinear models

| $\beta$ | Relative error |
|---|---|
| <1° | <0.035% |
| <2° | <0.120% |
| <5° | <0.760% |
| <10° | <3.02% |
| <15° | <6.70% |
| <20° | <11.7% |

Table 6.2 The relative error between the linear and nonlinear models

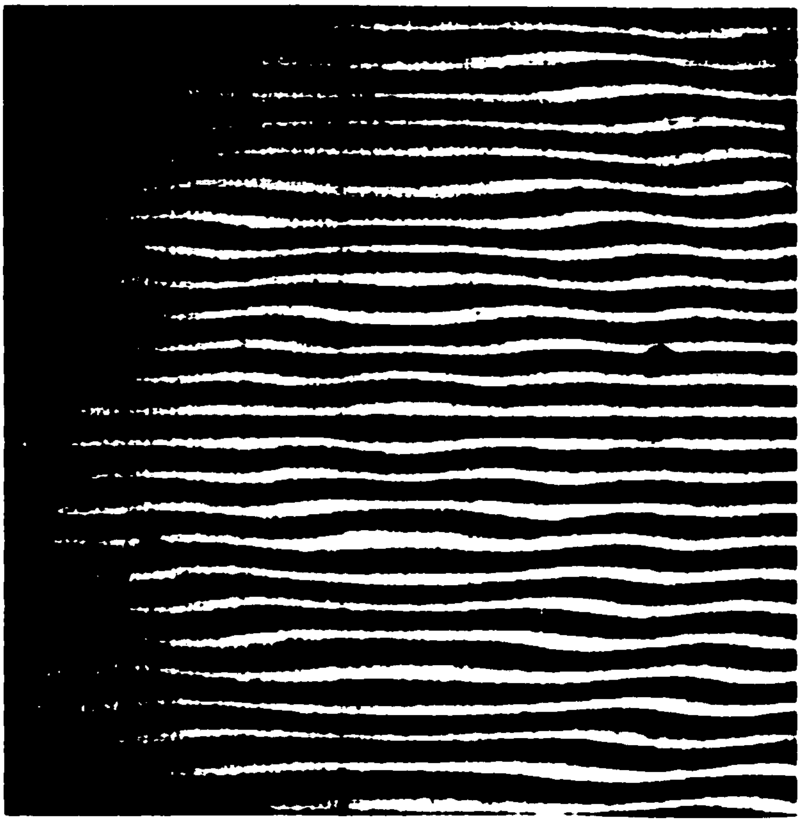

Figure 6.3a The grating image with phase shift $\alpha=0$ for the artifact with 0.016mm wave amplitude

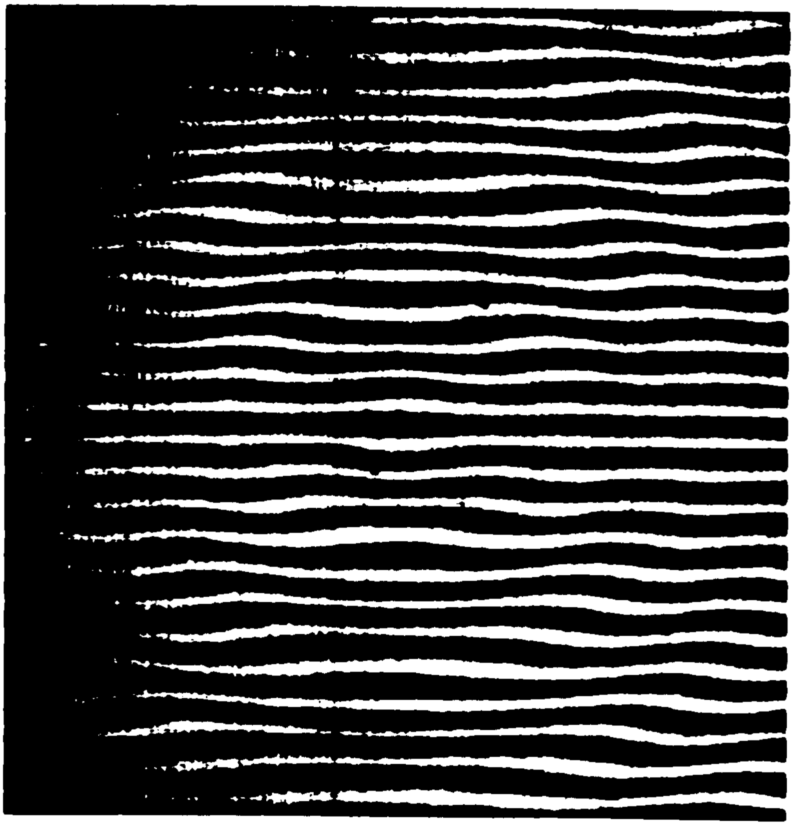

Figure 6.3b The grating image with phase shift $\alpha=\pi/2$ for the artifact

with 0.016mm wave amplitude

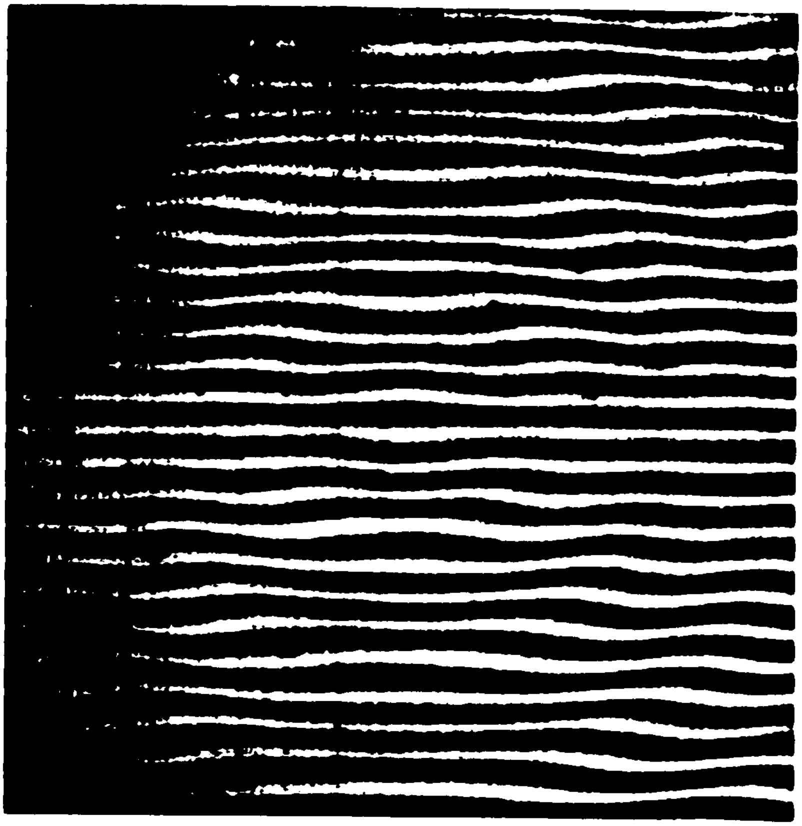

Figure 6.3c The grating image with phase shift $\alpha=\pi$ for the artifact with 0.016mm wave amplitude

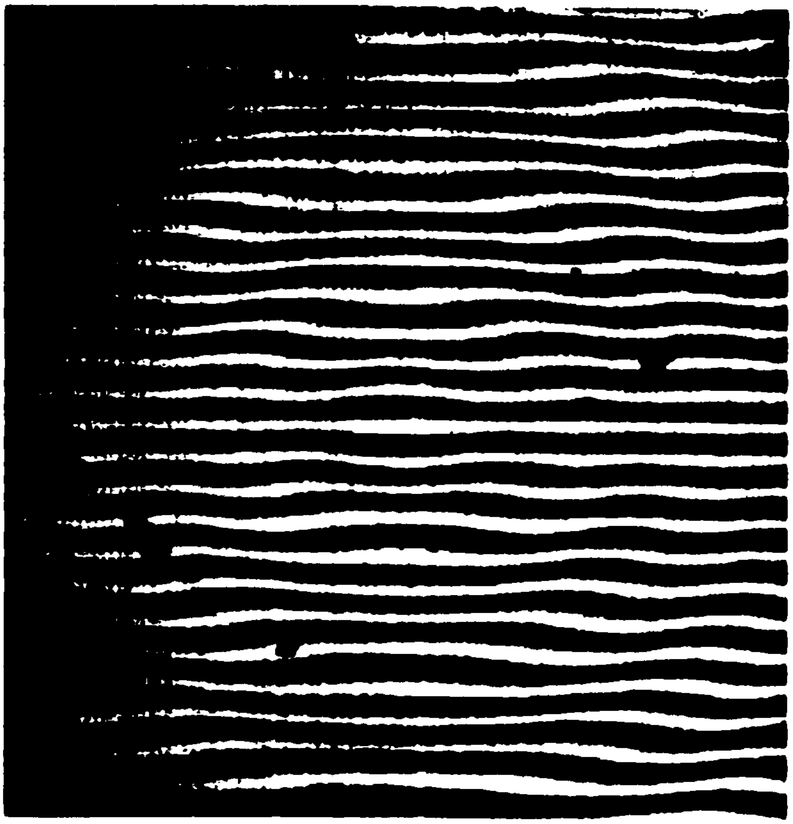

Figure 6.3d The grating image with phase shift α=3π/2 for the artifact

with 0.016mm wave amplitude

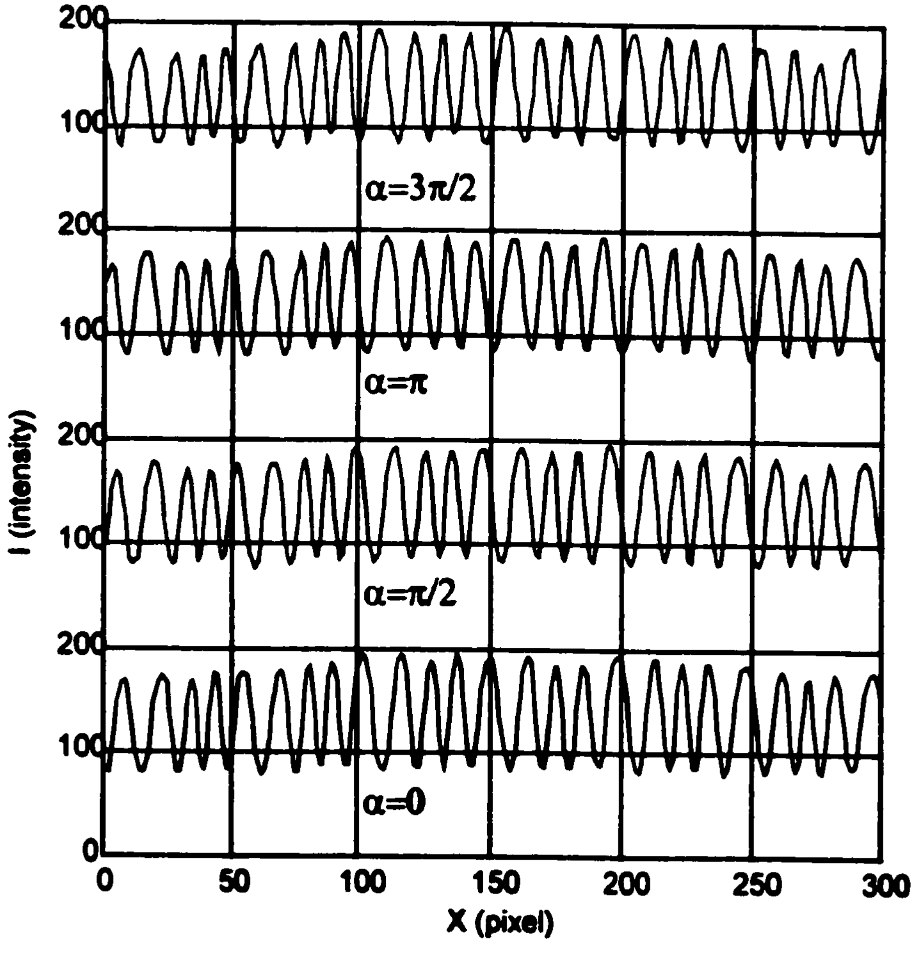

Figure 6.3e The intensity of central slices of the four grating images for the artifact with 0.016mm wave amplitude

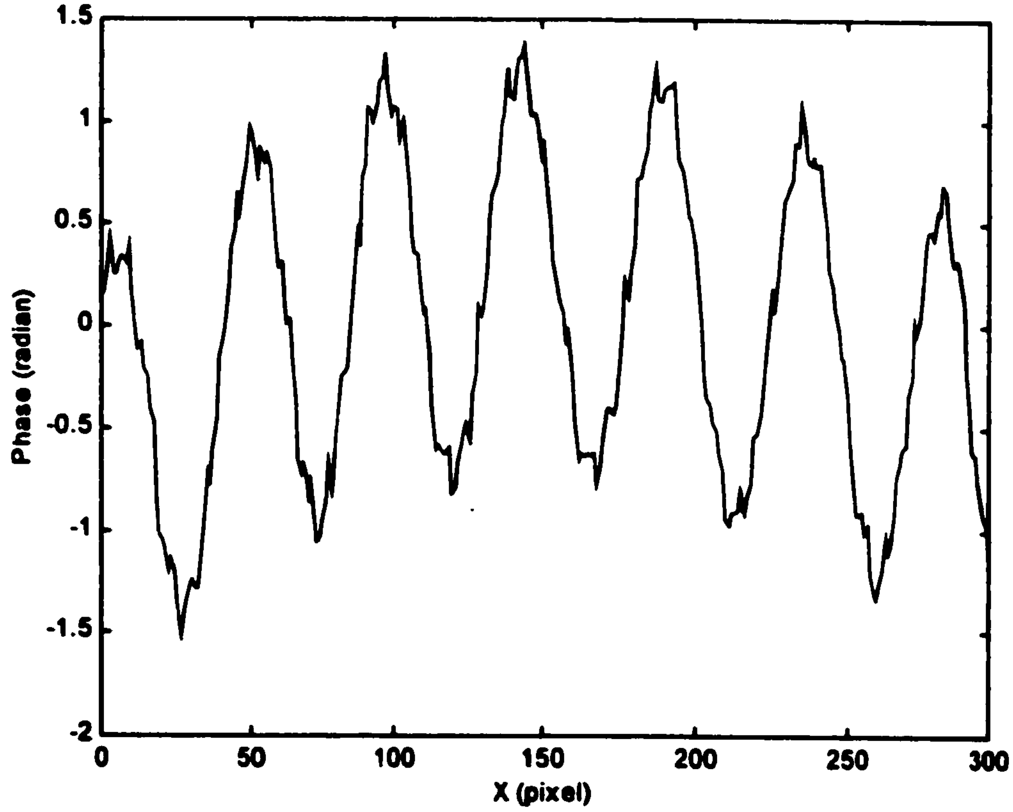

Figure 6.3f The phase of the central line calculated by the PST method

for the artifact with 0.016mm wave amplitude

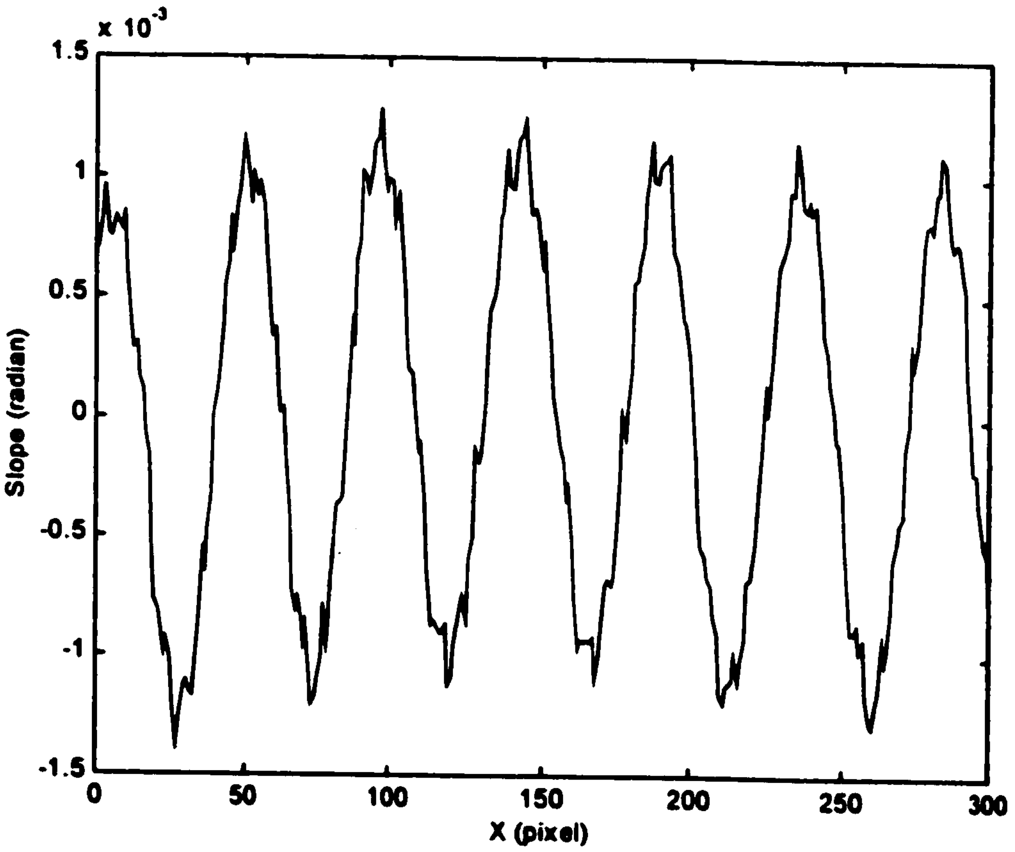

Figure 6.3g The slope of the central line calculated by using the nonlinear model for the artifact with 0.016mm wave amplitude

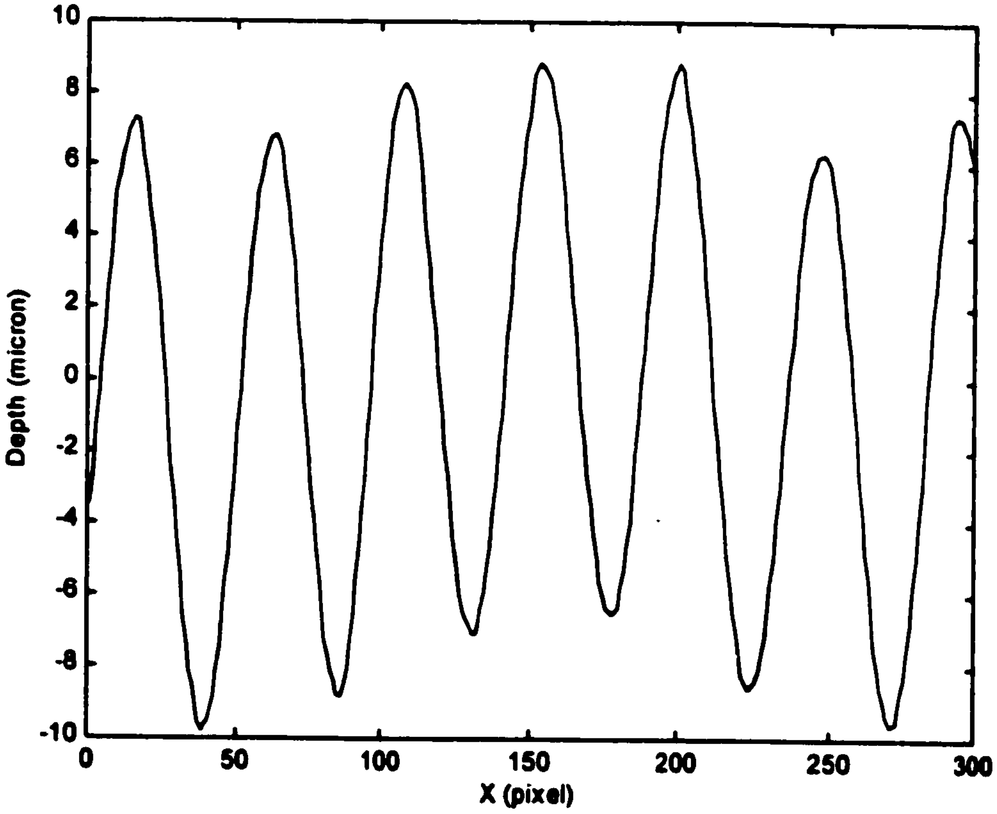

Figure 6.3h The profile of the central line calculated by integration of the slope for the artifact with 0.016mm wave amplitude

| Peak No. (n) | Location (pixel) | Peak Value (micron) | Adjacent peak-peak distance (pixel) | Peak-peak amplitude (micron) |
|---|---|---|---|---|
| 0 | 16 | +7.28 | ---- | ---- |
| 1 | 38 | -9.76 | 22 | 17.04 |
| 2 | 63 | +6.84 | 25 | 16.60 |
| 3 | 85 | -8.80 | 22 | 15.65 |
| 4 | 109 | +8.25 | 24 | 17.05 |
| 5 | 131 | -7.10 | 22 | 15.35 |
| 6 | 154 | +8.81 | 23 | 15.90 |
| 7 | 178 | -6.52 | 24 | 15.33 |
| 8 | 201 | +8.82 | 23 | 15.34 |
| 9 | 224 | -8.58 | 23 | 17.41 |
| 10 | 247 | +6.33 | 23 | 14.92 |
| 11 | 271 | -9.61 | 24 | 15.95 |
| 12 | 293 | +7.36 | 22 | 16.97 |

**Table 6.3a The peak-to-peak amplitudes on the profile of the central line for the artifact with 0.016mm wave amplitude**

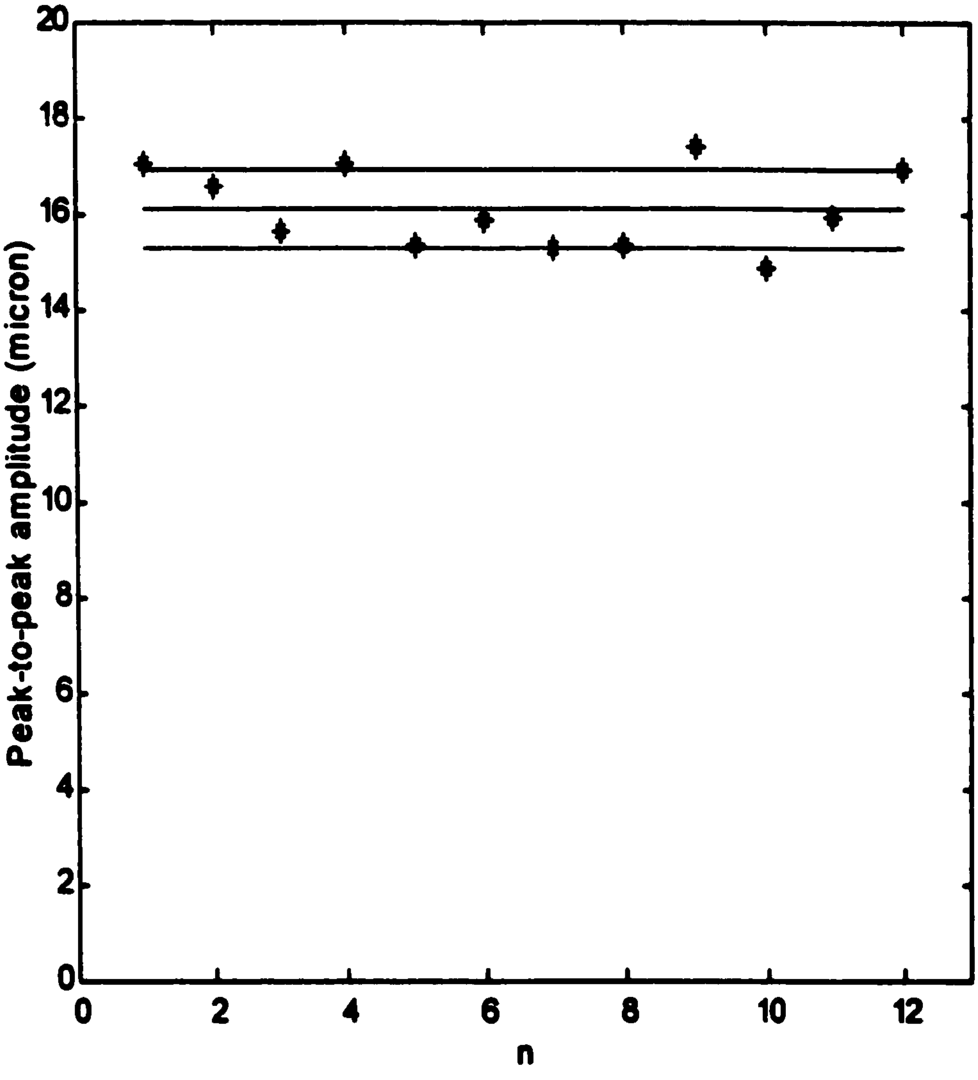

Figure 6.3i The error band of the peak-to-peak amplitudes on the central line for the artifact with 0.016mm wave amplitude (mean±σ=16.1±0.812)

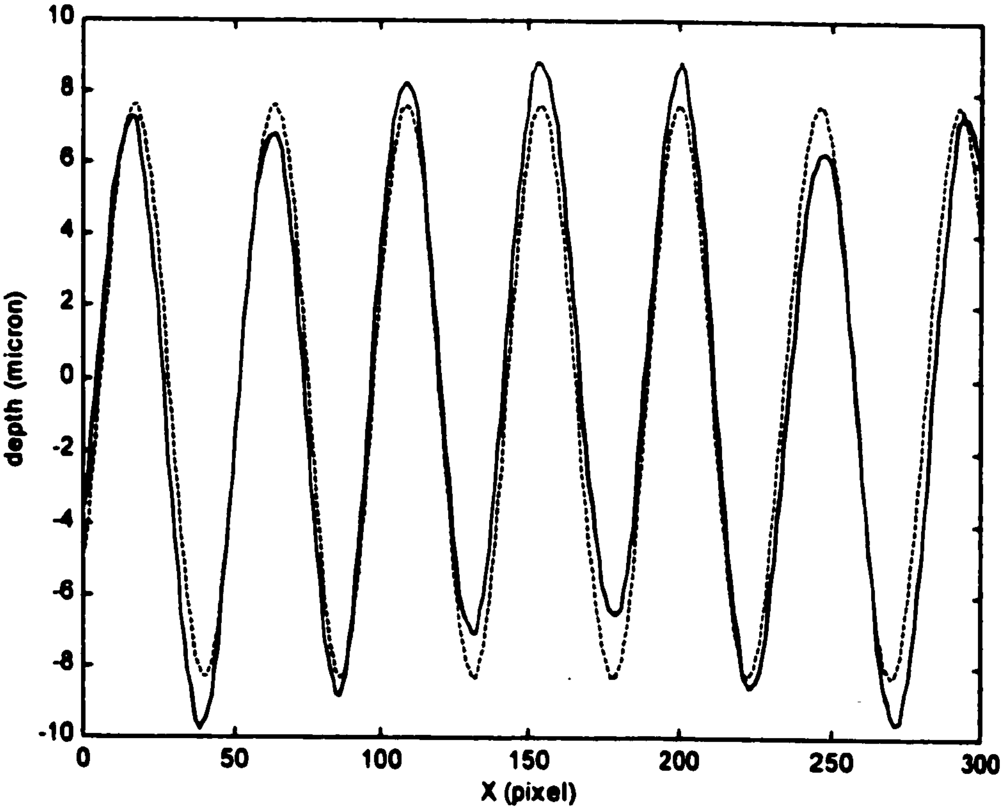

Figure 6.3j The peak-to-peak amplitude of the central line calculated by the least squares trigonometric approximation for the artifact with 0.016mm wave amplitude

Note: C0=-0.3306, C1=7.9668, γ=-131.38°

(the solid line is the experimental data and the dashed line represents the least squares trigonometric approximation of the experimental data)

| Peak-to-peak amplitude | Value (micron) | Relative error |
|---|---|---|
| Mean | 16.1 | +0.625% |
| Standard deviation | ±0.812 | |
| Maximum | 17.4 | +8.75% |
| Minimum | 14.9 | -6.88% |
| Curve-fit(mean) | 15.9 | -0.625% |

Table 6.3b The error summary of peak-to-peak amplitude measurement compared to the calibrated artifacts with 0.016±0.001mm peak-to-peak amplitude

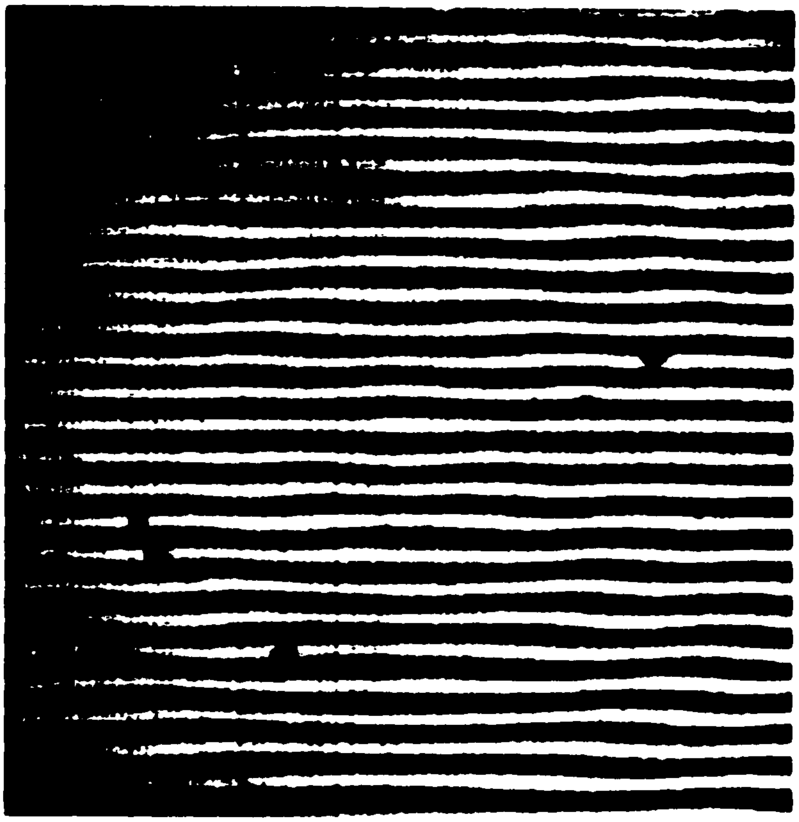

Figure 6.4a The grating image with phase shift α=0 for the artifact with 0.008mm wave amplitude

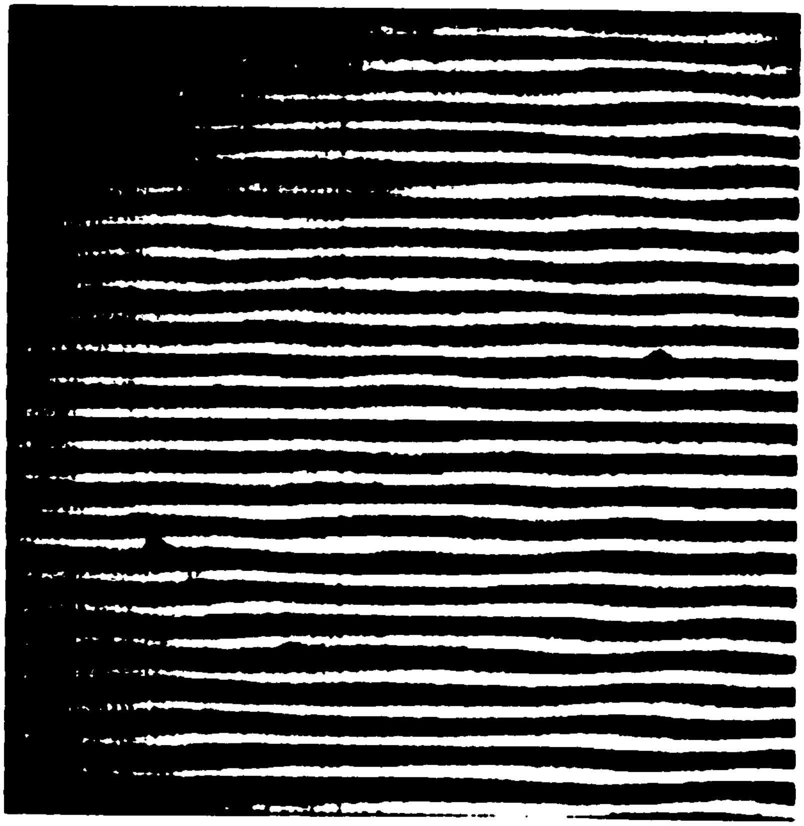

Figure 6.4b The grating image with phase shift $\alpha=\pi/2$ for the artifact with 0.008mm wave amplitude

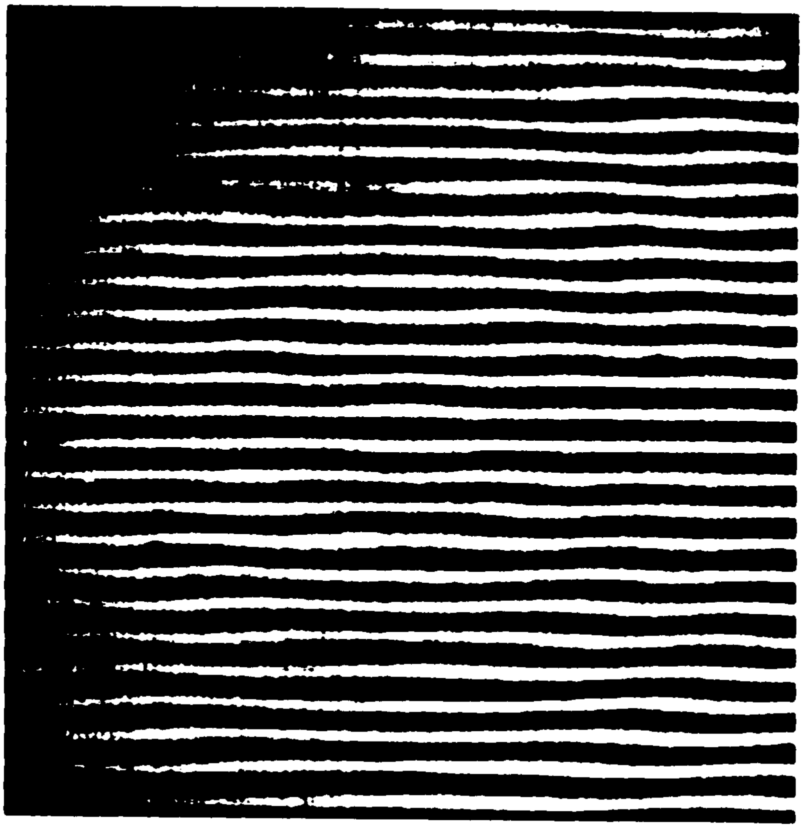

Figure 6.4c The grating image with phase shift $\alpha=\pi$ for the artifact with 0.008mm wave amplitude

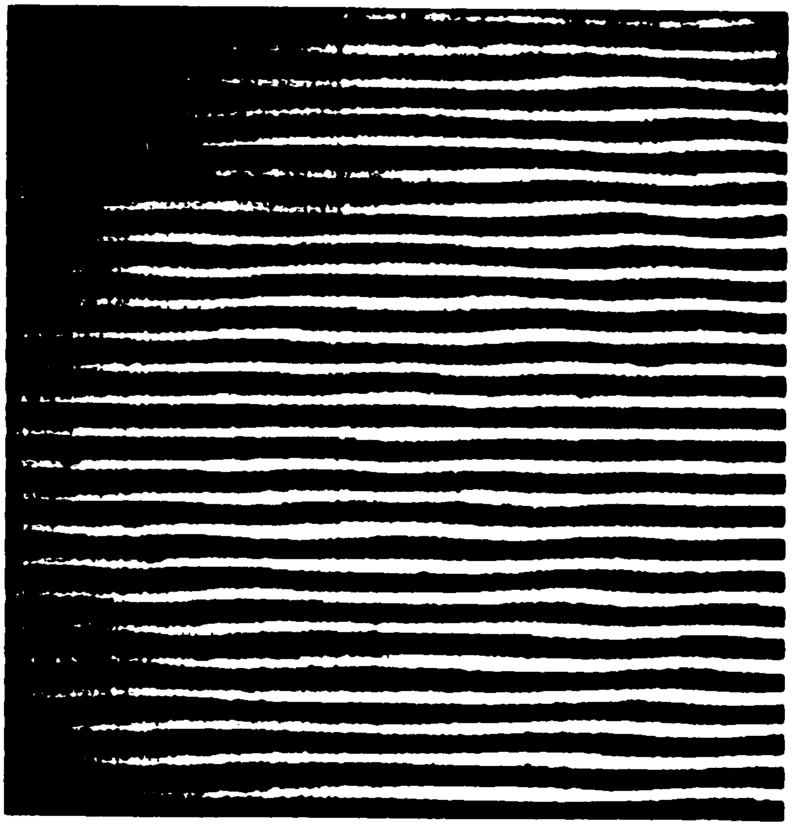

Figure 6.4d The grating image with phase shift $\alpha=3\pi/2$ for the artifact

with 0.008mm wave amplitude

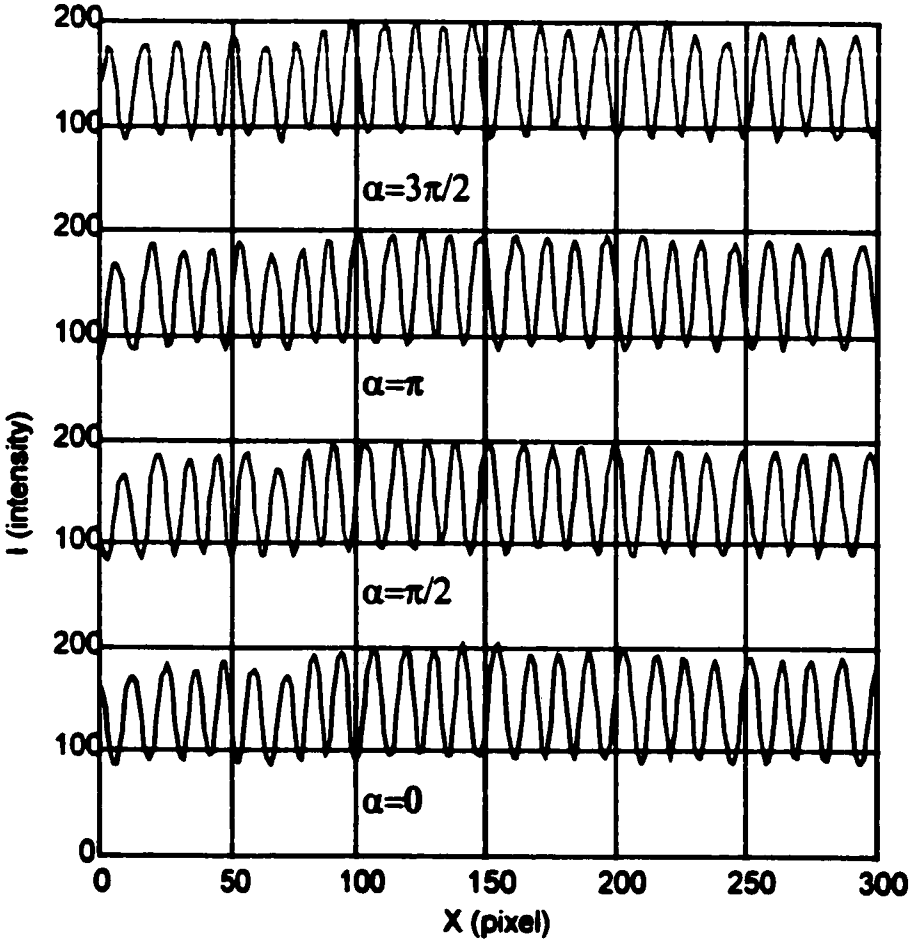

Figure 6.4e The intensity of central slices of the four grating images for the artifact with 0.008mm wave amplitude

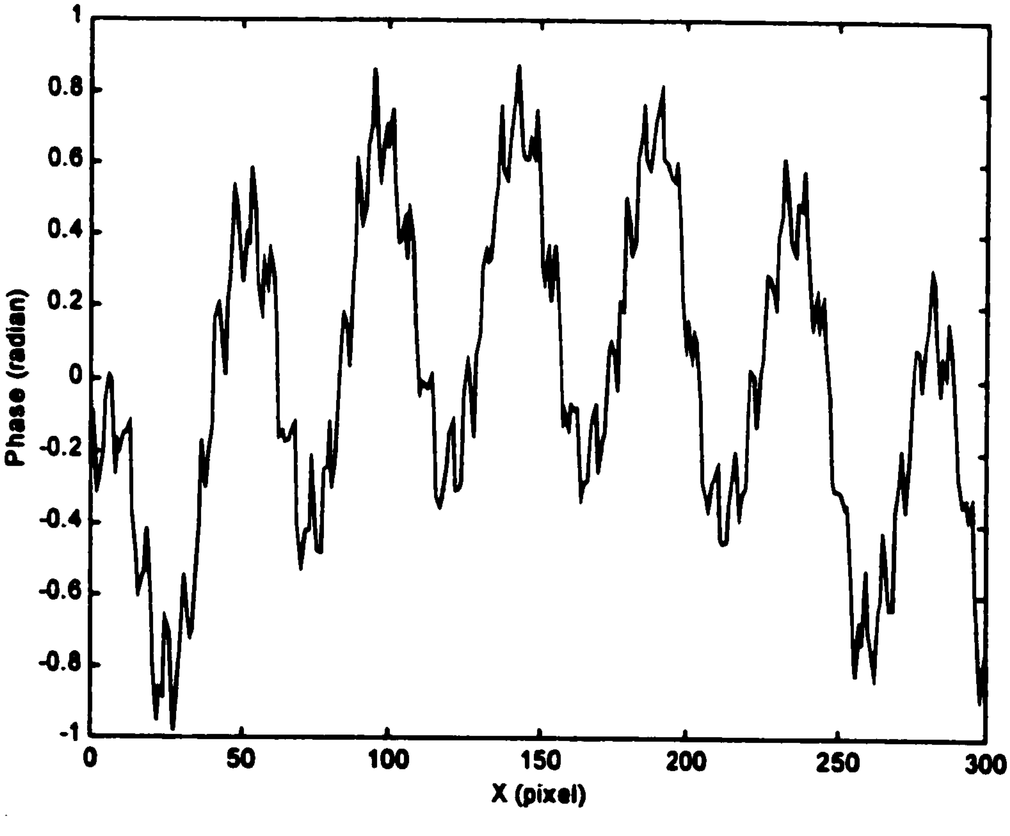

Figure 6.4f The phase of the central line calculated by the PST method for the artifact with 0.008mm wave amplitude

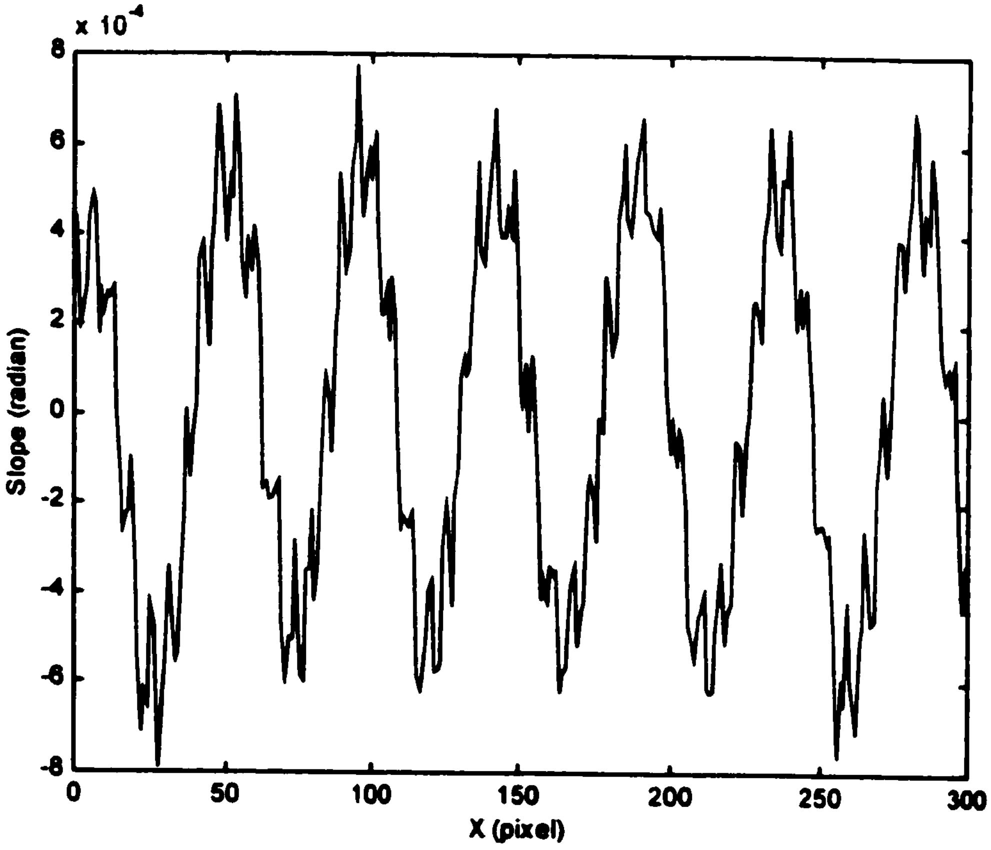

Figure 6.4g The slope of the central line calculated by using the nonlinear model for the artifact with 0.008mm wave amplitude

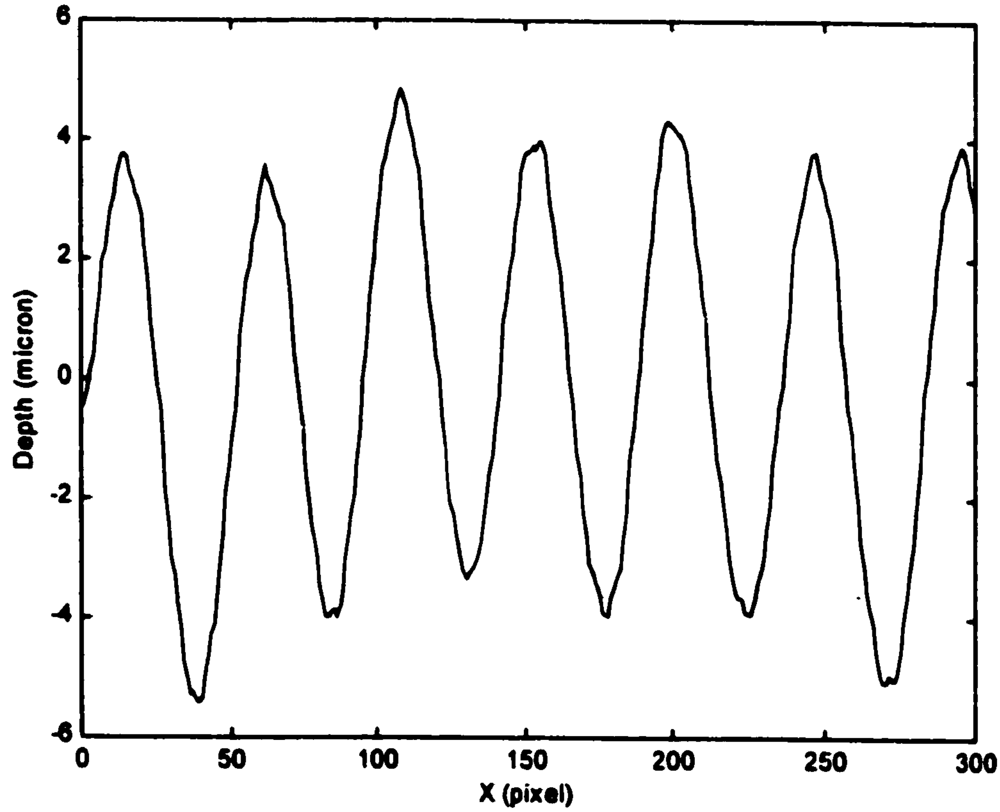

Figure 6.4h The profile of the central line calculated by integration of the slope for the artifact with 0.008mm wave amplitude

| Peak No. (n) | Location (pixel) | Peak Value (micron) | Adjacent peak-to-peak distance (pixel) | Peak-to-peak amplitude (micron) |
|---|---|---|---|---|
| 0 | 14 | +3.76 | ---- | ---- |
| 1 | 39 | -5.39 | 25 | 9.15 |
| 2 | 61 | +3.54 | 22 | 8.93 |
| 3 | 82 | -3.97 | 21 | 7.51 |
| 4 | 108 | +4.82 | 26 | 8.79 |
| 5 | 130 | -3.33 | 22 | 8.15 |
| 6 | 156 | +3.96 | 26 | 7.29 |
| 7 | 178 | -3.96 | 22 | 7.93 |
| 8 | 199 | +4.32 | 21 | 8.29 |
| 9 | 225 | -3.94 | 26 | 8.26 |
| 10 | 247 | +3.79 | 22 | 7.73 |
| 11 | 270 | -5.04 | 23 | 8.83 |
| 12 | 295 | +3.91 | 25 | 8.95 |

**Table 6.4a The peak-to-peak amplitudes on the profile of the central line for the artifact with 0.008mm wave amplitude**

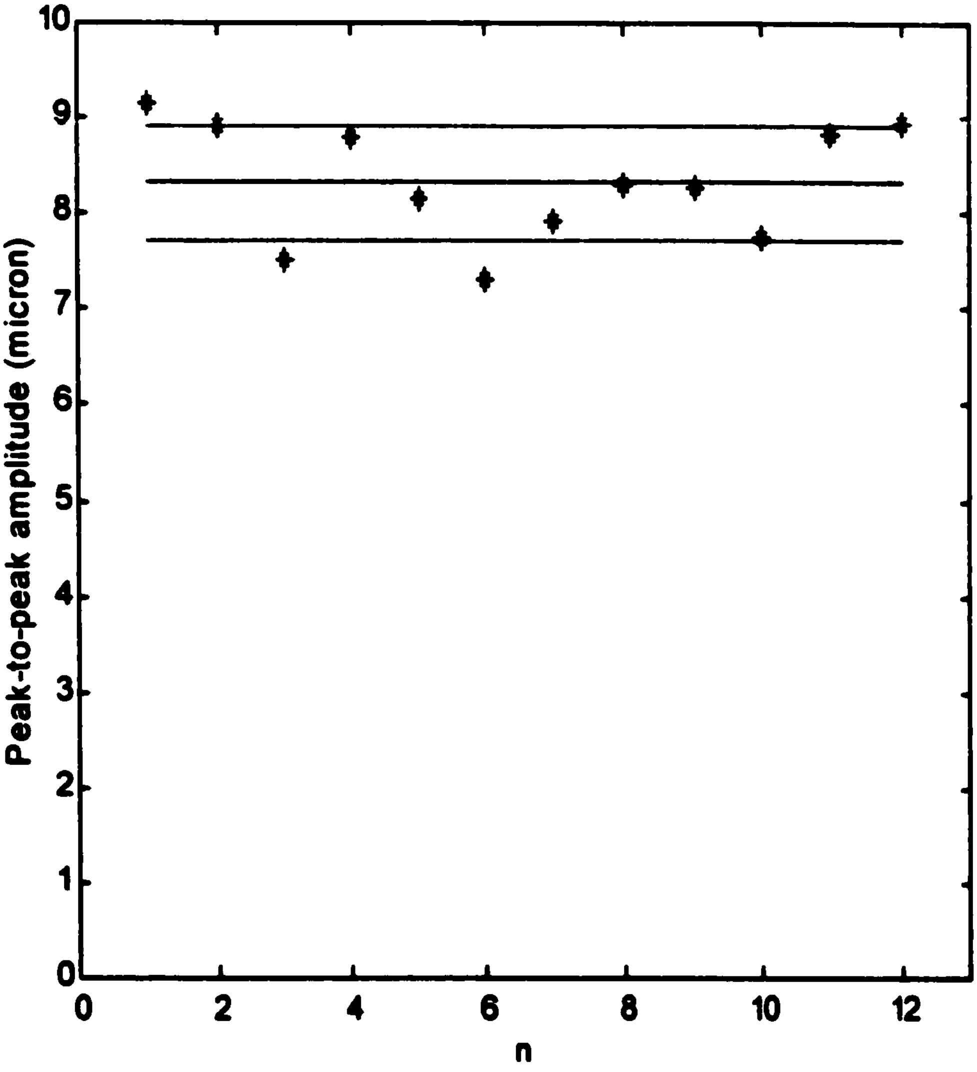

Figure 6.4i The error band of the peak-to-peak amplitudes on the central line

for the artifact with 0.008mm wave amplitude

(mean±σ=8.32±0.591microns)

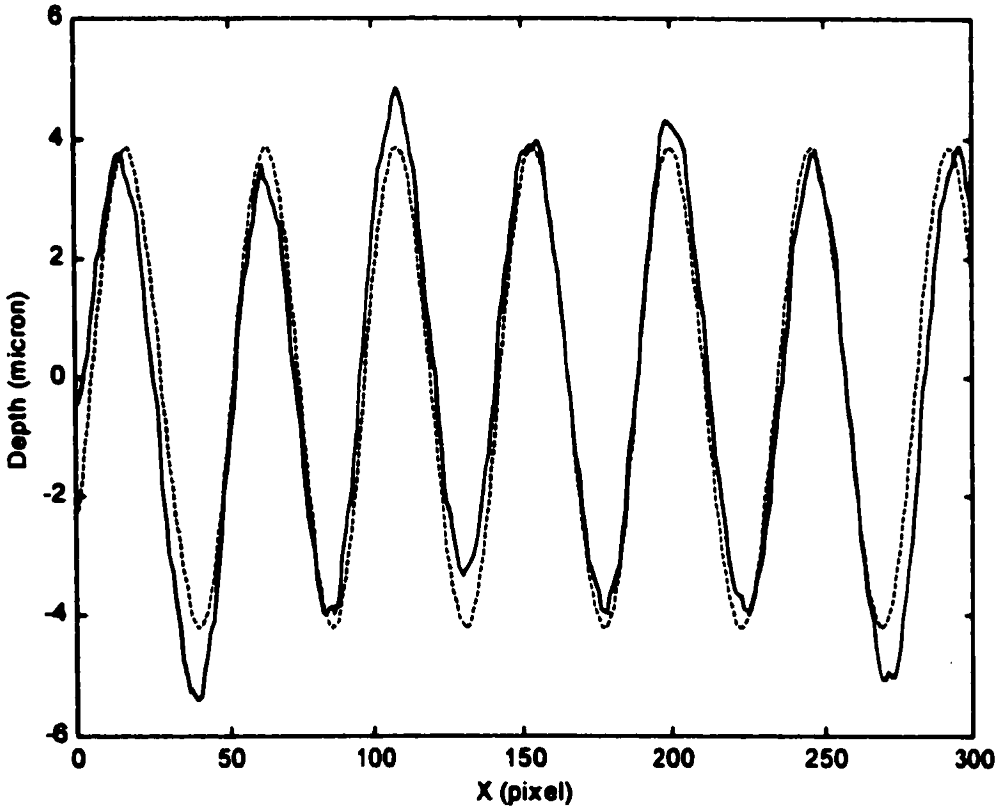

Figure 6.4j The peak-to-peak amplitude of the central line calculated by the least squares trigonometric approximation for the artifact with 0.008mm wave amplitude

Note: C0=-0.1721, C1=4.0288, $\gamma$=-128.46°

(the solid line is the experimental data and the dashed line represents the least squares trigonometric approximation of the experimental data)

| Peak-to-peak amplitude | Value (micron) | Relative error |
|---|---|---|
| Mean | 8.32 | +4.0% |
| Standard deviation | ±0.591 | |
| Maximum | 9.15 | +14.4% |
| Minimum | 7.29 | -8.88% |
| Curve-fit | 8.06 | +0.75% |

Table 6.4b The error summary of peak-to-peak amplitude measurement compared to the calibrated artifact with 0.008±0.001mm peak-to-peak amplitude

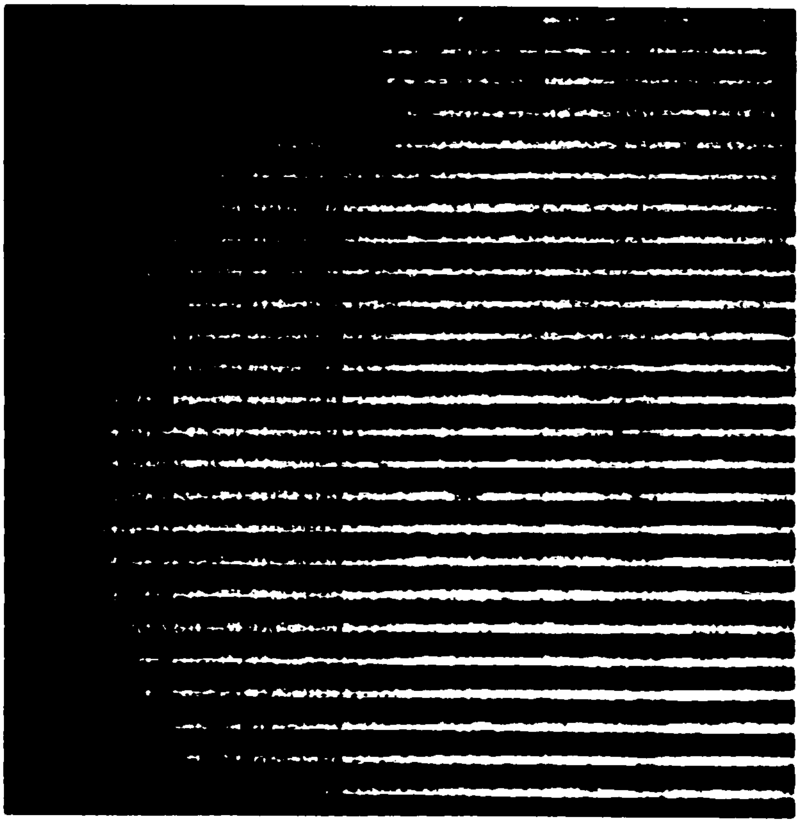

Figure 6.5a The grating image with phase shift $\alpha=0$ for the artifact with flat surface

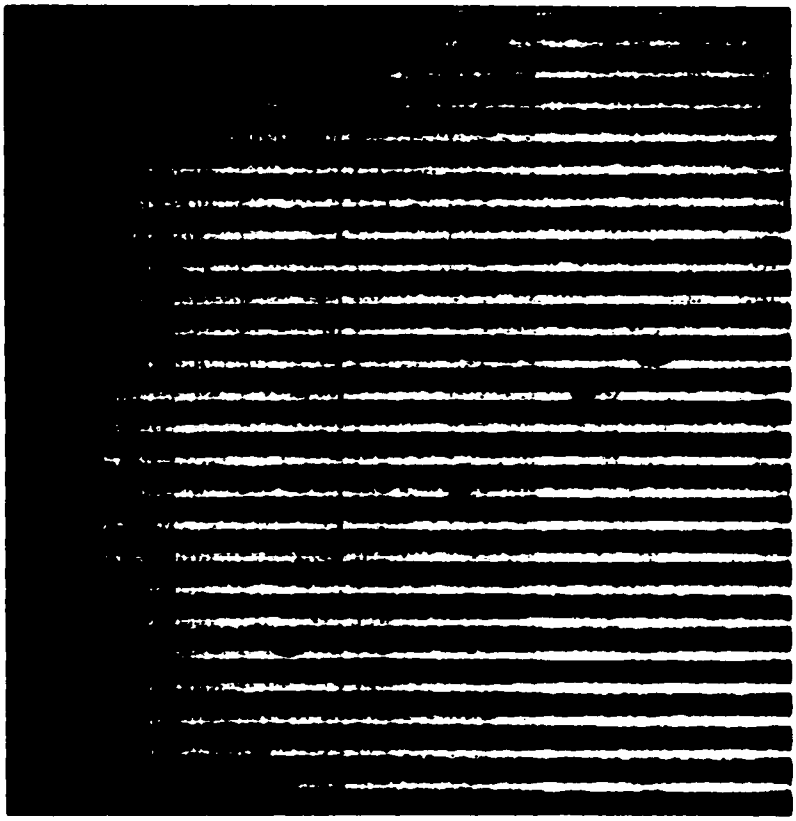

Figure 6.5b The grating image with phase shift $\alpha=\pi/2$ for the artifact with flat surface

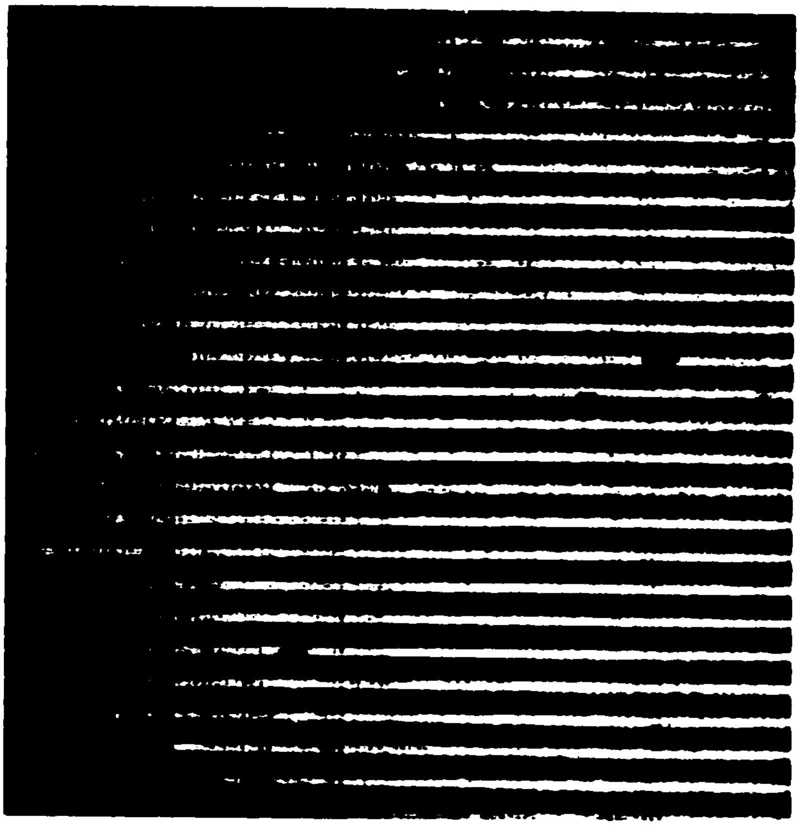

Figure 6.5c The grating image with phase shift $\alpha=\pi$ for the artifact with flat surface

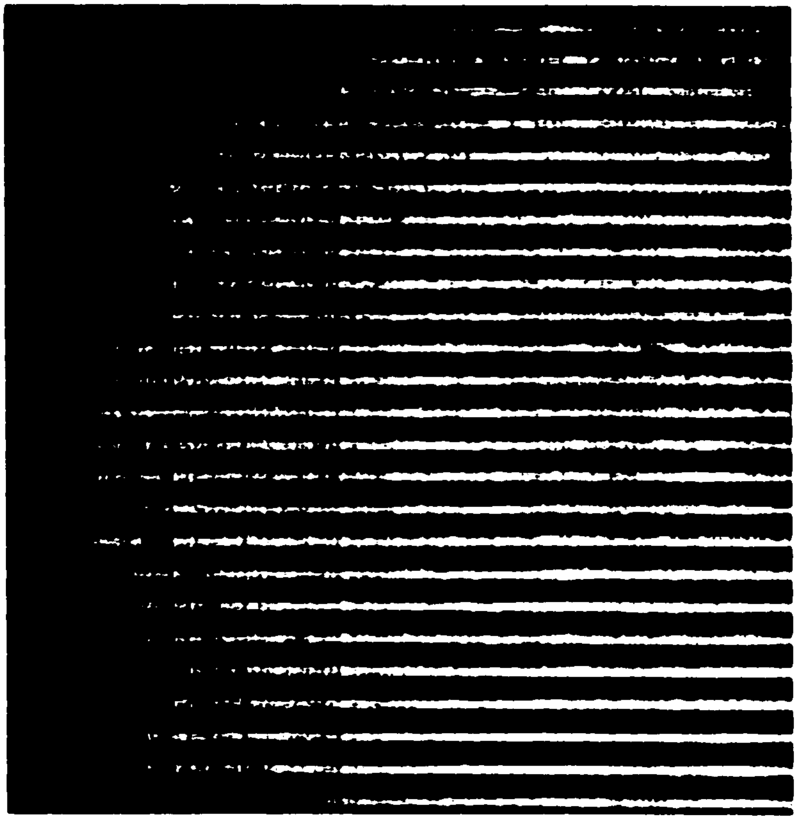

Figure 6.5d The grating image with phase shift $\alpha=3\pi/2$ for the artifact with flat surface

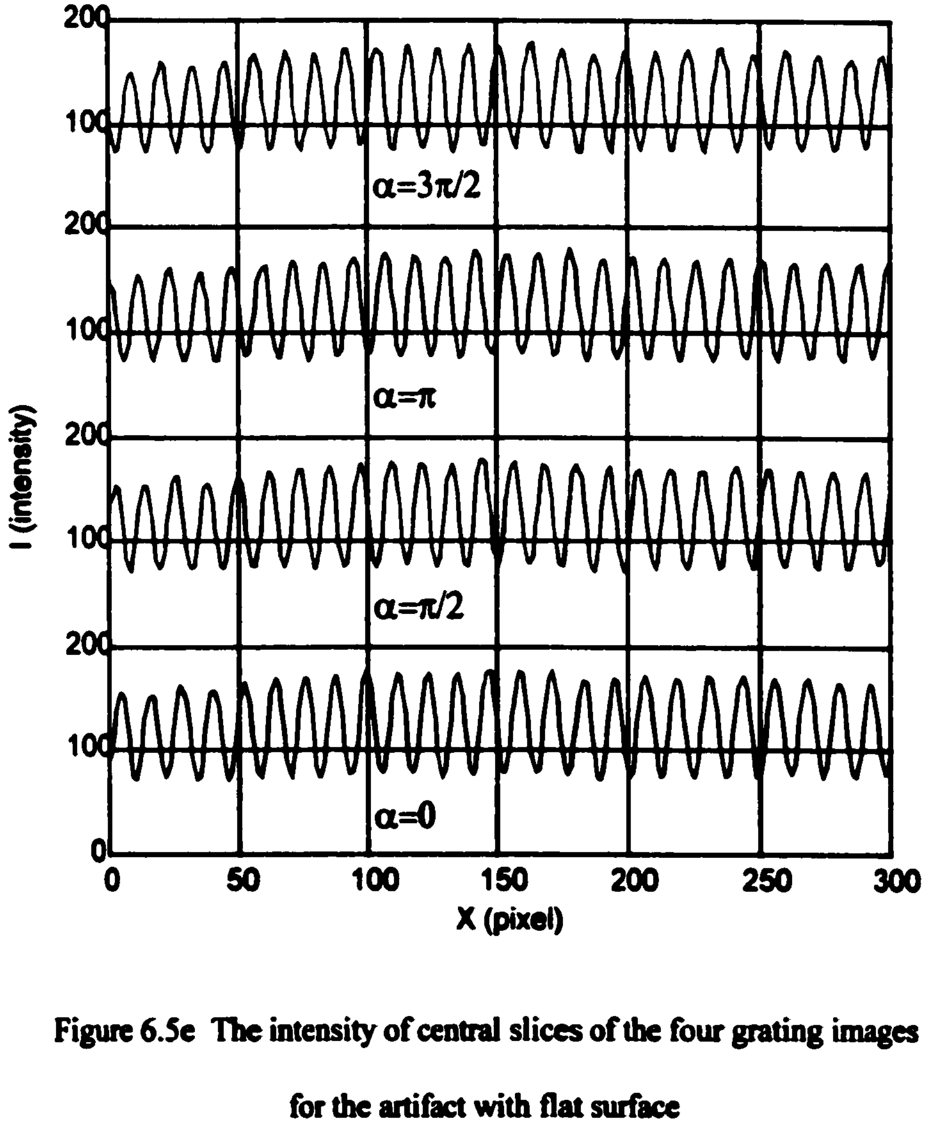

Figure 6.5e The intensity of central slices of the four grating images for the artifact with flat surface

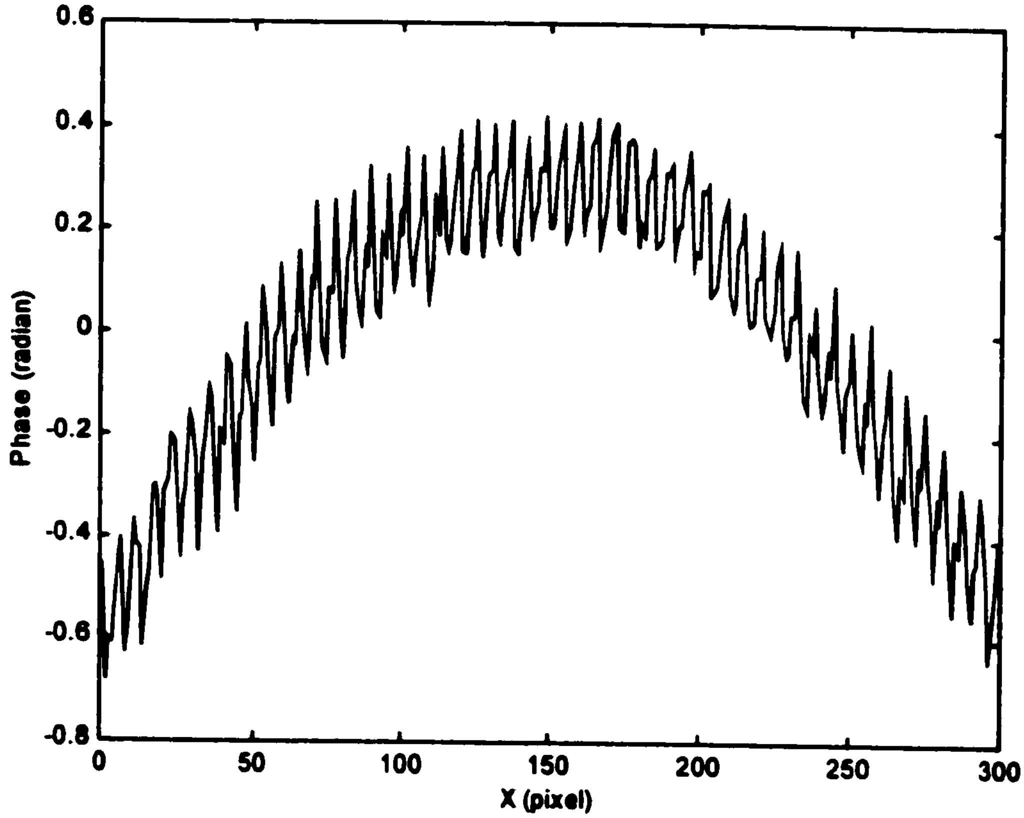

Figure 6.5f The phase of the central line calculated by the PST method

for the artifact with flat surface

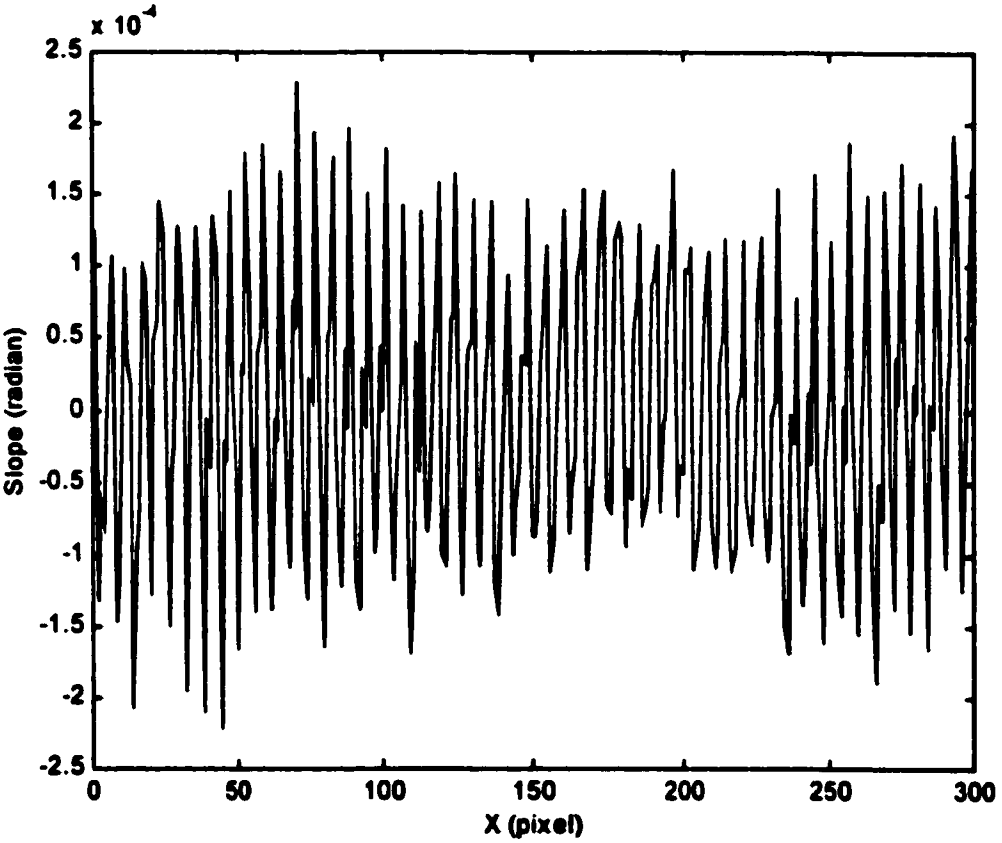

Figure 6.5g The slope of the central line calculated by using the nonlinear model for the artifact with flat surface

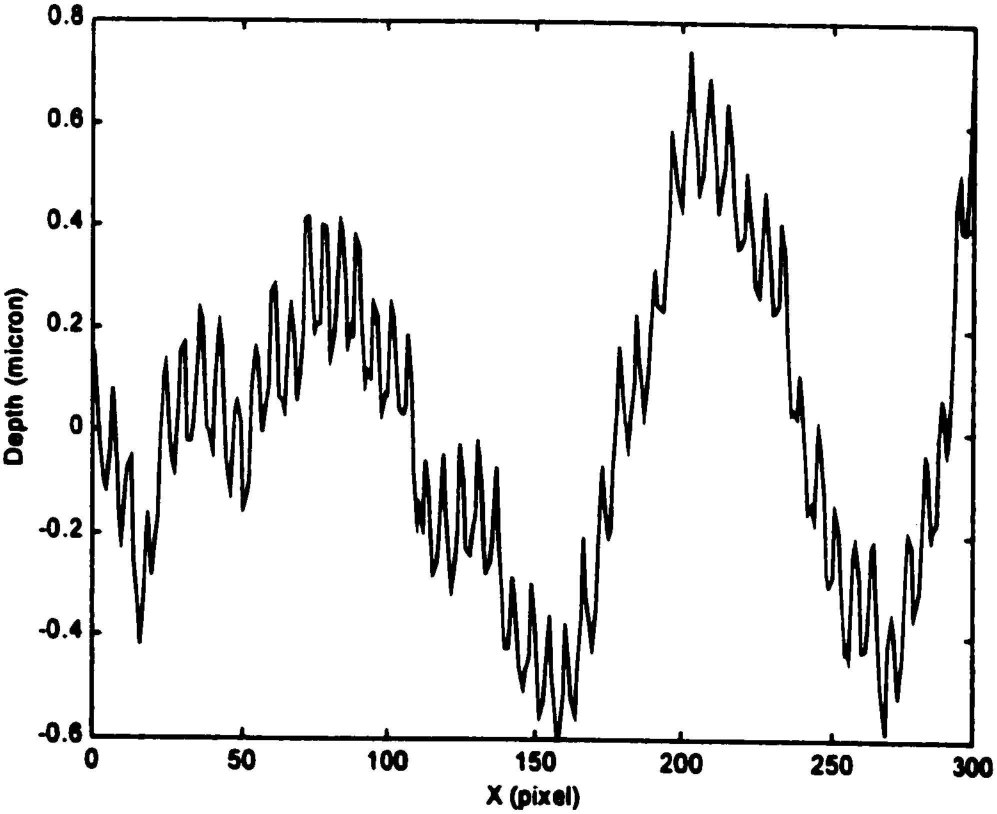

**Figure 6.5h** The profile of the central line calculated by integration of the slope for the artifact with flat surface

| Depth | Value (micron) |
|---|---|
| Mean | 0 |
| Standard deviation | ±0.305 |
| Maximum | +0.770 |
| Minimum | -0.599 |

Table 6.5 The error summary of profile measurement for the central line of the calibrated artifact which is guaranteed flat ±1µm

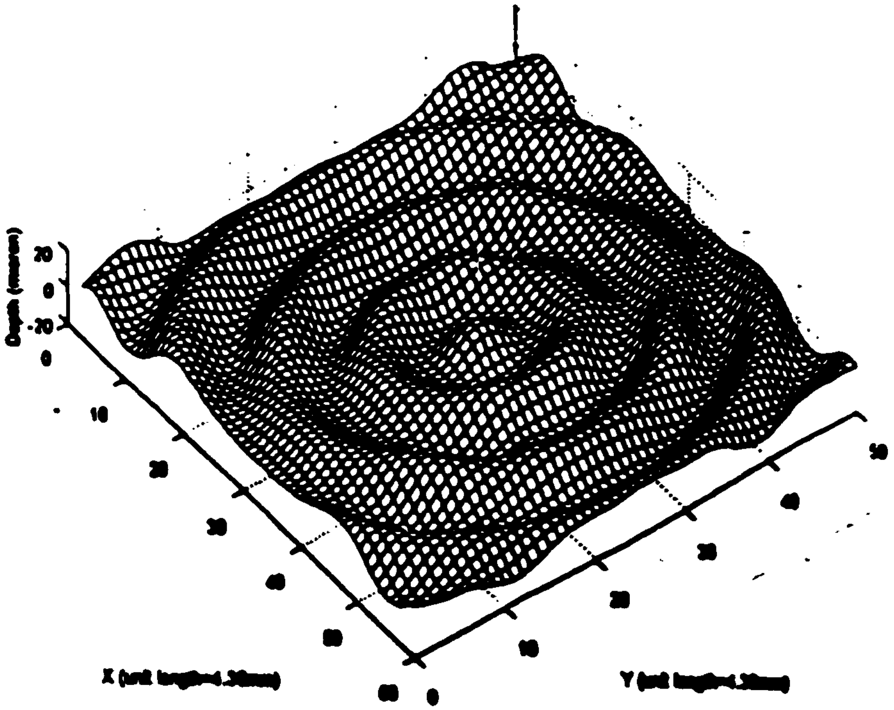

Figure 6.6a The measured contour of the surface waviness on the calibrated artifact with 0.016mm peak-to-peak amplitude displayed in 3D mesh

Note: field of view(262mm, 218mm)

Matlab view(-37.5+90,80)

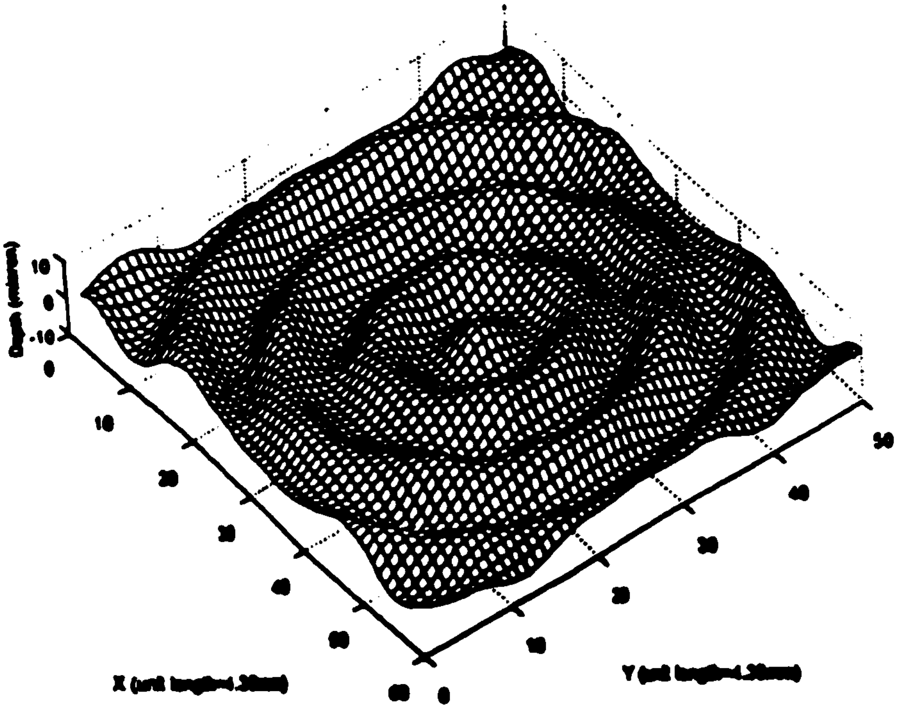

Figure 6.6b The measured contour of the surface waviness on the calibrated artifact

with 0.008mm peak-to-peak amplitude displayed in 3D mesh

Note: field of view(262mm, 218mm)

Matlab view(-37.5+90,80)

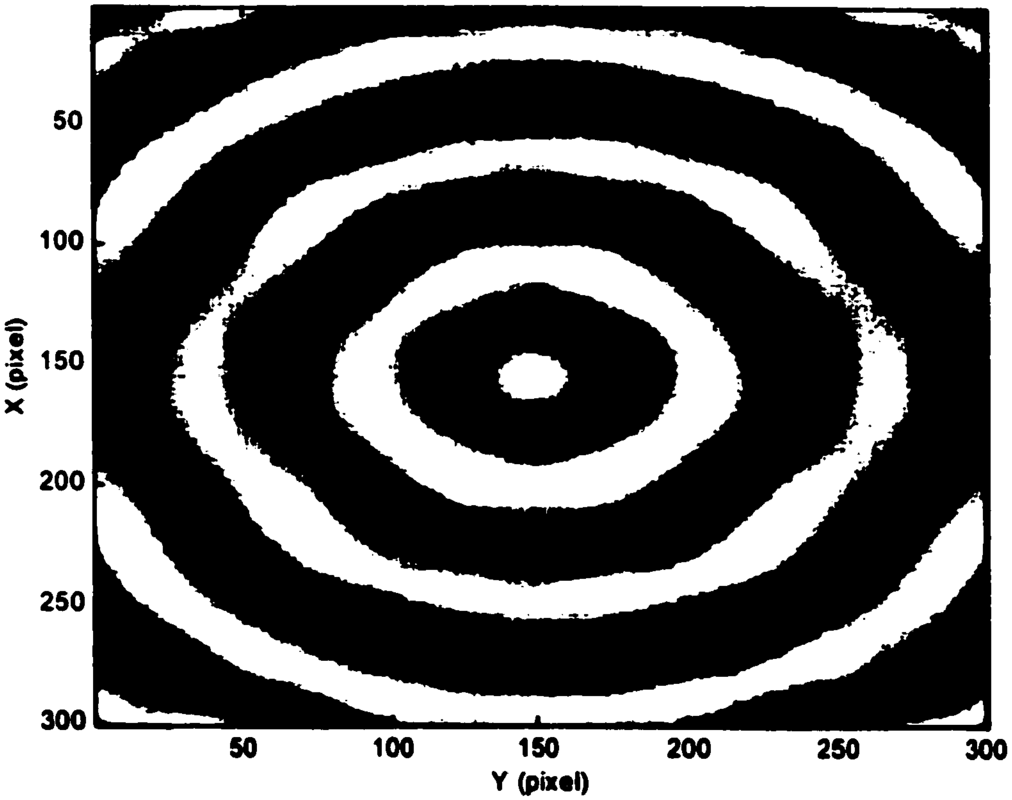

Figure 6.7a The measured contour of the surface waviness on the calibrated artifact with 0.016mm peak-to-peak amplitude displayed in grey-level image

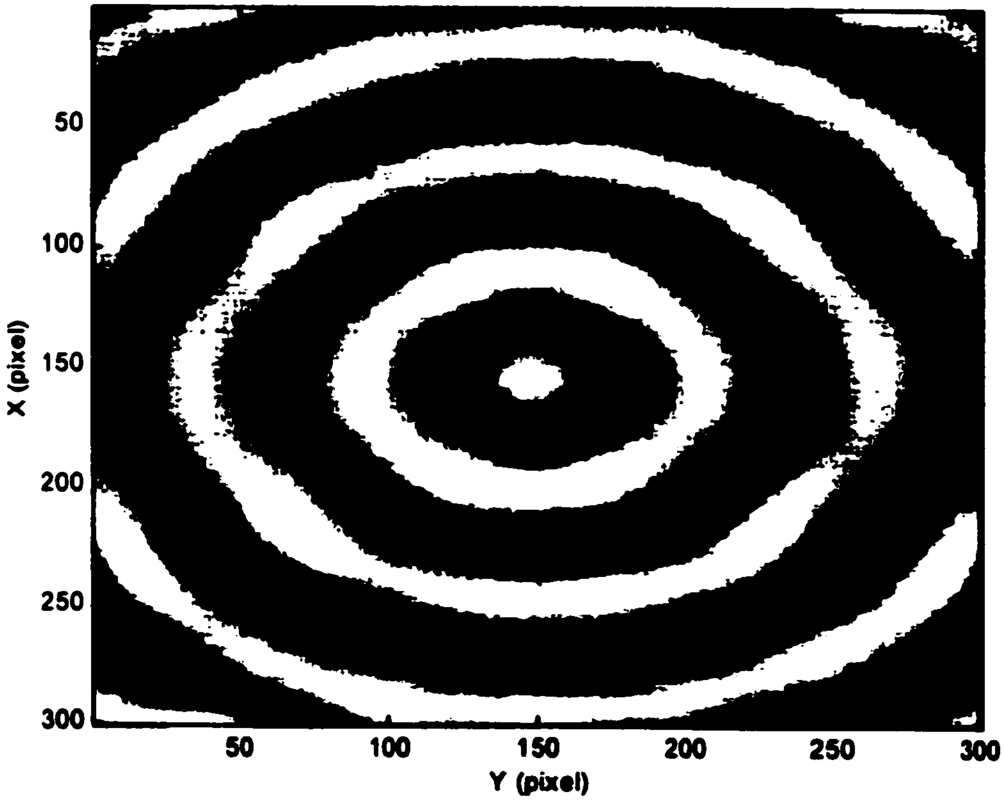

Figure 6.7b The measured contour of the surface waviness on the calibrated artifact with 0.008mm peak-to-peak amplitude displayed in grey-level image

Figure 6.8a The Dsight® image of the surface waviness on the calibrated artifact

with 0.016mm peak-to-peak amplitude

(improved by an histogram equalization algorithm).

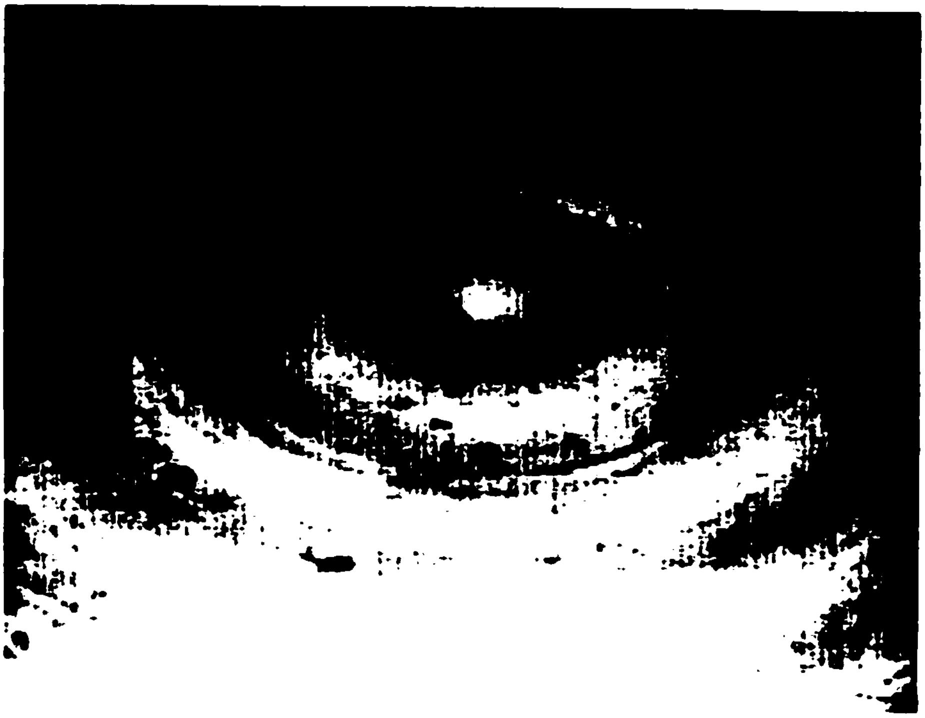

Figure 6.8b The Dsight® image of the surface waviness on the calibrated artifact with 0.008mm peak-to-peak amplitude (improved by an histogram equalization algorithm).

| Item | True value | Predicted value | Precision | Accuracy |
|---|---|---|---|---|
| Flat Surface | 0 | 0 | ±0.305μm | --- |
| Waviness I | 8.00μm | 8.32μm | ±0.591μm | 3.96% |
| Waviness II | 16.0μm | 16.1μm | ±0.812μm | 0.78% |

Table 6.6 The precision and accuracy of the measurement

# Chapter 7

# Discussions and Conclusions

## 7.1 The parameters for the optical configuration

The software package for image processing is Matrox Inspector 2.0 and the frame grabber is Matrox Meteor Rev .02 board. Both of them are products of Matrox Electronic Systems Ltd.

COHU CCD Camera (Model No.4812-2000/0000):

The CCD chip area is 8.8 by 6.6 mm in the y and x direction respectively.

Number of active picture elements is 754 (H or y direction) by 488 (v or x direction) on the camera and each pixel size is 11.5μm (H or y direction) by 13.5μm (V or x direction).

Field of view:

The dimension of the reference artifacts is 305mm by 305mm.

The Matrox field of view chosen for analysis is 262mm (300 pixels) by 218mm (300 pixels).

The unit lengths in x and y directions are 4.36mm (5 pixels) and 4.36mm (6 pixels), respectively, i.e., each frame grabber pixel in the x and y directions is equivalent to 0.871mm and 0.726mm on the object, respectively.

The demagnification of the optical configuration is shown in Figure 7.1 and calculated as follows:

$$Demagnification = \sqrt{\frac{0.8714mm \times 0.7262mm}{13.5\mu m \times 11.5\mu m}} = \sqrt{4076} = 64 \qquad (7.1)$$

## 7.2 Sensitivity

Sensitivity is the ratio of output signal over the input signal. In retroreflective metrology, the surface under test functions as a modulator (or sensor). The input signal is the local slope of the surface under test. The output signal is the phase change in the distorted grating image. The sensitivity is then calculated as follows:

$$sensitiviy = \frac{d\Phi}{d\theta} = 4\pi n \left( \frac{radians}{radians} \quad or \quad \frac{\deg rees\_of\_phase\_shift}{\deg rees\_of\_slope\_change} \right) \tag{7.2}$$

The sensitivity of the measurement depends on the amplification of the optical configuration, n(n=p/L). For example, n=62.5 for the measurement of the calibrated artifacts, and sensitivity is 785, that is to say, the phase measurement changes 785 times faster than the surface slope changes.

## 7.3 Resolution

Resolution is the smallest change in slope that can be detected for a given optical configuration(p, L, and n). According to a specific application and flaw amplitude, the resolution is adjustable by changing the parameters of the optical configuration. For example, if a coarse pitch grating is used, the resolution is reduced, while the range is increased, and, if a fine pitch grating is used, the resolution is increased, while the range is reduced.

The minimum detected values in slope can be found in the measured slope diagrams for the calibrated artifacts, which are located near the peaks of the waviness. For the artifact with 16 microns peak-to-peak amplitude, they are listed in the Table 7.1.

The mean of the absolute detectable values in slope is $4.19\times10^{-5}$(rad) and the standard deviation is $3.04\times10^{-5}$(rad).

$$\mathrm{Re}\,solution_{slope} \le 4.19\times10^{-5}\,rad \tag{7.3a}$$

$$\mathrm{Re}\,solution_{contour} \le \mathrm{Re}\,solution_{slope} \times \Delta x = 4.19\times10^{-5}\,rad \times 0.871mm = 0.0365\mu m \tag{7.3b}$$

$$\mathrm{Re}\,solution_{second\_derivative} \le \frac{\mathrm{Re}\,solution_{slope}}{\Delta x} = \frac{4.19\times10^{-5}\,rad}{0.871mm} = 4.81\times10^{-5}\,rad\,/\,mm \tag{7.3c}$$

The resolution of the measurement for the calibrated artifacts is shown in the Table 7.2.

## 7.4 The maximum range

In retroreflective metrology, to avoid ambiguity in the phase unwrapping, the maximum phase difference between adjacent pixels can not exceed π. This condition limits the maximum range of measurement between the adjacent pixels in slope and contour. From the slope and phase relationship, we have

$$\begin{aligned}
&\Phi(x) = 4\pi n\theta(x) \\
&|\Delta\Phi(x)|_{max} = 4\pi n|\Delta\theta(x)|_{max} < \pi \\
&|\Delta\theta(x)|_{max} < \frac{1}{4n} \\
&|\Delta Z|_{max} = |\Delta\theta(x)|_{max} \cdot \Delta x < \frac{\Delta x}{4n} \\
&\left|\frac{\Delta\theta(x)}{\Delta x}\right|_{max} < \frac{1}{4n\Delta x}
\end{aligned} \tag{7.4}$$

where

$|\Delta\theta(x)|_{max}$ is the maximum difference in the first derivative(slope) between the adjacent pixels; Δx is the spatial resolution in the field of view; $|\Delta Z|_{max}$ is the maximum difference in depth(contour) between the adjacent pixels; $\left|\frac{\Delta\theta(x)}{\Delta x}\right|_{max}$ is the maximum value in the second derivative allowed on a surface.

For example, in the experiment for the standard artifact with 16μm peak-to-peak amplitude, we have

$$n = 62.5$$
$$\Delta x = 0.8714mm$$

The maximum range for slope measurements between the adjacent pixels is

$$|\Delta\theta(x)|_{max} < \frac{1}{4n} = \frac{1}{4 \times 62.5} = 4 \times 10^{-3}\,rad \tag{7.5a}$$

The maximum range for contour measurements between the adjacent pixels is

$$|\Delta Z|_{max} < \frac{\Delta x}{4n} = \frac{0.871mm}{4 \times 62.5} = 3.5\mu m \tag{7.5b}$$

The maximum range for second derivative measurements between the adjacent pixels is

$$\left|\frac{\Delta\theta(x)}{\Delta x}\right|_{max} < \frac{1}{4n\Delta x} = \frac{1}{4 \times 62.5 \times 0.871mm} = 4.6 \times 10^{-3}\,rad\,/\,mm \tag{7.5c}$$

The maximum range of the measurement between the adjacent pixels for the 16μm calibrated artifact is also shown in the Table 7.2.

## 7.5 The minimum suitable grating pitch in the artifact measurements

As described in section 6.4, the wavelength of waviness on the surface of the artifacts, λ, is 40.0mm and the profile through the wave center can be described as a trigonometric sum of order one, which is repeated here:

$$Z = C_0 + C_1 \cos(\omega_0 x + \gamma) \tag{6.5}$$

where

Z is the depth of each point on the profile;

$\omega_0$ is the spatial frequency[$\omega_0 = 2\pi/\lambda = 0.1571$(rad/mm)];

x is the coordinate along the x direction;

$C_0$, $C_1$, and $\gamma$ are the coefficients [$C_1$=4 μm (or 8 μm) for the waviness with 8μm (or 16μm) peak-to-peak amplitudes, respectively].

The slope and contour of the surface waviness can be found as:

$$\theta(x) = \frac{dZ}{dx} = -C_1\omega_0 \sin(\omega_0 x + \gamma) \tag{7.6a}$$

$$\left|\theta(x)\right|_{max} = C_1\omega_0 \tag{7.6b}$$

$$\dot{\theta}(x) = \frac{d\theta(x)}{dx} = -C_1\omega_0^2 \cos(\omega_0 x + \gamma) \tag{7.7a}$$

$$\left|\dot{\theta}(x)\right|_{max} = C_1\omega_0^2 \tag{7.7b}$$

The maximum slope change in the adjacent pixels can be calculated as:

$$\left|\Delta\theta\right|_{max} = \left|\dot{\theta}(x)\right|_{max} \times \Delta x = C_1\omega_0^2 \Delta x \tag{7.8}$$

For the waviness with 8μm peak-to-peak amplitudes,

$$|\theta(x)|_{max} = C_1\omega_0 = 4\mu m \times 0.157 rad/mm = 6.28 \times 10^{-4} rad \tag{7.9a}$$

$$|\dot{\theta}(x)|_{max} = C_1\omega_0^2 = 4\mu m \times (0.157 rad/mm)^2 = 9.87 \times 10^{-5} rad/mm \tag{7.9b}$$

$$|\Delta\theta|_{max} = C_1\omega_0^2\Delta x = 9.87\times10^{-5} \times 0.871 = 8.60\times10^{-5} rad \tag{7.9c}$$

For waviness with 16μm peak-to-peak amplitudes,

$$|\theta(x)|_{max} = C_1\omega_0 = 8\mu m \times 0.157 rad/mm = 1.26 \times 10^{-3} rad \tag{7.10a}$$

$$|\dot{\theta}(x)|_{max} = C_1\omega_0^2 = 4\mu m \times (0.157 rad/mm)^2 = 1.97 \times 10^{-4} rad/mm \tag{7.10b}$$

$$|\Delta\theta|_{max} = C_1\omega_0^2\Delta x = 1.97\times10^{-4} \times 0.871 = 1.72\times10^{-4} rad \tag{7.10c}$$

From the phase and slope relationship, we have

$$\Phi = 4\pi n\theta = 4\pi\left(\frac{L}{p}\right)\theta \Rightarrow \Delta\Phi = 4\pi\left(\frac{L}{p}\right)\Delta\theta \le \pi \Rightarrow p \ge 4L\Delta\theta \tag{7.11}$$

i.e., p=4LΔθ is the minimum pitch which can be used without causing ambiguity in the phase unwrapping.

For the waviness with 8μm peak-to-peak amplitudes,

$$p_{min} = 4L|\Delta\theta|_{max} = 4 \times 2.50 \times 10^3 mm \times 8.60 \times 10^{-5} = 0.860 mm \tag{7.12a}$$

and for the waviness with 16μm peak-to-peak amplitudes,

$$p_{min} = 4L|\Delta\theta|_{max} = 4 \times 2.5 \times 10^3 mm \times 1.72 \times 10^{-4} = 1.72 mm \tag{7.12b}$$

These minimum pitches are measured on the field of view.

## 7.6 Environment of the measurement

Temperature: 22°C

Humidity: 30%

## 7.7 Conclusions

1) Advantages:

   a) Both DFT and PST can be used to extract the phase information from the deformed grating image and eliminate the variations in background and grating contrast. They are more powerful than simply observing the distorted grating image and ordering the grating image centers

   b) Both DFT and PST used with retroreflective grating technology will accurately yield surface contour and the polarity of a flaw.

   c) Small flaw less than 5μm can be evaluated.

   d) Both methods are optical and non contacting.

   e) Both yield results by definition and need no calibration.

   f) Both yield a 3D view of the surface as opposed to point by point measurements typical of a CMM for example.

   g) Both yield results faster then typical mechanical measurements.

   h) The DFT method requires only one image frame of the surface, which can have advantages if the surface is not stationary.

i) The PST method determines the phase independently at each point without need to consider data from other points in the image.

j) In the PST method, because of the pixel size, many pixels of information each from close proximity are used to determine the phase. This leads to better resolution as compared to the DFT method.

2) Disadvantages:

a) Both methods will only work on quasi flat, specular surfaces.

b) Both methods depend on sufficient Dsight® sensitivity to detect the location of a flaw. Flaws must be slope related.

c) Undersampling leads to cumulative error which is propagated to other areas

d) DFT has the major disadvantage that each point in the surface contour is determined by light from many points on the surface and difficulties with this method are inevitable near edges and at discontinuities.

e) PST has the major disadvantage that it requires four frames of image. The grating has to be physically shifted three times each by a precise amount. It is not applicable for dynamic applications or instances where vibrations make it difficult to constantly step.

3) For a small field of view ($\beta<5°$) the linear equation is simple to use. But for a large field of view ($\beta<5°$), the nonlinear equation has to be used to calculate the slope from the phase information.

4) The 2nd and 3rd optical configurations in the projection grating method can best be used to capture the modulated phase of the grating.

5) Experimental comparisons of the retroreflecting grating measurements with the Rank Taylor Hobson and CMM systems were less conclusive as both of these mechanical probes apply a load to the specimen. Even though this load is small, it caused enough displacement that measurements could not be reliably repeated. As well the operator must visually probe the position of maximum contour deviation.

6) The most useful comparison would appear to come from the calibrated artifacts as the measurements are optical and noncontacting. However no artifact is known to exist which have point by point calibration throughout the surface. While artifact accuracy is guaranted ±1 μm, it is a large percentage of an artifact with 8μm amplitude.

7) Retroreflective grating measurements result by definition hence calibration is not necessary.

From the experiments using the calibrated artifacts, the following specifications can be written.

For the field of view of 262mm by 218mm, L=2500mm, p=40.0mm and using PST and compared to the calibrated artifacts:

(a) The accuracy of peak-to-peak amplitude measurement is 0.78% for the artifact with 0.016mm wave amplitude and 3.96% for the artifact with 0.008mm wave amplitude.

(b) The precision of peak-to-peak amplitude measurement is 0.811μm for the artifact with 0.016mm peak-to-peak amplitude and 0.591μm for the artifact with 0.008mm peak-to-peak amplitude.

(c) The sensitivity of phase shift versus slope change is 785 radians/radians.

(d) The resolution in slope is $4.19\times10^{-5}$radians for the adjacent pixels on the object surface, the resolution in contour is 0.0365μm, and the resolution in the second derivative is $4.81\times10^{-5}$radians/mm.

(e) The maximum range for slope measurements is $4.00\times10^{-3}$radians for the adjacent pixels. The maximum range for contour measurements is 3.50μm. The maximum range for the second derivative measurements is $4.60\times10^{-3}$ radians/mm.

(f) Range can be extended , against a loss of resolution, by increasing the pitch p of the grating.

Retroreflective grating metrology can identify the slope variation pixel by pixel. As a result, it has better resolution than Dsight, which determines the relative severity of a flaw by the area of the flaw as well as the gray level variations as a result of the flaw.

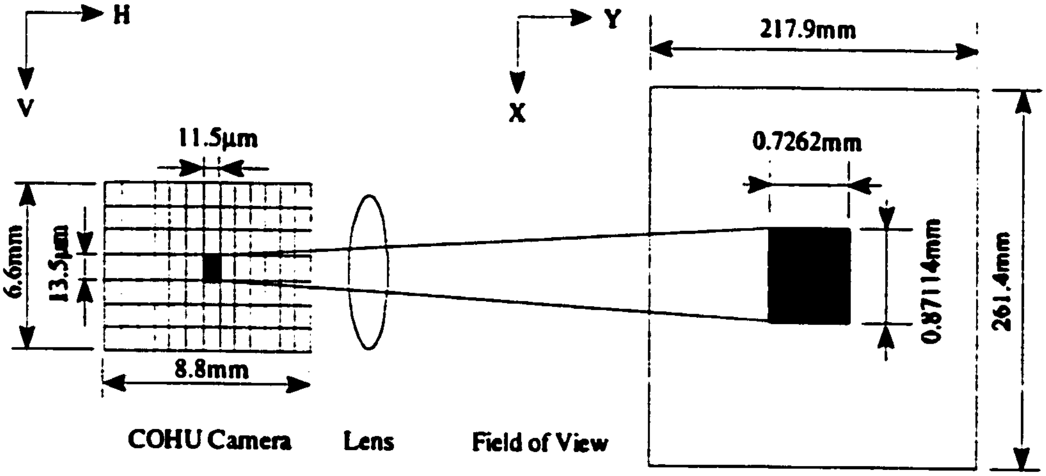

Figure 7.1 The demagnification of the optical system

| Peak No. (n) | Location (pixel) | Slope detected (radian) |
|---|---|---|
| 0 | 16 | $-6.59\times10^{-5}$ |
| 1 | 39 | $+4.36\times10^{-6}$ |
| 2 | 62 | $+2.61\times10^{-5}$ |
| 3 | 85 | $-2.06\times10^{-5}$ |
| 4 | 109 | $+4.45\times10^{-5}$ |
| 5 | 132 | $+5.93\times10^{-5}$ |
| 6 | 155 | $-3.02\times10^{-5}$ |
| 7 | 177 | $+1.82\times10^{-5}$ |
| 8 | 201 | $+1.31\times10^{-4}$ |
| 9 | 226 | $+4.12\times10^{-5}$ |
| 10 | 247 | $+3.44\times10^{-5}$ |
| 11 | 272 | $-2.44\times10^{-5}$ |
| 12 | 293 | $-4.47\times10^{-5}$ |

**Table 7.1 The minimum detected values in slope**

**($\text{mean}\pm\sigma=4.19\times10^{-5}\text{rad}\pm3.04\times10^{-5}\text{rad}$)**

|  | The first derivative(slope) | Contour | The second derivative |
|---|---|---|---|
| Resolution | $4.19\times10^{-5}$rad | 0.0365μm | $4.81\times10^{-5}$rad/mm |
| Max range | $4.00\times10^{-3}$rad | 3.50μm | $4.60\times10^{-3}$rad/mm |

Table 7.2 The resolution and max range of the measurement between the adjacent pixels for the calibrated artifacts

# Chapter 8

# Recommendations for Future Work

## 8.1 Optomechatronics

1) Refine the concept and investigate its impact on engineering research and education;
2) Study the possibility of developing some generic module(software and/or hardware) for optomechatronic products by using cheap and available components. The module should be compatible with the future trends of optomechatronics.

## 8.2 Retroreflective metrology

While the research done so far indicates the retroreflective metrology is efficient and practical, further research might be done in the following directions:

1) to create uniform gratings using the moiré method since it makes it simple and flexible to change the grating pitch;
2) to study the effect of the gratings with different pitches, profiles and patterns;
3) to build a more sophisticated mathematical model for true 3D measurements to improve the resolution of retroreflective metrology;
4) to use high dimensional DFTs and more complicated PSTs, and investigate their advantages and disadvantages;
5) to analyze the retroreflective grating image by using Wavelets Transform(WT)[74];

6) to develop more robust phase unwrapping algorithms;
7) to develop a model for large angle of incidence typical of industrial Dsight® applications;
8) to add this technology to the existing D Sight process. In the long term, this would result in a new product for commercial exploitation;
9) Since 56% of the possible experiment error come from lens resolution (Table C.2), it is necessary to investigate methods to reduce this.

## 8.3 3D surface measurement

1) to apply the retoreflective metrology to non-reflective surfaces by using a hi-lighting fluid to make them specular;
2) to use C++ and OOP to develop an automatic off-line software tool for retroreflective grating analysis;
3) to use VLSI and Parallel computing architecture to build a real-time on-line system for non-contacting surface measurement;
4) to transfer the technique to a specific industrial application like surface quality inspection and quality control of automobile bodies;
5) to research the possibility of adding this technology to the existing D Sight process to quantify defects on aircraft surfaces such as the fuselage or to detect lap splice corrosion;
6) to apply retoreflective metrology for quality control of computer disc drives.

# References

## Optomechatronics

[1] Terry S. Reynolds, editor, "The Engineering in America: a historical anthology from technology and culture", The University of Chicago Press, Chicago, 1991.

[2] Board on Engineering Education, Commission on Engineering and Technical Systems, Office of Scientific and Engineering Personnel, National Research Council, "Engineering Education: design an adaptive system", National Academy Press, Washington, D. C., 1995.

[3] ONR European Office, Newsletter#54 on electronics by Nick Bottka, Report on NATO Advanced Research Workshop on Future Trends in Microelectronics, 7-Aug-95. http://www.ehis.navy.mil/nbnews54.htm.

[4] Heather Menzies, "Who Braves New World: the information highway and new economy", Between The Lines, Toronto, Canada, 1996.

[5] Fatemeh Zahedi, "Intelligent Systems for Business: Expert Systems with Neural Networks", Wadsworth Publishing Company, Belmont, California, 1993.

[6] Center for Information Research(CIT), Standford University. http://logic.standford.edu/cit/cit.html.

[7] Msc Mechatronics and Optical Engineering, Mechatronics Group, Department of Mechanical Engineering, Loughborough University.

http://info.lut.ac.uk/mechatronics.html.

[8] International Conference on Micromechatronics for Information and Precision Equipment(MIPE'97), July 22, 1997, International Forum, Tokyo, Japan.

[9] Nan's Parallel Computing page. http//www.cs.rit.edu/~ncs/parallel.html.

[10]Institute for Real-Time Computer Systems & Robotics(IPR), University of Karlsruhe. http://i60s30.ira.uka.de/areas/parallel.html.

[11] Department of Artificial Intelligence, University of Edinburgh. http://www.dai.ac.uk/AI_at_Edinburgh_perspective.html.

[12] Japanese Trend'96, "Unity of Knowledge and action" in the age of the information revolution. http://www.dihs.co.jp/reseach/CHORYU96/CHORYU96_E.html.

[13] NTT Interdisciplinary Laboratories, Nippon Telephone and Telegraph Corporation. http://itri.loyala.edu/mems/c_ntt.html.

[14] Etcheverry MEMS Lab, Department of Mechanical Engineering, University of California at Berkeley. http://mems.me.berkeley.edu.

[15] D. M. Rowe, editor, "CRC Handbook of thermoelectronics", CRC Press 1995.

[16] Peter Van Zant, "Microchip Fabrication: A Practical Guide to Semiconductor Processing", McGraw-Hill Inc., 1996.

[17] Xianzhu Zhang, "Thermal Design of Computer Packaging Substrates", Electronic Machinery Engineering, Vol. 42, No. 2, p35-41, 1993.

[18] Xianzhu Zhang, "An Efficient Optomechatronic System for 3D Surface Inspection", Techanical Report, Department of Mechanical & Materials Engineering, University of

Windsor, December, 1996.

[19] Xianzhu Zhang, "Optomechatronics—An Overview to Modern Technology", the Electronic Journal of Engineering Technology: the Technology Interface, Fall 1998. http://et.nmsu.edu/~etti/fall98/mechanical/zhang/zhang.html.

## Retroreflective Metrology for 3D Surface Measurement

[20] Daniel Malacara, "A Review of Interferogram Analysis Methods", SPIE Vol. 1332, Optical Testing and Metrology III: Recent Advanced in Industrial Optical Inspection (1990)

[21] H. Philip Stahl, " Review of Phase-measuring Interferometry", SPIE Vol. 1332, Optical Testing and Metrology III: Recent Advanced in Industrial Optical Inspection (1990)

[22] K. E. Perry, Jr. and J. McKelvie, "A Comparison of Phase Shifting and Fourier Methods in the Analysis of Discontinuous Fringe Patterns", Optics and Lasers in Engineering 19(1993).

[23] Mitsuo Takeda, "Current trends and future directions of fringe analysis," SPIE Vol. 2544(1995).

[24] Yves Surrel, "Morie and Grid Methods: A Signal Processing Approach", SPIE Vol. 2342 Photomechanics(1994).

[25]C. C. Soh, S. M. Shang, F. S. Chau, and Y. Y., Hung, "The Use of Holographic Phase Shifting in Assessing Unbonds in GRP Plates", Journal of Engineering Materials

and Technology, October 1994, Vol.116.

[26] Jie Gu, Y. Y. Hung, and Fang Chen, "Iteration Algorithm for Computer-aided Speckle Interferometry", Applied Optics/Vol.33 No.23/10 August 1994.

[27] Joseph Der Hovanesian and Y. Y. Hung, "Sheargraphy for Discontinuity Dection", Materials Evaluation/June 1995.

[28] S. H. Tang, Y. Y. Hung and Q. Zhu, "A New Measurement for Non-monotonical Fringe Patterns", SPIE Vol. 1332, Optical Testing and Metrology III: Recent Advanced in Industrial Optical Inspection (1990)

[29] Y.Y. Hung, G.C. Jin and S.H. Tang, "Surface Inspection of Automotive Bodies by Reflective Computer Vision", SPIE Vol. 955 Industrial Laser Interferometry II(1988).

[30] Y.Y. Hung, J. Q. Wang, and Keyu Li, "Dual Beam Digital Sheargraphy for Full-field Measurement of In-phase Strain", EEP-Vol. 10-2, Advances in Electronic Packaging, ASME 1995.

[31] Y.Y. Hung, S.H. Tang and Q. Zhu, "3-D Surface Inspection Using Interferometric Grating and 2-D FFT Based Technique", SPIE Vol.1332 Optical Testing and Metrology III: Recent Advances in Industrial Optical Inspection(1990).

[32] Y. Y. Hung, S. Tang, and J. D. Hovanesian, "Real-time Sheargraphy for Measuring Time-dependent Displacement Derivatives", Experimental Mechanics/March,1994.

[33] Y. Y. Hung, T. P. Leung, and F. S. Chau, "Direct Determination of Derivatives of Holographically Recorded Displacement by an Optical Diffraction Technique", Journal of Strain Analysis, Vol.25, No. 3,1990.

[34] D. P. Towers, T. R. Judge, and P. J. Bryanston-cross, " Automatic Interferogram Analysis Techniques Applied to Quasi-heterodyne Holography and ESPI", Optics and Lasers in Engineering 14(1991).

[35] Gordon D. Lassahn, "Automatic High Resolution Analysis of Low-Noise Fringes", SPIE Vol.1332 Optical Testing and Metrology III: Recent Advances in Industrial Optical Inspection(1990).

[36] Gordon M. Brown, "Fringe Analysis for Automotive Applications", Optics and Lasers in Engineering 19 (1993).

[37] Haruhisa Kurokawa, Naoki Inhikawa and Nobuyuki Yajima, "Fringe Scanning Moiré System Using a Servo Controlled Grating", SPIE Vol.1332 Optical Testing and Metrology III: Recent Advances in Industrial Optical Inspection(1990).

[38] H. Philip Stahl," White-Light Morie Phase-Measuring Interferometry", SPIE Vol.1332 Optical Testing and Metrology III: Recent Advances in Industrial Optical Inspection(1990).

[39] J. Schorner, A. Ettemeyer, U. Neupert, H. Rottenkolber, C. Winter and P. Obermeier, "New Approaches in Interpreting Holographic Images", Optics and Lasers in Engineering 14(1991).

[40] Meiyuan Wen and Guangting Liu, "New Technique for Multiplying the Isoclinic Fringes", SPIE Vol.1332 Optical Testing and Metrology III: Recent Advances in Industrial Optical Inspection(1990).

[41] Jerzy P. Komorowski, Shankar Krishnakumar, Ronald W. Gould, Nicholas, C.

Bellinger, Frank Karpala, and Omer L. Hageniers, "Double Pass Retroreflection for Corrosion Detection in Aircraft Structures", Materials Evaluation / January 1996 /Vol. 32 No.9.

[42] Qin Geng, "Retro-reflective Optics to Determine Stress Resulting from Interlaminar Corrosion in Fuselage Lap Joints", M. A. Sc. Thesis, University of Windsor, 1996.

[43] R. L. Reynolds, F. Karpala, and O. L. Hageniers, "Theory and Applications of a Surface Inspection Technique Using Double-pass Retroreflection", Optical Engineering, Vol. 33, pp. 2122-2129, 1993.

[44] Rodger L. Reynolds and Omer L. Hageniers, "Surface Quality Measurement on Sheet Metal Stampings", 1989 international Conference and Exposition, May1-4, 1989, Detroit, Michigan.

[45] Till W. Liepmann, "How Retroreflectors Bring the Light Back", Laser Focus World, October, 1994.

[46] Walter G. Egan, "Laser Retroreflectance", SPIE Vol. 1747 Polarization and Remoate Sensing.

[47] Donald J. Bone, "Fourier Fringe Analysis: the Two-dimensional Phase Unwrapping Problem", 1 September 1991 / Vol. 30, No. 25 / Applied Optics.

[48] Donald J. Bone, H.A. Bachor, and R. John Sandeman, "Fringe-pattern Analysis Using a 2-D Fourier Transform", 15 May 1986 / Vol. 25, No. 10 / Applied Optics.

[49] Maher A. Sid-Ahmed, "Image Processing: Theory, Algorithms, and Architectures", McGraw-Hill Inc. 1995.

[50] Mitsuo Takeda, Hideki Ina and Seiji Kobayashi, "Fourier-transform method of fringe-pattern analysis for computer-based topography and interferometry," J. Opt. Soc. Am. Vol. 72, No.1 January 1982

[51] William W. Macy, Jr., "Two-dimensional Fringe-pattern Analysis", Applied Optics / Vol. 22, No. 23 / 1 December 1983.

[52] A. Apik, "Investigation of the Cellular Automata Method for Phase Unwrapping and Its Implementation on an Array Processor", Optics and Lasers in Engineering 14 (1991) 25-37.

[53] David R. Burton and Michael J. Lalor, "Multichannel Fourier Fringe Analysis as an Aid to Automatic Phase Unwraping", May 1995/Vol. 33, No. 14/Applied Optics.

[54] J. M. Huntley, "Noise-immune Phase-unwrapping Algorithm", Applied Optics/Vol. 28, No. 15/15 August 1989.

[55] J. M. Huntley and H. Saldner, "Temporal Phase-unwrapping Algorithm for Automated Interferogram Analysis", June 1993 / Vol. 32, No. 17 / Applied Optics.

[56] Qian Lin, John F. Vesecky, and Howard A. Zebker, "Phase Unwrapping through Fringe-line detection in Synthetic Aperture Radar Interferometry", January, 1994/Vol. 33,No.2/Applied Optics.

[57] R. Cusack, J. M. Huntley and H. T. Goldrein, "Improved Noise-immuse Phase-unwrapping Algorithm", Applied Optics/Vol.34 , No. 5/ February 1995.

[58] T. R. Judge and P. J. Bryanston-Cross, "A Review of Phase Unwrapping Techniaues in Fringe Analysis", Optics and Lasers in Engineering 21(1994).

[59] A. Asundi and C. S. Chan, "Phase Shifting Applied to Non-sinusoidal Intesity Distribution --An Error Simulation", Optics and Lasers in Engineering 21(1994)

[60] A. Asundi and C. S. Chan, "Phase Shifting Projection Grid—Effect of Pitch and Profile", Optics and Lasers in Engineering 21(1994)

[61] C.S. Chan and A. Asundi, "Phase Shifting Digital Projection System for Surface Measurement", Proc. SPIE Vol. 2354, pp. 444-452, 1994.

[62] Chiayu Ai and James C. Wyant, "Effect of Retroreflection on a Fizeau Phase-shifting Interferometer", Applied Optics/ Vol. 32, No. 19/ 1 July 1993.

[63] Gary L. Cloud, "Optical Methods of Engineering Analysis", Cambridge University Press 1995.

[64] Jacob Woisetschlager, Daniel B. Sheffer, C. William Loughry, Kavitha Somasundaram, Surendra K. Chawla, and Piotr J. Wesolowski, "Phase-shifting Holographic Interferometry for Breast Cancer Dection", August 1994/ Vol.33, No. 22/ Applied Optics.

[65] K. Ramesh and S. K. Mangal, "Automation of Data Acquisition in Reflection Photoelasticity by phase shifting Methodology", the Journal Of the British Society of Strain Measurement: Strain, Vol. 33, No.3, August, 1997.

[66] Booth, Kathryn M. and Hill, Steven L., "The Essence of Optoelectronics", Prentice Hall Europe, Hertfordshire, UK, (1998).

[67] Isaacson, Eugene and Keller, Herbert Bishop, "Analysis of Numerical Methods", John Wiley & Sons, Inc., New York, USA, (1966).

[68] Madisetti, Vijay K. and Williams, Douglas B.,"The Digital Signal Processing Handbook", CRC Press LLC, Boca Raton, FL, USA (1998).

[69] Holst, Gerald C., "Sampling, Aliasing, and Data Fidelity for Electronic Imaging Systems, Communications, and Data Acquisition", JCD Publishing, Winter Park, FL, USA, (1998).

[70] Taylor, John R., "An Introduction to Error Analysis", University Science Books, Mill Valley, CA,(1982).

[71] Jacobs, D., "The State of the Art in Numerical Analysis", Academic Press Inc., New York, USA, (1977).

[72] Wegman, Edward J., "Statistical Signal Processing", Marcel Dekker, Inc., New York, USA,(1984).

[73] Ambardar, Ashok, "Analog and Digital Signal Processing", PWS Publishing Company, Boston, USA, (1995).

[74] Olivier Rioul and Martin Vetterli, "Wavelets and Signal Processing", IEEE SP Magazine, October 1991.

[75] B. K. Johnson, "Optics and Optical Instruments", Dover Publications, Inc., New York, 1960.

[76] W. T. Welford, "Geometrical Optics and Optical Instrumentation", North-Holland Publishing Company, Amsterdam, 1962.

[77] Rudolf Kingslake, "Applied Optics and Optical Engineering", Vol. III, Optical Components, Academic Press, New York and London, 1965.

[78] Joseph Morgan, "Introduction to Geometrical and Physical Optics", New York, Toronto and London, McGraw-Hill Book Company. Inc., 1953.

[79] M. Fogiel, Director, "Handbook of Mathematical. Scientific, and Engineering Formulas, Tables, Functions, Graphs, Transforms", Research and Education Association. USA, 1992.

[80] Athanasios Papoulis, "The Fourier Integral and Its Applications", McGraw-Hill Book Company, Inc., New York, San Francisco, London, and Toronto, 1962

[81] M. B. Priestley, "Spectral Analysis and Time Series", Academic Press, London, 1981.

[82] G. H. Rieke, "Detection of Light: From the Ultraviolet to the Submillimeter", Cambridge University Press 1994.

[83] Allen Nussbaum and Richard A. Philips, "Contemporary Optics for Scientists and Engineers", Prentice-Hall, Inc., 1976.

[84] P. Das, "Laser and Optical Engineering", Springer-Verlag Inc., 1991.

[85] Charles. S. Williams and Orville A. Becklund, "Optics: A Short Course for Engineers & Scientists", John Willey & Sons, 1972.

[86] Bernard Picinbono, "Random Signals and Systems", Prentice Hall, 1993.

[87] Mischa Schwartz, "Information Transmission, Modulation, and Noise", McGraw-Hall Book Company, 1970.

[88] Nirode Mohanty, "Random Signals Estimation and Identification: Analysis and Applications", Van Nostrand Reinhold Company Inc. 1986.

[89] Dsight® Application Note, 92-03, Diffrato Limited, 2835 Kew Drive, Windsor, Ontario, Canada.

# Appendix A:

# Relevant Publications

[1] Xianzhu Zhang and Walter P.T. North, "Analysis of 3D Surface Waviness on Standard Artifacts by Retroreflective Metrology", Optical Engineering, Vol. 39, No. 1, pp 183-186, 2000.

[2] Xianzhu Zhang and Walter P.T. North, "Retroreflective Projection Gratings", Optics & Laser Technology, Vol. 31, No. 5, pp369-372, 1999.

[3] Xianzhu Zhang and Walter P.T. North, "Contour Inspection of Automotive Sheet Metal by Efficient Optomechatronics", published in 32nd International Symposium on Automotive Technology & Automation, Vienna, Austria, June 14-18, 1999.

[4] Xianzhu Zhang and Walter P.T. North, "Phase Shifting Method for Retroreflective Grating Analysis", the Journal of the British Society for Strain Measurement: Strain, Vol. 34, No. 4, pp. 123-126, 1998.

[5] Xianzhu Zhang and Walter P.T. North, "Retroreflective Grating Analysis VS Physical Measurements on Surface Contour", Optical Engineering, Vol. 37, No. 5, pp. 1464-1467, 1998.

[6] Xianzhu Zhang and Walter P.T. North, "Retroreflective Grating Generation and Analysis for Surface Measurement", Applied Optics, Vol. 37, No. 13, pp. 2624-2627, 1998.

# Appendix B:

# Most Significant Contributions

1) Optomechatronics is discussed comprehensively as a philosophy and illustrated by retroreflective metrology as an instance;
2) This represents the first time that PST and DFT was used in conjunction with retroreflective optics to quantify a surface;
3) Three optical configurations were tested;
4) Because of the unique properties of retroreflective optics, a nonlinear equation was developed explicitly in optical metrology, to eliminate nonlinear errors in the results;
5) This represents the first time that calibrated artifacts were used to verify the optical measurement of slope and contour;
6) Retroreflective metrology is one of the most precise among the existing optical methods. It is a new optical technique for surface measurement, which is efficient and practical.
7) It can be developed for machine vision and industrial application in Nondestructive Testing and Evaluation (NDTE).

# Appendix C

# Error Analysis

## C.1 The Resolving power of Lens

The lens used in the measurement is Universal Optical CCTV Zoom lens(12.5-75mm, f/1.8, MACRO). The parameters of the lens system are set as: object distance u is 813mm, focal length f is 12.5mm, and aperture is f/8. The bar line target on the Paterson Optical Test Target 2 was used to measure the resolution of the lens. The target was originally calibrated for use at 27×focal length and measured from the film plane in line pairs per millimeter with the range of 7-48 line pairs per millimeter(l.p.p.m).

Shown in Figure C.1 is the configuration of a resolution test. The bar line target was located at the object distance u. The bar line target is shown in Figure C.2 and its image in Figure C.3.

Figure C.3 indicates that the line pairs are indistinguishable at the position of approximately 3lines/5mm[0.60 l.p.p.mm] on the target, which was determined by visual inspection. From the image formation condition, we have

$$\frac{1}{u}+\frac{1}{v}=\frac{1}{f}\Rightarrow v=\frac{u-f}{uf}=\frac{813-12.5}{813\times 12.5}=12.7mm \tag{C.1a}$$

The lateral magnification is

$$m_x=1-\frac{v}{f}=-\frac{v}{u}=-\frac{12.7}{813}=-15.6\times 10^{-3} \tag{C.1b}$$

The resolution measured from the CCD imager is equivalent to

$$\mathrm{Re}\,solution = \frac{3lines/5mm}{|m_x|} = \frac{3lines/5mm}{15.6\times10^{-3}} = 38.4(l.p.p.m) \qquad \text{(C.2)}$$

## C.2 Intensity uncertainties resulting from lens resolution, camera contrast variation, and mechanical shifting

Shown in Figure C.4 is the spatial carrier of the measurement, which is the image of the grating from the flat surface as captured by the camera. The characteristics of the spatial carrier are: the period T is 12 pixels(10.5mm), the spatial frequency $\omega_0$ ($2\pi/T$) is 0.456 rad/mm, the average A is 123.3, and the amplitude B is 46.7.

For the PST method, the intensity of the image captured by camera was modeled as Eq. 4.1, which can be simplified as:

$$i(x) = A + B\cos[(\omega_0 x + \Phi(x) + \alpha] \qquad \text{(C.3)}$$

where A and B represent the unwanted errors arising from the variations of the background intensity and grating contrast, respectively; $\omega_0$ is the spatial frequency of the grating in the x direction, $\Phi(x,y)$ is the phase of the deformed grating; $\alpha$ is a known added phase difference.

The resolution of lens measured from the field of view is 3 lines/5mm(1 line/1.67mm), which means that, at an arbitrary position x, the image intensity is the average over $x-0.83<x<x+083$mm($-0.83<\Delta x<+0.83$). This results in the intensity uncertainty as derived in following equation.

$$
\begin{aligned}
|\Delta i|_{lens} &= \left|\frac{di(x)}{dx}\right||\Delta x| = |-B\omega_0 \sin[\omega_0 x + \Phi(x) + \alpha]||\Delta x| \le B\omega_0|\Delta x| \\
|\Delta i|_{lens,max} &= 46.7 \times 0.456 \times 0.835 = 17.6
\end{aligned}
\tag{C.4}
$$

There is mechanical error in the phase shifting of grating, which is about p/4±0.1mm(1.25±0.1mm) and is equivalent to π/2(1±0.08)rad in α. This results in the intensity uncertainty as derived in following equation.

$$
\begin{aligned}
|\Delta i|_{mechanical} &= \left|\frac{di(x)}{d\alpha}\right||\Delta \alpha| = |-B \sin[\omega_0 x + \Phi(x) + \alpha]||\Delta \alpha| \le B|\Delta \alpha| \\
|\Delta i|_{mechanical,max} &= 46.7 \times \frac{\pi}{2} \times 0.08 = 5.86
\end{aligned}
\tag{C.5}
$$

The camera(COHU 4810 Series Solid-State CCD Camera) has a contrast variation of less than 5% overall @25°C. This is equivalent to the intensity uncertainty as derived in following equation.

$$
\frac{|\Delta i|_{camera,max}}{A} = 5\% \Rightarrow |\Delta i|_{camera,max} = A \times 5\% = 123.3 \times 5\% = 6.17 \tag{C.6}
$$

The effect of these possible errors is discussed in the section C.5 and summarized in Table C.2.

## C.3 Error analysis of PST

It is estimated that PST reduces the possible error by 100/1 [61]. The following derivation is a proof for the estimation. We start with Eq.(4.3), which is repeated here.

$$
\Phi = \tan^{-1}\left(\frac{i_4 - i_2}{i_1 - i_3}\right) \tag{4.3}
$$

$$\sigma_\Phi = \sqrt{\left(\frac{\partial\Phi}{\partial i_4}\sigma_{i_4}\right)^2 + \left(\frac{\partial\Phi}{\partial i_2}\sigma_{i_2}\right)^2 + \left(\frac{\partial\Phi}{\partial i_1}\sigma_{i_1}\right)^2 + \left(\frac{\partial\Phi}{\partial i_3}\sigma_{i_3}\right)^2}$$

$$\sigma_\Phi = \frac{1}{1+\left(\frac{i_4-i_2}{i_1-i_3}\right)^2}\sqrt{\left(\frac{1}{(i_1-i_3)}\sigma_{i_4}\right)^2 + \left(\frac{1}{(i_1-i_3)}\sigma_{i_2}\right)^2 + \left(\frac{(i_4-i_2)}{(i_1-i_3)^2}\sigma_{i_1}\right)^2 + \left(\frac{(i_4-i_2)}{(i_1-i_3)^2}\sigma_{i_3}\right)^2}$$

$$\sigma_\Phi = \frac{1}{1+\left(\frac{i_4-i_2}{i_1-i_3}\right)^2 (i_1-i_3)^2}\sqrt{(i_1-i_3)^2(\sigma_{i_4}{}^2+\sigma_{i_2}{}^2)+(i_4-i_2)^2(\sigma_{i_1}{}^2+\sigma_{i_3}{}^2)}$$

$$\sigma_\Phi = \frac{1}{(i_1-i_3)^2+(i_4-i_2)^2}\sqrt{(i_1-i_3)^2(\sigma_{i_4}{}^2+\sigma_{i_2}{}^2)+(i_4-i_2)^2(\sigma_{i_1}{}^2+\sigma_{i_3}{}^2)}$$

Assumes that $\sigma_{i_1} = \sigma_{i_2} = \sigma_{i_3} = \sigma_{i_4} = \sigma_i$

$$\sigma_\Phi = \frac{1}{(i_1-i_3)^2+(i_4-i_2)^2}\sqrt{2\sigma_i{}^2[(i_1-i_3)^2+(i_4-i_2)^2]}$$

$$\sigma_\Phi = \frac{\sqrt{2}\sigma_i}{\sqrt{[(i_1-i_3)^2+(i_4-i_2)^2]}}$$

Since $i_1 = A + B\cos[\omega_0 x + \Phi(x)]$

$$i_2 = A + B\cos[\omega_0 x + \Phi(x) + \frac{\pi}{2}] = A + B\sin[\omega_0 x + \Phi(x)]$$

$$i_3 = A + B\cos[\omega_0 x + \Phi(x) + \pi] = A - B\cos[\omega_0 x + \Phi(x)]$$

$$i_4 = A + B\cos[\omega_0 x + \Phi(x) + \frac{3\pi}{2}] = A - B\sin[\omega_0 x + \Phi(x)]$$

we have

$$i_1 - i_3 = 2B\cos[\omega_0 x + \Phi(x)]$$

$$i_4 - i_2 = -2B\sin[\omega_0 x + \Phi(x)]$$

$$\sigma_{\Phi} = \frac{\sqrt{2}\sigma_t}{\sqrt{\{2B\cos[\omega_0 x + \Phi(x)]\}^2 + (-2B\sin[\omega_0 x + \Phi(x)]\}^2}} = \frac{\sqrt{2}\sigma_t}{2B} = \frac{\sigma_t}{\sqrt{2}B} \tag{C.7}$$

The equation C.7 shows that the possible error in phase can be substantially reduced by choosing a large grey level for the amplitude B, as recorded in the Matrox image grabber, which is shown in Table C.1.

## C.4 Error analysis in slope calculation

The slope is related to the phase information in the grating image by Eq. (4.2):

$$\theta(x) = \frac{\Phi(x)}{4\pi n} = \frac{\Phi(x)}{4\pi}\frac{p}{L} \tag{4.2}$$

where Φ(x,y) is the phase of the deformed grating; θ is the local slope of the surface of the specimen; n(n=L/p) is the optical amplification of the system; L is the distance between the specimen surface and retroreflective screen; and p is the pitch of the grating. The error in the measurement of pitch on the retroreflective screen is estimated as 40±1mm and the error in distance L is about 250±1cm. From Eq 4.2, we have

$$|\Delta\theta|_{\Phi} = \left|\frac{d(\theta(x))}{d\Phi}\right| \cdot |\Delta\Phi| = \frac{P}{4\pi L} \cdot |\Delta\Phi| \tag{C.8}$$

$$|\Delta\theta|_{p} = \left|\frac{d(\theta(x))}{dp}\right| \cdot |\Delta p| = \frac{|\Phi(x)|}{4\pi L} \cdot |\Delta p| \tag{C.9}$$

$$|\Delta\theta|_{L} = \left|\frac{d(\theta(x))}{dL}\right| \cdot |\Delta L| = \frac{|\Phi(x)| \cdot p}{4\pi L^2} \cdot |\Delta L| \tag{C.10}$$

From the phase and slope relationship, we have

$$\Phi(x) = 4\pi n\theta(x) \Rightarrow |\Phi(x)|_{\max} = 4\pi n|\theta(x)|_{\max} \tag{C.11}$$

For the waviness with 8μm and 16μm peak-to-peak amplitudes, the maximum slopes are $6.28\times10^{-4}$(rad) and $1.26\times10^{-3}$(rad) as calculated in equations 7.9a and 7.10a, respectively.

$$|\Delta\theta|_{p,\max} = \frac{|\Phi(x)|_{\max}}{4\pi L}\cdot|\Delta p| = \frac{4\pi n|\theta(x)|_{\max}}{4\pi L}\cdot|\Delta p| = \frac{|\theta(x)|_{\max}}{p}\cdot|\Delta p| \tag{C.12}$$

$$|\Delta\theta|_{L,\max} = \frac{|\Phi(x)|_{\max}\cdot p}{4\pi L^2}\cdot|\Delta L| = \frac{4\pi n|\theta(x)|_{\max}\cdot p}{4\pi L^2}\cdot|\Delta L| = \frac{|\theta(x)|_{\max}}{L}\cdot|\Delta L| \tag{C.13}$$

## C.5 Error analysis of retroreflective metrology

Table C.2 summarizes the error transmission and distribution in the retroreflective analysis of the artifact with 16μm peak-to-peak amplitude. The values are calculated by using the equations derived in the previous sections.

## C.6 Error Analysis of DFT method

One Dimensional DFT: $F(n) = \sum_{k=0}^{N-1} f(k)e^{-j\frac{2\pi}{N}nk}$

1D Inverse DFT: $f(k) = \frac{1}{N}\sum_{n=0}^{N-1} F(N)e^{j\frac{2\pi}{N}nk}$

Some Properties of the DFT:

Linearity: $f_3(k) = af_1(k) + bf_2(k) \Leftrightarrow F_3(n) = aF_1(n) + bF_2(n)$

Symmetry: $F(N-n) = F(n)^*$

Periodicity: $F(-n) = F(N-n) \quad and \quad f(-k) = f(N-k)$

For the DFT method, the grey level image captured by the camera was modeled as:

$$i(k) = A + B\cos[\frac{2\pi}{p}(kdx) + \Phi_i] = A + B\cos[2\pi f_0 k + \Phi_i] \quad where \quad f_0 = \frac{dx}{p}$$

$$i(k) = A + \frac{1}{2}Be^{j(2\pi f_0 k + \Phi_i)} + \frac{1}{2}Be^{-j(2\pi f_0 k + \Phi_i)} = A + c(k)e^{j2\pi f_0 k} + c(k)^{*}e^{-j2\pi f_0 k}$$

with

$c(k) = \frac{1}{2}Be^{j\Phi_i}$ k=0, 1, 2, ..., N-1.

It is assumed that The bandwidth of C(n)=DFT[c(k)] is $\Delta f = 2M + 1$

and $\sigma_{i(k)} = \sigma_i$ k=0, 1, 2, ..., N-1.

$$I(n) = I_x(n) + jI_y(n) = \sum_{k=0}^{N-1} i(k)e^{-j\frac{2\pi}{N}nk} = \sum_{k=0}^{N-1}\left[i(k)\cos(\frac{2\pi}{N}nk)\right] + j\sum_{k=0}^{N-1}\left[i(k)\sin(\frac{2\pi}{N}nk)\right]$$

$$\sigma^2_{I(n)} = \sigma^2_{I_x(n)} + \sigma^2_{I_y(n)} = \sum_{k=0}^{N-1}\left[\sigma_{i(k)}\cos(\frac{2\pi}{N}nk)\right]^2 + \sum_{k=0}^{N-1}\left[\sigma_{i(k)}\sin(\frac{2\pi}{N}nk)\right]^2$$

$$\sigma^2_{I(n)} = \sigma_i^2\sum_{k=0}^{N-1}\left[\frac{1+\cos(\frac{4\pi}{N}nk)}{2}\right] + \sigma_i^2\sum_{k=0}^{N-1}\left[\frac{1-\cos(\frac{4\pi}{N}nk)}{2}\right]$$

$$\sigma^2_{I(n)} = \sigma_i^2\,\frac{N + \sum_{k=0}^{N-1}\cos(\frac{4\pi n}{N}k)}{2} + \sigma_i^2\,\frac{N - \sum_{k=0}^{N-1}\cos(\frac{4\pi n}{N}k)}{2}$$

$$\sigma^2_{I(n)} = \sigma^2_{I_x(n)} + \sigma^2_{I_y(n)} = \sigma_i^2\frac{N}{2} + \sigma_i^2\frac{N}{2} = N\sigma_i^2 \qquad \text{(C.14)}$$

C(n)=I(f₀+n), n=0, 1, 2, ..., M

C(n)=0, n=M+1, M+2, …, N-M-1

C(n)=I(f$_0$+n-N), n=N-M, N-M+1, …, N-1

$\sigma^2_{C(n)} = \sigma^2_{C_x(n)} + \sigma^2_{C_y(n)} = \sigma_i^2 \frac{N}{2} + \sigma_i^2 \frac{N}{2} = N\sigma_i^2$, n=0, 1, …, M or N-M, N-M+1, …, N-1

$\sigma^2_{C(n)} = \sigma^2_{C_x(n)} = \sigma^2_{C_y(n)} = 0$, n=M+1, M+2, …, N-M-1

$$c(k) = c_x(k) + jc_y(k) = \frac{1}{N}\sum_{n=0}^{N-1} C(n)e^{j\frac{2\pi}{N}nk} = \frac{1}{N}\left[\sum_{n=0}^{M} C(n)e^{j\frac{2\pi}{N}nk} + \sum_{n=N-M}^{N-1} C(n)e^{j\frac{2\pi}{N}nk}\right]$$

$$c(k) = \frac{1}{N}\left[\sum_{n=0}^{M} C(n)e^{j\frac{2\pi}{N}nk} + \sum_{n=-M}^{-1} C(n)e^{j\frac{2\pi}{N}nk}\right] = \frac{1}{N}\sum_{n=-M}^{M} C(n)e^{j\frac{2\pi}{N}nk}$$

$$c(k) = \frac{1}{N}\sum_{n=-M}^{M}\left[C_x(n)\cos(\frac{2\pi}{N}nk) - C_y(n)\sin(\frac{2\pi}{N}nk)\right]$$

$$+ j\frac{1}{N}\sum_{n=-M}^{M}\left[C_x(n)\sin(\frac{2\pi}{N}nk) + C_y(n)\cos(\frac{2\pi}{N}nk)\right]$$

$$\sigma^2_{c(k)} = \sigma^2_{c_x(k)} + \sigma^2_{c_y(k)} = \left(\frac{1}{N}\right)^2 \sum_{n=-M}^{M}\left\{\left[\sigma_{C_x(n)}\cos(\frac{2\pi}{N}nk)\right]^2 + \left[\sigma_{C_y(n)}\sin(\frac{2\pi}{N}nk)\right]^2\right\}$$

$$+ \left(\frac{1}{N}\right)^2 \sum_{n=-M}^{M}\left\{\left[\sigma_{C_x(n)}\cos(\frac{2\pi}{N}nk)\right]^2 + \left[\sigma_{C_y(n)}\sin(\frac{2\pi}{N}nk)\right]^2\right\}$$

$$\sigma^2_{c(k)} = \left(\frac{1}{N}\right)^2 \sum_{n=-M}^{M}\frac{N}{2}\sigma_i^2\left\{\left[\cos(\frac{2\pi}{N}nk)\right]^2 + \left[\sin(\frac{2\pi}{N}nk)\right]^2\right\}$$

$$+ \left(\frac{1}{N}\right)^2 \sum_{n=-M}^{M}\frac{N}{2}\sigma_i^2\left\{\left[\cos(\frac{2\pi}{N}nk)\right]^2 + \left[\sin(\frac{2\pi}{N}nk)\right]^2\right\}$$

$$\sigma^2_{c(k)} = \left(\frac{1}{N}\right)^2 \sum_{n=-M}^{M}\frac{N}{2}\sigma_i^2 + \left(\frac{1}{N}\right)^2 \sum_{n=-M}^{M}\frac{N}{2}\sigma_i^2 = \frac{2M+1}{2N}\sigma_i^2 + \frac{2M+1}{2N}\sigma_i^2 = \frac{2M+1}{N}\sigma_i^2$$

$$c(k) = c_x(k) + jc_y(k) = \frac{1}{2}Be^{j\phi_k}$$

$$\begin{aligned}
\sigma^2_{c(k)} &= \sigma^2_{c_x(k)} + \sigma^2_{c_y(k)} = \left(\frac{1}{2}B\right)^2 \sigma^2_{\Phi_t} = \frac{2M+1}{N}\sigma_i^2 \\
\sigma_{\Phi_t} &= \sigma_{\Phi} = \sqrt{\frac{2M+1}{N}}\frac{2}{B}\sigma_i
\end{aligned} \tag{C.15}$$

The above deviation shows that, in the DFT method, the error is accumulated in the forward transform as indicated in equation C.14 and diluted again in the inverse transform as in the equation C.15.

The equation C.15 also shows that the possible error in phase can be substantially reduced by choosing a large grey level for the amplitude B, as recorded in the Matrox image grabber, which is shown in Table C.3.

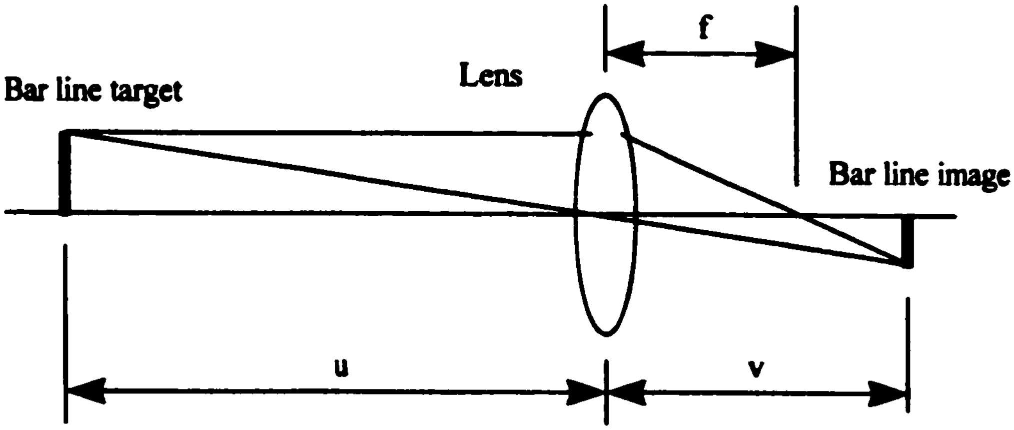

Figure C.1 The configuration of lens resolution test(assuming a thin lens)

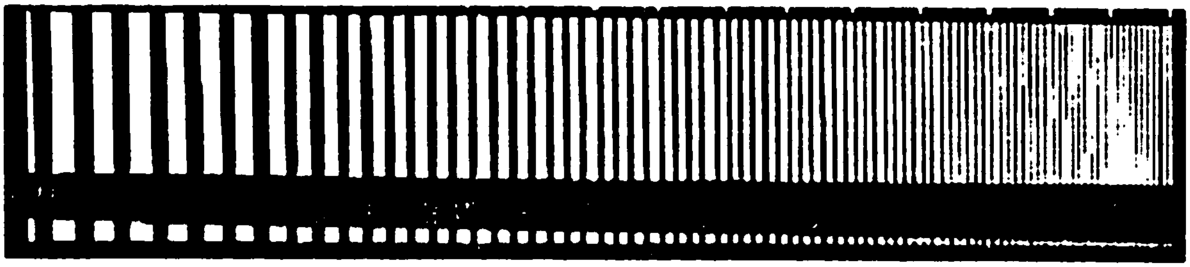

Figure C.2 The bar line target(Xerox copy)

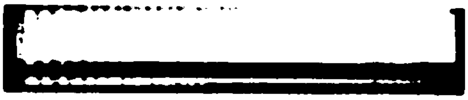

Figure C.3 The bar line image

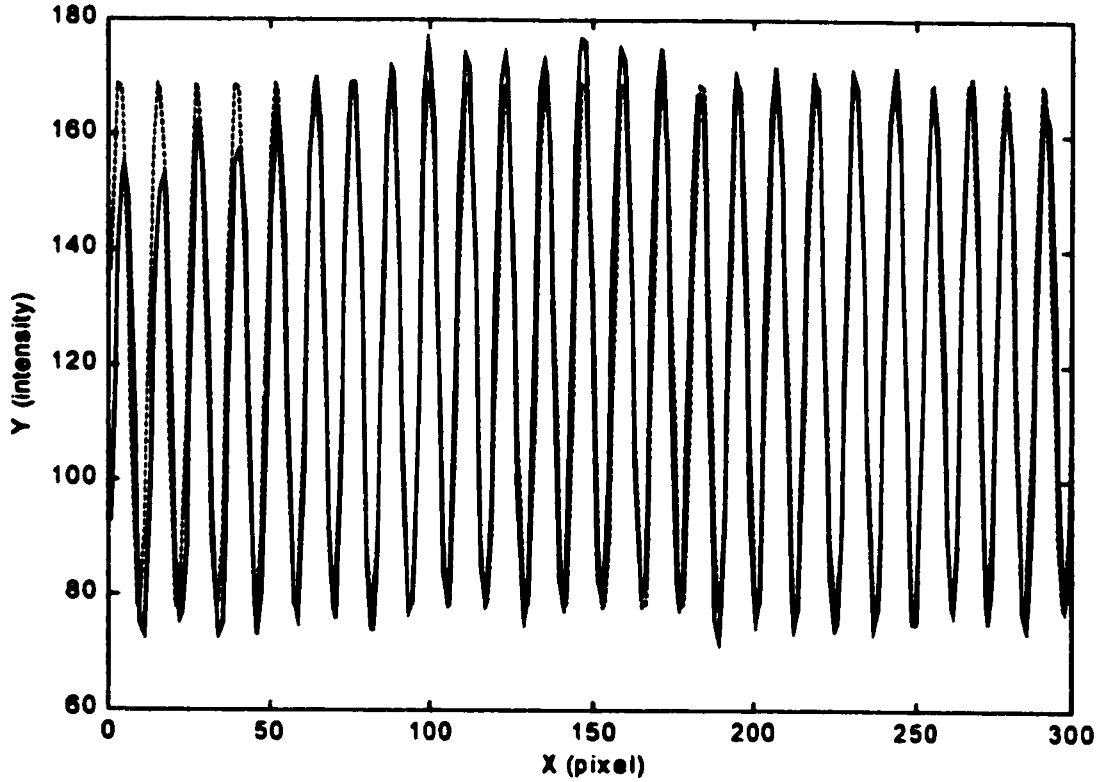

Figure C.4 The carrier of the measurement

Notes: ___ solid line: carrier measured

--- dashed line: its modeling

| Grey levels for B | Possible error in phase($\sigma_\phi/\sigma_i$) |
|---|---|
| 128 | 0.55% |
| 64 | 1.1% |
| 32 | 2.2% |
| 16 | 4.4% |
| 8 | 8.8% |
| 4 | 18% |
| 2 | 35% |
| 1 | 71% |

Table C.1 Possible error in phase for the PST method

| Sources | values | $\Delta I$ | $\Delta\Phi$(rad) | $\Delta\theta$(rad) | Percentage of $\Delta\theta$ |
|---|---|---|---|---|---|
| Mechanical Shifting | 1.25±1mm | 0~5.86 | 0~0.0888 | $0\sim11.3\times10^{-5}$ | 0~18.6 |
| Lens Resolution | 3line/5mm | 0~17.6 | 0~0.267 | $0\sim34.0\times10^{-5}$ | 0~55.9 |
| Camera Contrast | 5% | 0~6.17 | 0~0.0935 | $0\sim11.9\times10^{-5}$ | 0~19.6 |
| Pitch Measurement | 40±1mm | | | $0\sim3.14\times10^{-5}$ | 0~5.16 |
| Distance Measurement | 250±1cm | | | $0\sim0.500\times10^{-5}$ | 0~0.820 |
| Total | | | | $0\sim60.9\times10^{-5}$ | 0~100 |

Table C.2 The error transmission and distribution in the retroreflective analysis of the artifact with 16μm peak-to-peak amplitude

(The contribution of the various measurements to the percentage error in the slope for the artifact with 16μm peak-to-peak amplitude)

| Grey levels for B | Possible error in phase($\sigma_\Phi/\sigma_i$) |
|---|---|
| 128 | 0.52% |
| 64 | 1.0% |
| 32 | 2.1% |
| 16 | 4.1% |
| 8 | 8.3% |
| 4 | 16.6% |
| 2 | 33% |
| 1 | 66% |

**Table C.3 Possible error in phase for the DFT method**

**(assuming M=10 and N=100)**

# VITA AUCTORIS

Xianzhu Zhang was born in Fongyang, Anhui, China, in 1966. In 1990, he received a B.S.E. degree in Mechatronics with the highest honors and a B. S. degree in Computer Science as the second speciality, simultaneously from the University of Electronic Science and Technology of China. He was the first master student majored in microelectronic packaging technology in China and had the M.S. degree from Southeast University in 1993. Then he worked two years for the Microelectronic Lab in Nanjing Research Institute of Electronic Technology (NRIET). In 1995, he entered the Ph.D. program in the Department of Mechanical, Automotive & Materials Engineering at University of Windsor.